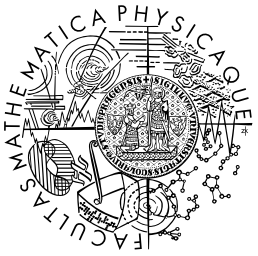

FACULTY
OF MATHEMATICS
AND PHYSICS
Charles University

**MASTER THESIS**

Jan Knapp

# Investigation of Hydrogen Interaction with Vacancies, Dislocations and Grain Boundaries in Titanium

Department of Low-Temperature Physics

Supervisor of the master thesis: doc. Mgr. Jakub Čížek, Ph.D.

Study programme: Condensed Matter Physics

Study branch: Low-Temperature Physics

Prague 2017

I declare that I carried out this master thesis independently, and only with the cited sources, literature and other professional sources.

I understand that my work relates to the rights and obligations under the Act No. 121/2000 Sb., the Copyright Act, as amended, in particular the fact that the Charles University has the right to conclude a license agreement on the use of this work as a school work pursuant to Section 60 subsection 1 of the Copyright Act.

In Prague, 10. 5. 2017 signature of the author

Title: Investigation of Hydrogen Interaction with Vacancies, Dislocations and Grain Boundaries in Titanium

Author: Jan Knapp

Department: Department of Low-Temperature Physics

Supervisor: doc. Mgr. Jakub Čížek, Ph.D., Department of Low-Temperature Physics

Abstract: This thesis deals with the system of titanium and hydrogen. Interstitial hydrogen alloys and hydrides are subject to intensive investigation, both theoretical and experimental. It has been proved, that absorbed hydrogen lowers the formation energy of defects in metals, and thus works as the so called 'defactant'. Surfactants on the surfaces of liquids lower the surface tension, defactants in solids lower the formation energy of defects. It has also been proved, that titanium absorbs hydrogen readily, when exposed to high temperature, or high pressure (fugacity); while different loading conditions lead to different features of the final sample. Beside ordinary coarse grained titanium, ultra–fine grained titanium shall be studied in present work, due to its high content of defects. Positron Annihilation Life-time Spectroscopy, a non-destructive technique sensitive on open-volume defects, shall be of prime importance in our investigation. We shall further use the X-ray diffraction, Micro-hardness measurements and Differential Scanning Calorimetry together with Thermogravimetry. Lastly, we shall strongly benefit from using existing computational tools like the Vienna ab-initio Simulation Package, or Pos330; a program for positron life–times calculations.

Keywords: titanium, hydrogen, defects, positron annihilation spectroscopy, thermogravimetry

There are three people from our Positron Annihilation Group, I would like to express my gratitude to, for helping me with this work. First of all to my supervisor doc. Jakub Cizek for leading me through this interesting and challenging project. Beside him, I would like to thank Frantisek Lukac Ph.D., for the in-situ X-ray diffraction measurements, that were performed within the Czech Academy of Sciences with his kind assistance. The third person is Dr. Petr Hruska, who helped me with numerous technical issues. A thank him very much as well. Apart from our group, I would like to thank to Sivie Maskova Ph.D., from the Department of Condensed Matter Physics, for some diffractograms, that were obtained in Karlov department by her.

# Contents

# 1. Introduction

## 1.1 The Aim of This Work

Titanium (Ti) is a very important industrial material with wide usage. What complicates its production and some of its applications is the high reactivity with light elements at high temperatures [1, 2]. Hydrogen (H) is one of these elements. H diffuses into metallic grid of Ti readily when exposed to a $H_2$ atmosphere of a high temperature, or a high pressure. Such treatment sometimes creates irreversible changes in Ti. We inquire H solution in Ti for many reasons both industrial and theoretical. Let me now introduce some of these reasons.

It is already longer than a century, since scientists began studying metal – hydrogen systems [3]. And yet the behaviour of hydrogen in metals is not completely understood. The reason is surprising complexity of the binary system metal – hydrogen. H atom is too small and light to be considered frozen in the grid; it diffuses faster than any other interstitial atom and much faster than vacancies too [3]. However, the H atom is still much larger than an electron, so we cannot describe its movement in terms of a band structure either. In principle, we would have to describe the H-phonon, H-electron and H-polaron interactions for a proper understanding of H behaviour in metals. Though there would be still even more complex interactions between H atoms generated via phonons and electrons at the same time. Fortunately, our problem can be treated in an easier way. Thermodynamics and statistical physics can give us a strong frame for the system behaviour; and we can further investigate in details the stationary states only. Due to its complexity, the phenomenon of hydrogenation is very interesting for a Condensed matter physicist.

In the field of industry; H diffusion can be a desired effect as well as an unwanted effect. Hydrogenated metals have been used in chemistry as catalysts due to their H related properties. Some other applications are H fuel cells and metal — hydrogen batteries [4]. On the other hand, hydrogenated systems and hydrides especially are very brittle. This phenomenon, the so-called hydrogen embrittlement, has not been understood for a long time; yet the key in this problem is the hydrogen — vacancy (VAC-H) interaction, which shall be discussed in this particular piece of work, very intensively both theoretically and experimentally. One can also find a phenomenon of hydrogen-assisted cracking (HAC) in literature [5, 6, 7]. These terms mean practically the same.

Ultra–fine grained materials (UFG) are relatively new issue in material science. They posses excellent mechanical properties, their production is quite complicated though. Only small samples have been prepared without cracks, so far [8, 9, 10]. One property of UFG materials is a low temperature diffusivity, which is a completely new phenomenon in physics. Together with the fact, that

UFG materials contain large amount of defects, it is natural to look at their relationship to H.

This thesis consists of several parts. First part provides a survey of existing literature to describe the principles of hydrogenation from the thermodynamical and statistical point of view. This is an essential step for setting up an appropriate framework to this study. The knowledge of thermodynamic properties of titanium–hydrogen (Ti-H) system is also important for the differential scanning calorimetry (DSC) measurements analysis.

After that, a description of techniques used for H loading is given. Ti samples were loaded in several ways and their composition and properties were investigated by the positron annihilation life–time spectroscopy (PALS), differential scanning calorimetry (DSC), X-ray diffraction (XRD) and Vickers micro-hardness testing (HV).

Results of ab-initio theoretical calculations, we have performed, are presented in the next part. These calculations will shed light on the behaviour of H in our examined system and will give us values of systems internal energy and positron life-times, comparable with our experiments.

The last part of this work presents experimental results obtained by studying the Ti-H system in-situ, or generally during a thermal processing. The same range of experimental techniques was used.

All results were obtained using an excellent experimental equipment and computational tool available at the Charles University and The Czech Academy for Sciences.

## 1.2 Hydrogen, Titanium & the Ti-H System

### 1.2.1 Hydrogen

The lightest element is known to exist in various forms. It can form mono-atomic gas at low densities and gas of diatomic molecules in arbitrary conditions. It can probably form a metallic conductor at high pressures and ionized plasma at very high temperatures [11]. There are three isotopes of hydrogen, referred as protonium (H), deuterium (D) and tritium (T). They differ among others in nuclear spin, which gives rise to different properties of diatomic molecules formed out of these isotopes, as shall be seen shortly.

The diatomic molecule $H_2$ is a very stable entity. The energy of such molecule is by $E_0 = 4.748$ eV lower, then the energy of two isolated atoms. Yet this is not the dissociation energy of hydrogen molecule, since the zero-point oscillation

energy is still around $E_v = 0.4$ eV, depending on whether the molecule is formed out of H, or D. The H (T) atom is a fermion, while the D atom is a boson. The wave-functions of electron states and vibration states are symmetric, with the interchange of two nuclei in the molecule. Thus, the fermion/boson symmetry requirement must be satisfied by the product of rotational and nuclear wave functions of the molecule. For H and T with fermionic antisymmetric wave function, this condition demands the molecular wave function to be antisymmetric. For D, the molecular wave function is symmetric. Hydrogen molecule is often thought to be "dumbbell shaped", while this is not always true. The Molecules with the rotational quantum number $J_R = 0$ are spherically symmetric. These are for instance the para-protonium ($p-H_2$) and ortho-deuterium ($o-D_2$) molecules.

In figure 1.1, one can see the difference between the $p - H_2$ and $o - H_2$. Table 1.1 shows some basic properties of hydrogen. More details about hydrogen molecules and isotopes influence of some experimental results can be found in the Fukai's book [11].

| | H | D | T |
|---|---|---|---|
| Nuclear mass $[M_P]$ | 1.000 | 1.998 | 2.993 |
| Nuclear spin | 1/2 | 1 | 1/2 |
| Nuclear moment $[\mu B]$ | 2.7928 | 0.8574 | 2.9788 |
| Molecule: | | | |
| binding energy $E_0[eV]$ | 4.748 | 4.748 | - |
| dissociation energy $E_D[eV]$ | 4.478 | 4.556 | 4.59 |
| vibration energy $E_0^v[eV]$ | 0.5160 | 0.3712 | 0.3402 |
| rotational energy $B_R[eV]$ | $7.32 \cdot 10^{-3}$ | $3.70 \cdot 10^{-3}$ | - |
| Critical point: | | | |
| Temperature [K] | 32.98 | 38.34 | 40.44 |
| Pressure [bar] | 12.98 | 16.49 | 19.06 |

Table 1.1: Basic properties of hydrogen isotopes and their di-atomic molecules.

Hydrogen is interesting among other elements for its high reactivity at low temperatures [11]. If the hydrogen was acting classically, like other big molecules do, its reactivity would not be so high. There is therefore a need for including the possibility of quantum tunnelling in chemical reactions, for a proper description of hydrogen interaction with other elements, or bulk metallic systems. According to [11], the quantum tunneling is of the biggest importance on metallic surfaces. There are also other complicating features of hydrogen, like a medium size electronegativity. Hydrogen can from tohe reasons form a various types of bonds, including metallic, covalent bonds and of course the so-called hydrogen-bond, like in water for example.

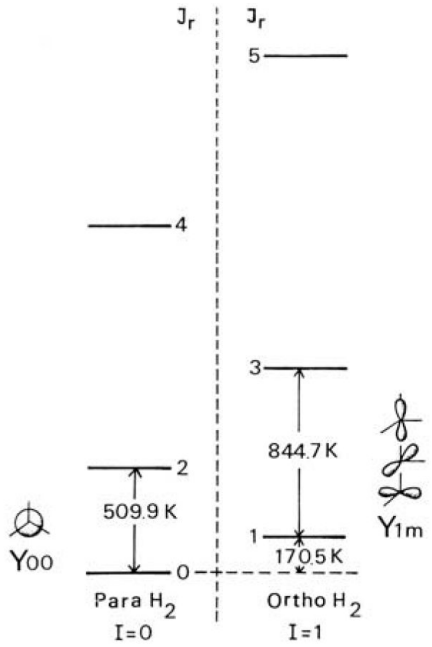


Figure 1.1: Energy and wave functions of $p - H_2$ and $o - H_2$ molecule. I, the total nuclear spin is 0, or 1. The rotational quantum number $J_R$ is 0,1,2,... [11].

There are three known ionic states oh hydrogen. The $H^-$ ion has the atomic radius of 2.1 Å, which is rather large. The size of neutral hydrogen atom is twice the Bohr radius: $r_B = 0.529$ Å. One might think, that there is no point of considering the size of $H^+$ atom, as it is a pure nucleus. Though in the presence of surrounding, the hydrogen-bond causes a contradiction of neighbouring atomic bonds and thus the atomic radius of (0.18 – 0.38) Å can be considered, depending on the number of surrounding atoms [12]. When a hydrogen atom is inserted in a metallic material, conducting electrons shield the protonic charge at small distances. Thus hydrogen in metals behaves as a neutral atom. Electronic calculations for hydrogen in transition metals have shown, that the $^1s$-like electrons around the proton, are strongly hybridized with the d-orbitals on the hosting metal. This behaviour further helps the hydrogen atom to enter a metal and diffuse through the interstitial sites in the metal lattice [11].

The vibrational energy of interstitial hydrogen in metallic lattices is usually much higher, then the vibrational energy of metallic atoms in a pure lattice. It is one order of magnitude smaller, then the typical vibrational energy of a hydrogen atom in a di-atomic molecule, but it highly influences the phase stability and preference of interstitial sites (octahedral vs. tetrahedral) [11].

### 1.2.2 Titanium

Titanium is silver, relatively low-dense and hard metal. Its density, 4510 kg/m$^3$ is somewhere between the density of aluminium and stainless steel. It is the first element in group IV B and possesses 22 electrons. It is the 7th most common metal in Earth's crust and lithosphere, but its extraction and further treatment is difficult due to its high reactivity with gasses at high temperatures [1]. It is valued for its low reactivity at low temperatures, its strength, paramagnetic behaviour and its look. Titanium is totally resistible against water, majority of mineral acids and alkali hydroxides at low temperatures [13]. It can be very easily dissolved in hydrofluoric acid or hot hydrochloric acid; the nitric acid passivates titanium's surface [13]. The reactivity of titanium is highly increased at high temperatures. It reacts with most non-metals; hydrogen, oxygen, nitrogen, carbon, boron, silicon, sulphur and halogens [13, 14, 15].

Titanium is obtained from various ores that occur naturally on the earth. The primary ores used for titanium production are ilmenite, leucoxene, and rutile. Other notable sources include anatase, perovskite, and sphene. Ilmenite and leucoxene are so-called titaniferous ores. Ilmenite $FeTiO_3$ contains approximately 53 % titanium dioxide. Leucoxene has a similar composition but has about 90 % titanium dioxide. They are found associated with hard rock deposits or in beaches and alluvial sands. Rutile is relatively pure titanium dioxide $TiO_2$. Anatase is another form of crystalline titanium dioxide and has just recently become a significant commercial source of titanium. They are both found primarily in beach and sand deposits. Perovskite $CaTiO_3$ and sphene $CaTi - SiO_5$ are calcium and titanium ores. Neither of these materials are used in the commercial production of titanium because of the difficulty in removing the calcium. In the future, it is likely that perovskite may be used commercially because it contains nearly 60 % titanium dioxide and only has calcium as an impurity. Sphene has silicon as a second impurity that makes it even more difficult to isolate the titanium [1].

Titanium is produced using the Kroll process. The steps in the Kroll process are extraction, purification, sponge production, alloy creation, and forming and shaping. At the beginning, a $TiO_2$ rich ore is put in a fluidized-bed reactor along with chlorine gas and carbon. The mixture is heated to $900^0C$ and the subsequent chemical reaction produces titanium tetrachloride $TiCl_4$ and $CO$. There are however still impurities in the product, as a result of the fact that pure titanium dioxide was not used at the beginning. Therefore various unwanted metal chlorides must be removed [1].

Thus the product is put into large distillation tanks and heated. During this step, the impurities are separated using fractional distillation and precipitation. This action removes metal chlorides including those of iron, vanadium, zirconium, silicon, and magnesium [1].

After that, the purified titanium tetrachloride is liquified and transferred to a stainless steel vessel. Magnesium is added and the vessel is heated to roughly $1100^0C$. Argon atmosphere is used. The magnesium reacts with the chlorine producing liquid magnesium chloride. Thus the solid titanium is produced, since its melting point is higher than the temperature of the reaction. The titanium solid is removed from the vessel and treated with water and hydrochloric acid to remove excess magnesium and magnesium chloride. The resulting solid is a porous metal called a sponge [1].

The pure titanium sponge can then be converted into a usable alloy via a consumable-electrode arc furnace. At this point, the sponge is mixed with the various alloy additions and scrap metal. The exact proportion of sponge to alloy material is a subject of investigation and know-how. This mass is then pressed and welded together, forming a sponge electrode. The sponge electrode is then placed in a vacuum arc furnace for melting. In this water-cooled, copper container, an electric arc is used to melt the sponge electrode to form an ingot. All of the air in the container is either removed (forming a vacuum) or the atmosphere is filled with argon to prevent contamination. Typically, the ingot is remelted one or two more times to produce a commercially acceptable ingot. After an ingot is made, it is removed from the furnace and inspected for defects [1].

### 1.2.3 Titanium – Hydrogen Phase Diagram

We have already seen, that due to its medium electronegativity; hydrogen can form various bonds with other elements. In case of titanium, similarly to other transitive metals, the metal–hydrogen bond is metallic. Metallic hydrides exist in extended range of non-stoichiometric compositions. Hydrides represent a type of an interstitial alloys, where the interstitial sites in a metallic lattice are occupied by hydrogen atoms. However we usually use the term hydride only if a long term ordering is present in the alloy. If not, we use the term random interstitial alloy. More of this issue shall be discussed in a special section about hydride formation (section 1.3.3).

Already in 1866, it was discovered that palladium can absorb large amount of hydrogen gas [16]. In fact, this is an ability natural to all metallic materials; though they differ greatly in the amount of absorbable hydrogen. Thus a construction of phase diagrams of metal–hydrogen system is a highly desirable activity. There is however an obstacle, one must deal with, when constructing a binary phase diagram of solid material, like titanium and a gas. The situation is peculiar, because when the alloy is not at all time surrounded by an atmosphere of defined and non-changing qualities, the situation is strictly speaking not in the state of equilibrium. The phase diagram is however characterizes the equilibrium state. In theory, we should deal with a system, where the outside atmosphere is considered as a reservoir of temperature, pressure and chemical potential, alternatively particles. Such layout is however very hard to reach for

experimental measurements.

Fortunately, the above condition does not have to be satisfied for every type of measurement. For many transition metals, a hydrogen impermeable surface is set up, after the sample is exposed to the air, preventing the release of absorbed hydrogen [11, 14]. Thus experiments can be performed even at room temperature and Earth's atmosphere. The phase diagram of the Ti-H system can be seen at figure 1.2.

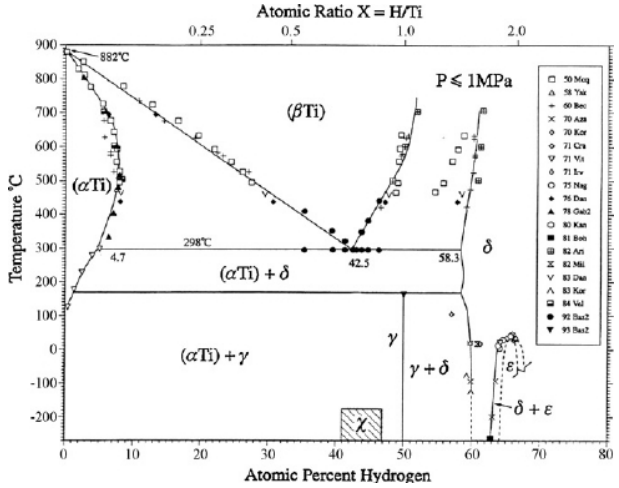


Figure 1.2: Phase diagram of Ti-H for $H_2$ pressure below 10 bar [17].

Following phases occur in the Ti-H system [17]:
• $\alpha$-Ti: a random interstitial alloy of H in the hexagonal closed-packed (hcp) structure. As pure (H-free) phase, the $\alpha-$Ti exists up to temperature of $882^0$C. A maximal solubility of H in the $\alpha-$Ti is 8 at.% at $550^0$C.
• $\beta$-Ti: a random interstitial alloy of H in the body-centred cubic (bcc) structure. of $\beta-$Ti. The pure $\beta-$Ti exist above the temperature $882^0$C. H stabilizes the $\beta-$Ti. It undergoes a eutectic decomposition to $\alpha-$Ti + $\delta$-hydride at the temperature $298^0$C. The eutectic point is at H concentration 51 at.%.
• $\delta$-phase: a Ti-H phase with Ti atoms forming a face-centred cubic (fcc) structure and H atoms occupying tetrahedral interstitial sites in that lattice. It exists in a wide range of temperature and contains at least 58 at.% of H. The $\delta$-phase is called hydrid, since a long range ordering is present and the phase is connected with relatively large enthalpy & entropy change, as will be shown later in this work.
• $\epsilon$-phase: a Ti-H phase with face-centred tetragonal (fct) structure. It exists at temperatures below $37^0$C and for hydrogen concentration above 66.7 at.%.
• $\gamma$-phase: a Ti-H phase with face-centred orthorhombic (fco) structure. It undergoes only partially reversible peritectic reaction $\gamma \rightarrow \alpha + \delta$ at $168^0$C and

H concentration very close to 50 at.%. The $\gamma$-phase is known to be unstable and is rarely detected.
• $\omega$-phase: a high pressure phase that emerges from the $\alpha-$Ti by martensitic transformation at $H_2$ pressure of 90 kbar. See figure 1.4.

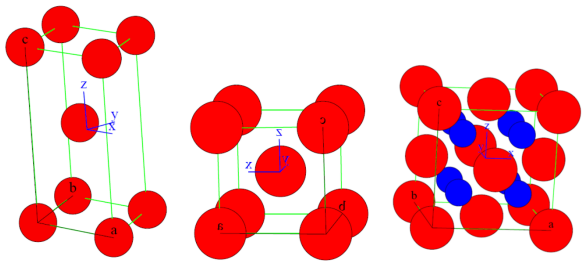

Figure 1.3: Atomic structures of hcp $\alpha-$Ti, bcc $\beta-$Ti and fcc $\delta-$hydride. Ti & H ions are denoted by red & blue circles respectively.

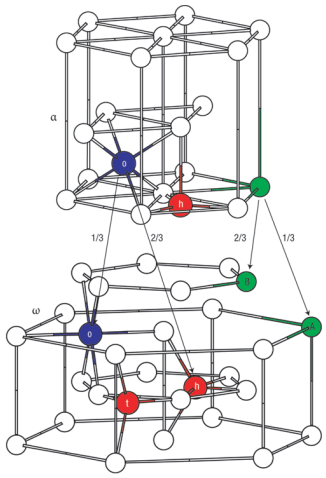


Figure 1.4: Martensitic transformation $\alpha \rightarrow \omega$ with interstitial sites new localization [18].

### 1.2.4 Hydrogen Occupation of Interstitial Sites in Titanium Lattice

In all three main crystal lattices of metals, i.e. fcc, bcc & hcp, one can find octahedral (O) and tetrahedral (T) interstitial sites. They are envisioned in Figure 1.5. In diverse materials, different set of sites is preferred by H. Also,

unfortunately different studies often come to different results regarding the occupancy of interstitial sites by H [19].

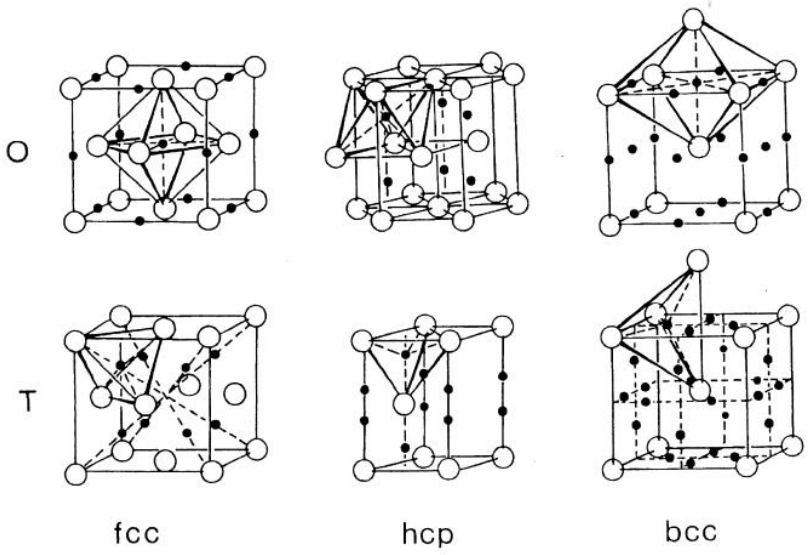


Figure 1.5: Interstitial sites in hexagonal and cubic lattices [20].

In case of hcp lattice, which is of primal interest for us, we can deduce, that every metal atom is surrounded by 6 (O) sites and 8 (T) sites. The number of (O) sites is therefore the same, as the number of all atoms in the lattice. There are two crystallographically equivalent (T) sites located in the [001] direction above and bellow each atom. Remaining 6 (T) sites are located at slightly larger distance from the atom.

Ti atoms form a tetrahedron around a (T) site and an octahedron around an (O) site, see Figure 1.5. When the lattice does not have the ideal c/a ratio of 1.633 those tetrahedrons and octahedrons are deformed. In case of titanium, the c/a ratio is 1.588 and is therefore slightly smaller than the ideal ratio. The c/a ratio actually highly influences the properties of a material. In materials with the c/a ratio lower than the ideal value, the pyramidal slip becomes more important. Such material is then very tough [21].

Table 1.2 shows properties of interstitial sites in the most common metallic lattices. Considering the slightly smaller c/a ratio in case of Ti, the interstitial sites sizes presented in Table 1.2 would be slightly different. The (O) sites in hcp lattice are bigger, than (T) sites.

One can see in Figure 1.3, that the $\delta-$hydride is actually a fcc titanium lattice, with (T) sites occupied by H. This type of lattice is also called fluorite,

or simply $CaF_2$ type of lattice.

| Structure | fcc & hcp(c/a=1.633) | | bcc | |
|---|---|---|---|---|
| Type | O | T | O | T |
| Number per atom | 1 | 2 | 3 | 6 |
| Size | 0.414 | 0.225 | 0.115 | 0.291 |

Table 1.2: Number per host metal atom, type and size of interstitial sites in common metallic lattices. Size of interstitial sites are expressed in units of atomic radius host metal atoms.

## 1.3 Thermodynamics of Interstitial Alloys & Hydrides

### 1.3.1 Titanium – Hydrogen Interstitial Alloy

Hydrogen absorbed in two systems will be considered in this section: a perfect Ti lattice and Ti lattice containing vacancies. The first case supposes equilibrium of the type: Ti – H. The second case supposes Ti – VAC – H equilibrium and thus it is noticeably more difficult. Results according to theoretical articles shall be presented.

#### H Solution in a Perfect Ti Lattice

The hydrogenation reaction is:

$$Ti + \frac{X}{2} H_2 \rightarrow TiH_X \tag{1.1}$$

During this reaction, enthalpy $X \cdot \Delta H$ is produced/consumed. It is negative for exothermic process and positive for endothermic process of H absorption. Equation 1.1 in fact describes three step process: First, the hydrogen molecules are adsorbed to the surface of titanium. Then they are dissociated into atomic hydrogen. Finally, atomic hydrogen quickly diffuses into the bulk. In equilibrium the chemical potential for absorbed hydrogen and hydrogen bound in a $H_2$ molecule are keeping each other equal.

$$\mu_H^\alpha = \frac{1}{2} \mu_{H_2} \tag{1.2}$$

The factor $\frac{1}{2}$ is present, because on $H_2$ molecule produces two H atoms. Assuming that absorbed hydrogen behaves as ideal non-interacting gas, the concentration of hydrogen absorbed in a metal in thermodynamic equilibrium with $H_2$ atmosphere of pressure p obeys the Sieverts law:

$$x \sim \sqrt{p} \tag{1.3}$$

The Sieverts law holds true for low hydrogen concentration solutions, when H–H interaction can be neglected. It was first observed for a gases like hydrogen, oxygen and nitrogen and their solubility in water. It holds true very accurately for some metal – gas systems too [22].

In order to derive the exact relation between the concentration and thermodynamical quantities, the metal–hydrogen system has to be treated as either the canonical, or the grandcanonical ensemble. None of these approaches is totally accurate, since the hydrogenation process is in fact non-equilibrium. Using the canonical ensemble is easier, but less correct for low temperatures and high hydrogen concentrations. Results obtained by using the grand-canonical ensemble will be presented, as derived here: [3]. After that, the low concentration limit will be used, in order to get easier expression for concentration.

The chemical potential of the hydrogen gas is given by contributions from translation, rotation, vibration and binding states of $H_2$ molecule. For details see [3]:

$$\frac{1}{2}\mu_{H_2} = k_B T \; ln\left(\zeta \cdot \frac{p^{1/2}}{T^{7/4}}\right) + \frac{1}{4}\hbar\omega_{vib} + \frac{1}{2}k_B T \; ln\left(1 - e^{-\frac{\hbar\omega_{vib}}{k_B T}}\right) + \frac{1}{2}\epsilon_{H_2} \tag{1.4}$$

$\omega_{vib}$ is the vibrational energy: $\hbar\omega_{vib} \approx 540$ meV [3]. $\epsilon_{H_2}$ is the binding energy of $H_2$ molecule. $\zeta$ is a constant and it is expressible in terms of fundamental constants:

$$\zeta = \left(\frac{2h^5}{(4\pi m_H k_B)^{3/2} 8\pi^2 I k_B^2}\right)^{1/2} \tag{1.5}$$

$I \approx 13.6 \cdot 10^{-47}$ kg.m$^2$ is the moment of inertia for rotation of $H_2$ molecule. The chemical potential $\mu_{H_2}$ depends explicitly on the temperature and pressure.

The chemical potential of hydrogen atoms occupying interstitial sites $\mu_H^\alpha$ is a next step. The interaction between hydrogen atoms is considered, but using the mean field approximation, so the interaction only depends on $n$, the number of absorbed H atoms. We denote the energy bound to this interaction: $W = w(n)$.

The partial function of H atoms occupying interstitial sites can be expressed as a product of two factors. The first factor is the binomial distribution of $n$ H atoms in N possible sites; with the probability of such configuration given by Boltzmann factor:

$$Z_{config} = \frac{N!}{n! \cdot (N-n)!} \cdot e^{-\frac{n \cdot w(n)}{k_B T}} \tag{1.6}$$

The second factor arises from the harmonic oscillations of hydrogen, inside an interstitial site with angular frequency $\omega_0$. Einstein model of oscillations is considered [3].

$$Z_{oscill} = \frac{e^{-\frac{3\hbar\omega_0}{2k_BT}}}{\left(1 - e^{-\frac{\hbar\omega_0}{2\,k_BT}}\right)^3} \cdot e^{-\frac{\epsilon_0}{k_BT}} \tag{1.7}$$

$\epsilon_0$ is the ground state energy of H inside an interstitial site. It can be taken as energy reference and therefore set up to $\epsilon_0 = 0$. By following:

$$\mu = \frac{\partial F}{\partial n} \tag{1.8}$$

and

$$F = -k_BT\ ln(Z) \tag{1.9}$$

The chemical potential $\mu_H^\alpha$ can be written in the form:

$$\mu_H^\alpha(T,n) = -k_BT\ ln(Z_{oscill}) + k_BT\ ln\left(\frac{x}{1-x}\right) + w(n) + \frac{\partial w(n)}{\partial n} \cdot n \tag{1.10}$$

where $x = n/N$ is the H concentration. The first term in 1.10 is the chemical potential of a single interstitial entity and together with the second term creates a chemical potential for infinite dilution of hydrogen. The last term can be written as $\frac{\partial w}{\partial x} \cdot x$ and is responsible for limited hydrogen solubility in the lattice.

Inserting the partial function $Z_{oscill}$ into to first term in equation 1.10 one gets the expression:

$$\mu_0 = \epsilon_0 + \frac{3}{2}\hbar\omega_0 + 3\ ln\left(1 - e^{-\frac{\hbar\omega_0}{k_BT}}\right) \tag{1.11}$$

The expression consists of a ground state energy level, zero-oscillation energy and the Gibbs energy for thermal excitations of a harmonic oscillator [3]. For the sake of clarity, let us divide the chemical potential $\mu_H^\alpha$ into a term describing an infinite dilution, denoted $\mu_H^\infty$, and the rest:

$$\mu_H^\alpha(T,x) = \mu_H^\infty(T,x) + w(n) + \frac{\partial w}{\partial x} \cdot x \tag{1.12}$$

Now, the chemical potentials $\mu_H^{solid}$ and $\frac{1}{2}\mu_{H_2}$ shall be put equal. For now, we neglect the last two terms in 1.12. We recall using the grand-canonical ensemble, since both chemical potentials have different variables.

$$x = \frac{1}{1 + e^{\frac{(-\frac{1}{2}\mu_{H_2} + \mu_0)}{k_BT}}} \tag{1.13}$$

Equation 1.13 have a form of Fermi – Dirac distribution. The degeneracy of the ground energy level is N. For $x \ll 1$ the distribution coincide with the Maxwell – Boltzmann distribution.

The Maxwell–Boltzmann limit of 1.13, is:

$$x = \sqrt{\frac{p}{p_0}} \cdot e^{\frac{\Delta s^{nc}}{k_B}} \cdot e^{-\frac{\Delta h}{k_B T}} \tag{1.14}$$

We call $\Delta h$ the molar enthalpy of the solution and $\Delta s^{nc}$ the non-configurational part of the molar entropy of the solution. We came to that expression by taking chemical potentials $\frac{1}{2}\mu_{H_2}$ (equation 1.4) and $\mu_0$ (equation 1.11) and denoting:

$$p_0 = \frac{\zeta^2}{T^{7/2}} \tag{1.15}$$

$$\Delta s^{nc} = k_B \; ln\left(1 - e^{-\frac{\hbar\omega_{vib}}{k_B T}}\right) \tag{1.16}$$

and

$$\Delta h = \frac{1}{2}\hbar\omega_{vib} + \epsilon_{H_2} - \mu_0 \tag{1.17}$$

The molar entropy change is called non-configurational, since only vibrational states of the gas and of the H in the interstitial site contribute. However, the entropy of H in the interstitial was not considered in the derivation, since its exact form is not known [3]. It can be however easily added into the finial expression. The configurational part in $\mu_H^\alpha$ was used to get the variable of concentration: $x$. The pressure $p_0$ is temperature dependent. The entropy change, is referred to $p_0$ at every temperature $T$ [11]. In other words, you calculate the value of entropy change at given temperature by considering the entropy vanishing of the $H_2$ gas of pressure $p_0$ & temperature $T$.

If treating the chemical potential $\mu_H^\alpha$ as full, another exponential term should be present in 1.14. That is:

$$e^{-\frac{pv_H}{k_B T}} \tag{1.18}$$

Where $v_H$ is a molar volume change of the solution. However, according to: [11], the partial volume is proven to be widely temperature independent and similar for many metals. It can be taken as approximately $v_H = 3\mathring{A}^3$. Together with a pressure of around one hundred bar, it gives energy of $pv_H \approx 0.19$ meV and thus the last exponential factor can be easily neglected for low pressures.

The equation 1.14 shows that the sign of enthalpy change is in primal importance. The enthalpy change varies throughout the periodic table, because it is given by the gross electron structure of the host metal. As we have seen, the term

$pv_H$ is negligible, so the enthalpy change is in fact equal to the internal energy change, that can be calculated by using density functional theorem (DFT). Generally speaking the enthalpy change is negative for metals at the left side of the periodic table and positive for metals at the right side of the periodic table. It is extra large for precious metals for example. See [11] and [23] for more information.

Metals with negative enthalpy, posses a positive affinity to hydrogen. Even though the solubility might not be large ($\alpha$-Ti), the hydrogen never accumulates somewhere in the sample, causing the metal to blister. If on the other hand the enthalpy is positive, there is a negative affinity between the metal and hydrogen and the solubility is either low, or the hydrogen gas slowly damages the sample, sometimes causing it to blister [23].

If we look at the Ti-H phase diagram 1.2, we can immediately see, that the equation 1.14 wont work for $\alpha$-Ti very well. The solubility rises with decreasing temperature only for temperature range $500 - 800^0$C. Indeed, in this temperature range, the equation 1.14 can be used according to [11] and the enthalpy change is $\Delta h(\alpha) \approx -0.55$ ev/atom. The equation 1.14 works well for $\beta$-Ti and $\Delta h(\beta) \approx -0.62$ ev/atom. The non-configurational entropy change is mostly given by the disappearance of the gas entropy and is around $\Delta s^{nc}(\alpha) \approx -7k_B$ & $\Delta s^{nc}(\beta) \approx -6k_B$ at temperature ranges: $500 - 800^0$C & $900 - 1100^0$C respectively [11].

The plot of H solubility vs. inverse of temperature, when the solubility is in logarithmic scale is called Arrhenius plot. If the plot is linear, enthalpy is given by the slope of the curve. The value of entropy is given, by the line intersection with the concentration axis. Figure 1.6 shows the Arrhenius plot for Ti-H system and several other metal–hydrogen systems.

As one can see in figure 1.6, $\beta - Ti$ shows common behaviour, corresponding to the value of enthalpy change given. However a plateau occurs, where one would expect $\alpha - Ti$ interstitial alloy.

How is it possible, that the slope in 1.6 is zero, even though the enthalpy change for $\alpha$-Ti is large enough? The reason is that figure 1.6 shows behaviour at high H concentration, when H interstitial alloy in $\alpha$-Ti does not exist at all. See the phase diagram 1.2; at H concentration $X \sim 1$ only a mixture of $\beta$-Ti & $\delta$-hydride exist.

Ti-H system is very interesting. Even though the $\alpha$-Ti has a positive affinity to hydrogen, a new phase ($\delta$-hydride) has even smaller energy and arises therefore instead of $\alpha$-Ti interstitial alloy. There also has to exist a relatively strong H-H interaction in the $\alpha$-Ti, otherwise the $\delta$-hydride could not arise.

The H solubility in $\alpha$-Ti is never larger than 8 at. %. Moreover, bellow the temperature of $168^0C$, the solubility is almost negligible [17]. The system

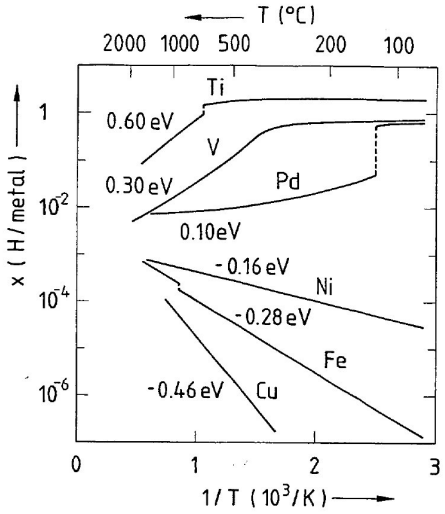


Figure 1.6: Arrhenius plot of hydrogen solubility in several metal–H systems [23].

strongly prefers the hydride formation, or the $\beta - Ti$ interstitial alloy. Hydrogen stabilizes the $\beta - Ti$ up to temperature $298^0C$, while the pure Ti $\alpha \rightarrow \beta$ transition temperature is $882^0C$. The hydride formation will be discussed in seection 1.3.3.

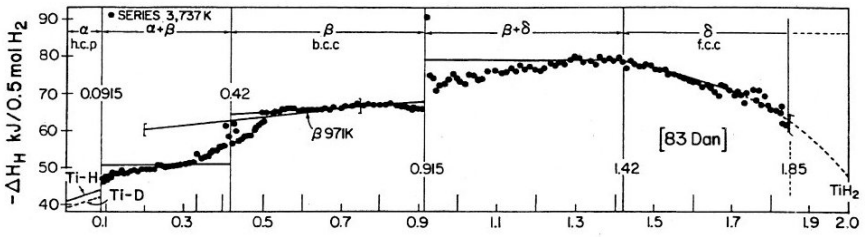


Figure 1.7: Enthalpy dependence of the concentration of H absorbed [17]. Measured at $464^o$C.

Experimental data from [17] for the enthalpy change dependence on concentration are shown in figure 1.7. For the entropy change they are in figure 1.8.

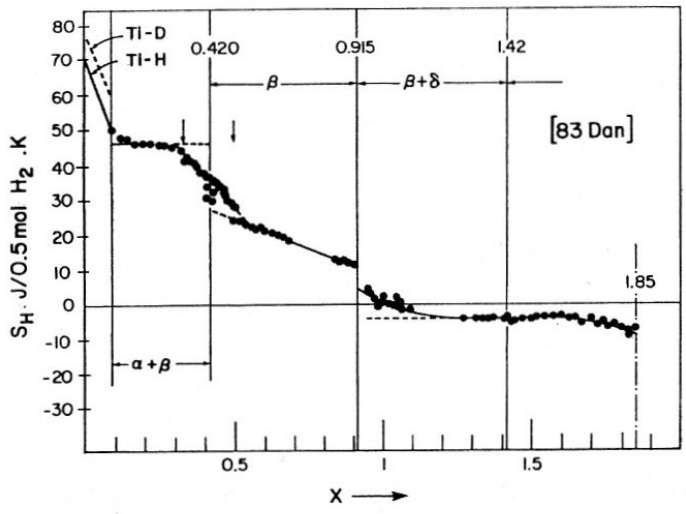


Figure 1.8: Entropy of solution dependence of the concentration of H absorbed [17]. Measured at 464$^o$C.

The $\Delta s^{nc}$ is connected to the entropy $S_H$ in figure 1.8 by:

$$\Delta s^{nc} = S_H - \frac{1}{2} S^0_{H_2} - \Delta s^c \tag{1.19}$$

$\Delta s^c$ is the configurational part of the entropy of the solution. Figure 1.8 is quite valuable, since it shows how large is the entropy of the solution without the largest contribution from the gas entropy vanishing, and with the contribution of configurational entropy. Generally it connects the entropy change that can be measured with the entropy change, that is used in equation 1.14. It can be seen, that for interstitial alloys in $\alpha$-Ti and $\beta$-Ti, the entropy is lowered with concentration, while for the phase mixture, it remains constant. For $\delta$-hydride it is negative, due to the ordering.

The units used in figures 1.7 & 1.8 differ from (eV/atom) & ($k_B$) we have used. I therefore give the conversion: The $\Delta H_H$ in figure 1.7 is plotted on interval $(0.41 - 0.93)$ eV/atom $= (40 - 90)$ kJ/0.5 mol $H_2$. The $S_H$ in figure 1.7 is plotted on interval $(-3.61 - 9.62)$ $k_B = (-30 - 80)$ J/0.5 mol $H_2$ K.

As one can see, there is a lack of experimental data for $\alpha$-Ti in figure 1.8. This corresponds to the problems, that were mentioned. From this reason, it is highly appropriate, to perform DFT based calculations, to get an insight into the Ti-H system.

**Hydrogen Solution in Titanium Grid Containing Vacancies**

This section deals with the Ti-VAC-H equilibrium. Such system is more difficult to be described than the Ti-H system, though the theory is known and is in good conformity with experiments [24, 3].

First we have to emphasize that a process of hydrogenation with instantaneous vacancies production is in fact non-equilibrium state. We make it to be quasi-equilibrium by considering processes of pure grid hydrogenation and vacancies production separated. In other words first the pure grid is filled with hydrogen to some level; then the vacancies are produced, due to the already absorbed hydrogen and surrounding $H_2$ atmosphere tops up the H concentration to its equilibrium value in the VAC free lattice.

Let $x$ be the equilibrium H concentration calculated for example by equation 1.14 from the previous section. The total vacancy concentration in the VAC containing lattice will be:

$$C_{VAC} = \sum_{i=0}^{g} P_i \phi_i \tag{1.20}$$

The $P_i$ stands for the binomial distribution, coming from distributing up to $i$ H atoms, into $g$ interstitial sites, surrounding a VAC. We will call such object a VAC-H cluster.

$$P_i = \frac{g!}{i!(g-i)!} x^i (1-x)^{(g-i)} \tag{1.21}$$

$x^i$ & $(1-x)^{(g-i)}$ are probabilities of the binomial distribution.

$\phi_i$ is the Fermi-Dirac distribution of VAC-H clusters:

$$\phi_i = \left[ 1 + exp\left( \frac{E^f_{VAC} + \Delta\epsilon^i_{VAC}}{k_B T} \right) \right]^{-1} \tag{1.22}$$

$E^f_{VAC}$ is the formation energy of a VAC and $\Delta\epsilon^i_{VAC}$ is the energy difference between a pure VAC and VAC surrounded by $i$ H atoms. $\Delta\epsilon^i_{VAC}$ is negative for systems, where H stabilizes VAC.

Equation 1.20 is surprisingly easy, though the mean issue might be, to express the VAC free H concentration $x$ for metals like Ti, where the equation 1.14 does not work very well. The second issue of equation 1.20 is that it treats all space arrangements of $i$ H atoms decorating a VAC as energetically equal. For Ti, this will be shown to be not accurate.

### 1.3.2 High Hydrogen Pressure/Fugacity Loading (Solubility Enhancement)

The so far described systems were systems of metal with the surrounding hydrogen atmosphere considered as ideal gas. However, the hydrogen atmosphere acts like the ideal-gas only up to pressure of roughly 10 bar, according to [11], or 100 bar, according to [23]. For effects, that will be described here, the 10 bar value is better to be considered.

At the beginning of this work, a table (1.1) of basic hydrogen properties was presented. The super critical region for protonium starts from temperature 33 K and pressure 13 bar. It may be anticipated that a very steep increase of the chemical potential of super-critical hydrogen, $\mu^{fluid}$, as showed in figure 1.9, should lead to large increase of hydrogen solubility.

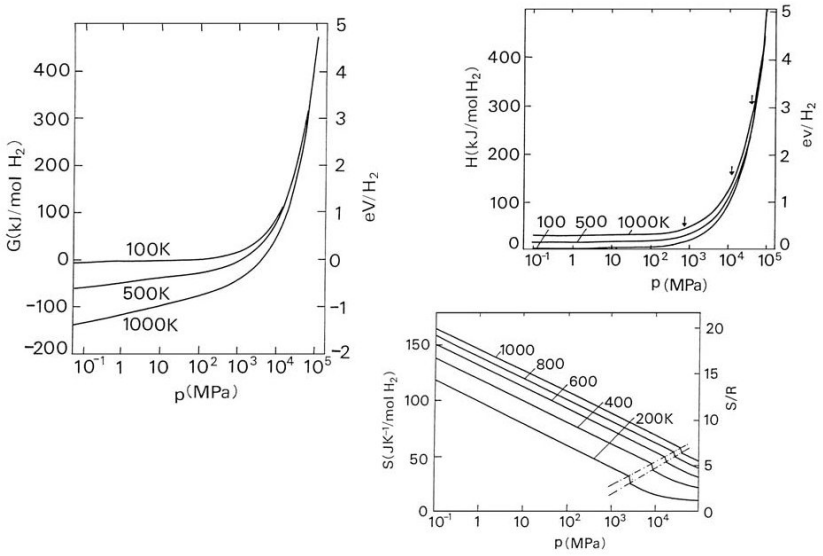


Figure 1.9: Molar Gibbs free enthalpy, molar enthalpy & molar entropy dependency on pressure in its extended range [11].

This conjecture is strongly supported by present experiments. Many groups around the world, dealing with metal–H systems, occupy themselves by building maximal reachable hydrogen pressure apparatuses. Typically two types of experiments are performed [11]. Either, a hydride prepared by standard, low pressure method, is placed into the high pressure atmosphere and changes in relative phase stability are followed. One must bear in mind, that the term $pv_H$ introduced in equation 1.14 becomes important at high pressures. It gives energy values around 0.1 eV and thus influence the once reached phase stability. The second type of experiment is insertion of pure metallic sample into the high

pressure atmosphere. Results of this type of experiments are usually given in the form of equilibrium $p_H - T$ diagrams with hydrogen concentration $x$ as an implicit variable [11]. Such results are in figure 1.10 from [17]. High hydrogen pressures cause large enhancements of the solubility, and allow the investigation of metal–hydrogen systems in hitherto unattainable ranges of temperature and hydrogen concentrations. The effects on the phase stability are studied too.

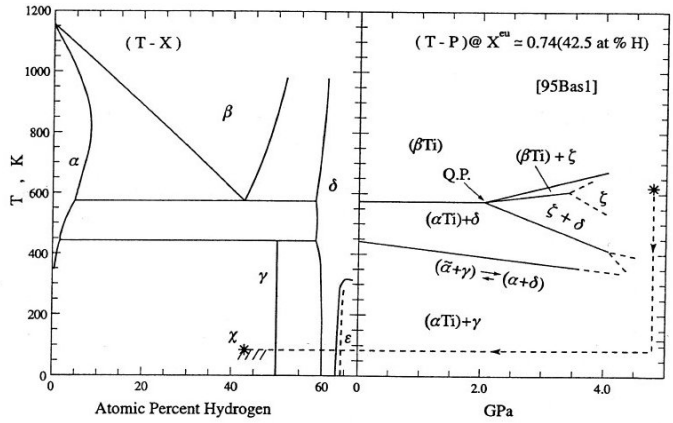


Figure 1.10: Sketch of Ti-H system at high hydrogen pressure [17]. Visible phases were described in the Ti-H phase diagram section 1.2.3.

In order to reach an equilibrium between interstitial alloy and surrounding hydrogen atmosphere, the same condition as in the previous chapter must hold:

$$\mu_H^\alpha = \frac{1}{2}\mu^{fluid} \tag{1.23}$$

Theoretical calculations of molar Gibbs free enthalpy (chemical potential), molar enthalpy and molar entropy were presented in figure 1.9. The values were calculated by:

$$G(p,T) = G(p_0,T) + \int_{p_0}^{p} V dp \tag{1.24}$$

$$S(p,T) = S(p_0,T) - \int_{p_0}^{p} \left(\frac{\partial V}{\partial T}\right) dp \tag{1.25}$$

The enthalpy value is given simply by: $H = G + TS$. For the integration in equations 1.24 & 1.25, Van der Waals like equation of the gas was considered:

$$\left[p + \frac{a(p)}{V^\zeta}\right][V - b(p)] = RT \tag{1.26}$$

### 1.3.3 Formation of Hydride

The term hydride is not precisely defined one. Certain is, that it is a new phase, for which H atoms are considered occupying some certain exact positions in the lattice, rather than forming a random interstitial alloy. The ideal stoichiometric hydride of titanium $TiH_2$ was shown in figure 1.3. It has the $CaF_2$ crystalline structure, similar to all hydrides of all IV B elements [11]. In another words, H atoms occupy (T) interstitial sites in the fcc lattice of titanium. If hydrogen concentrations of at least 58 at. % is reached inside a Ti bulk, $\delta$-hydride arises. More about $\delta$-hydride has been discussed in the 1.2.3 section.

Hydride arises from the hydrogen interstitial solution, when such change becomes energetically favourable. The hypothetical reaction of hydride formation is:

$$\frac{1}{x_\delta - x_\alpha} MH_{x_\alpha} + \frac{1}{2} H_2 \rightarrow \frac{1}{x_\delta - x_\alpha} MH_{x_\delta} \tag{1.27}$$

$x_\alpha$ is the H concentration in $\alpha$-phase and $x_\delta$ is the H concentration in $\delta$-phase. The Gibbs potential of such reaction remains unchanged. The entropy can be divided into pressure dependent and independent part:

$$\Delta H^{\alpha\rightarrow\delta} - T\left(\Delta S^{\alpha\rightarrow\delta} + k_B\, ln\frac{p}{p_0}\right) = 0 \tag{1.28}$$

$H^{\alpha\rightarrow\delta}$ is the enthalpy change for $\alpha \rightarrow \delta$ transformation. $\Delta S^{\alpha\rightarrow\delta}$ is the entropy change of the transformation, which is not influenced by the pressure of surrounding $H_2$ atmosphere. The values of enthalpy and entropy can be determined from the Arrhenius plot. However, due to the pressure term, the Arrhenius plot contains a plateau, due to the pressure term. (Bear in mind, that $p_0$ is temperature dependant.) Another illustrative plot can be done to visualize the solubility behaviour. It is the so-called plot of $p - x - T$ isotherms. Such plot for Ti-H system is presented in figure 1.11.

The pressure versus composition isotherms graph is a very practical tool. It allows one to directly read required temperature and/or pressure, if certain composition is supposed to be reached in equilibrium (after sufficient time of loading). We can clearly see that for Ti-H system, the higher the temperature is the larger pressure is required, in order to reach given composition. The two phase regions occur as plateaus on the plot. That shows, how wide range of compositions can be reached by the same pressure. This immediately implicates, that the pressure & temperature are not the only variables influencing the final constitution of loaded sample. The phenomenon is diffusion and the third variable influencing the constitution of a two phase system is time.

Taking the accessible experimental data, Fukai [11] determined values of $\Delta H^{\alpha\rightarrow\delta} = -0.68$ eV/atom & $\Delta S^{\alpha\rightarrow\delta} = -6k_B$ for Ti-H system. This values

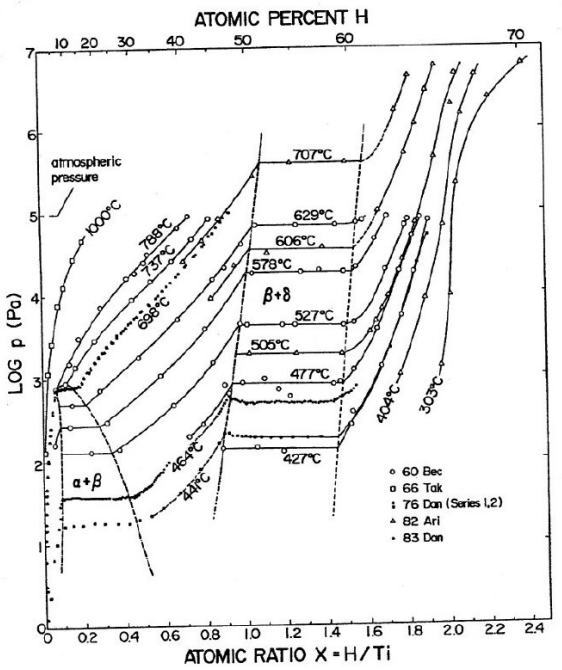


Figure 1.11: Pressure vs. concentration isotherms plot [17].

hold true for the $\delta$-hydride formation from $\alpha - Ti$ interstitial alloy for temperature lower than $300^0C$ [11]. Extensive experimental data can be found here [17].

We shall now develop a thermodynamic formalism that is applicable to binary interstitial alloys. Consider the Gibbs potential for crystal consisting of $N$ metal atoms and $n$ hydrogen atoms. $\mu_{Ti}$ shall be the chemical potential of metal species and $\mu_H$ shall be the one of hydrogen.The Gibbs potential will be:

$$G = N\mu_{Ti} + n\mu_H \tag{1.29}$$

or in a term of composition ratio $x = \frac{n}{N}$:

$$g = \frac{G}{N} = \mu_{Ti} + x\mu_H \tag{1.30}$$

Therefore:

$$\mu_H = \left(\frac{\partial g}{\partial x}\right)_{p,T} \tag{1.31}$$

$$\mu_{Ti} = g - x \cdot \left(\frac{\partial g}{\partial x}\right)_{p,T} \tag{1.32}$$

If we plot $g$ vs $x$ for $p, T$ given; $\mu$ is given by the slope of the tangent to the $g(x)$ curve at given s and $\mu_0$ is given by the intercept with the y-axis.

If we want to describe the equilibrium situation, where the hydride coexists with the solid solution and the hydrogen gas atmosphere, we write following equalities:

$$\mu^{\alpha}_{Ti}(p, T, x_\alpha) = \mu^{\delta}_{Ti}(p, T, x_\delta) = \frac{1}{2}\mu_{H_2}(p, T) \tag{1.33}$$

$$\mu^{\alpha}_{H}(p, T, x_\alpha) = \mu^{\delta}_{H}(p, T, x_\delta) = \frac{1}{2}\mu_{H_2}(p, T) \tag{1.34}$$

We came across the hydrogen gas chemical potential already. It is the expression 1.4. Since, as mentioned, the chemical potential $\mu_H$ is given by the slope of $g(x)$, the two phases coexistence condition is:

$$\frac{1}{x_\delta - x_\alpha}\int_{x_\alpha}^{x_\delta} \mu_H(x)dx = \mu_H(x_\alpha) = \mu_H(x_\delta) = \frac{g(x_\delta) - g(x_\alpha)}{x_\delta - x_\alpha} \tag{1.35}$$

This is the so-called Maxwell's construction. Only one out of four variables $(p, T, x_\delta, x_\alpha)$ can be considered independent, due to the Gibbs' phase rule. If we decide to change the temperature, we could eventually receive a theoretical background for the graph 1.11. Skipping the steps, the equilibrium condition can be written as [11]:

$$\frac{1}{2}\, ln\frac{p_{eq}}{p_0} = \frac{1}{k_B T}\left(\mu^{\delta} - \frac{1}{2}\mu^{g}\right) = \frac{1}{k_B T}\left(\mu^{\alpha} - \frac{1}{2}\mu^{g}\right) \tag{1.36}$$

Where $p_{eq}$ is the equilibrium plateau pressure in the two-phase coexistence region. From this condition, this follows for the molar enthalpy and entropy change:

$$\Delta h^{\alpha\to\delta} = \Delta h^{\alpha}(x_\alpha) = \Delta h^{\delta}(x_\delta) \tag{1.37}$$

$$\Delta s^{\alpha\to\delta} = \Delta s^{\alpha}(x_\alpha) = \Delta s^{\delta}(x_\delta) \tag{1.38}$$

This is a crucial result, since the molar enthalpy and entropy can now be identified with $\Delta H^{\alpha\to\delta}$ and $\Delta S^{\alpha\to\delta}$ witch are, according to equation 1.28, obtained from the slope and intercept of the Arrhenius plot.

Unfortunately, the given description is only sufficient for high temperature region for Ti-H system. Additional effect has to be taken into account. As can be seen on Figure 1.11, the experimental data were obtained for sufficiently high temperature only. The reason for that is the terminal (almost zero) H solubility in $\alpha$-Ti.

### 1.3.4 Diffusion of Hydrogen

Hydrogen is the lightest interstitial element and it is known to have a large diffusivity. There is not much known about the exact interaction between the hydrogen atom and host material atoms, though we consider the interaction to be small [3]. Various diffusion processes have been proposed and are depicted at Figure 1.12, with corresponding diffusion coefficients, which will be discussed.

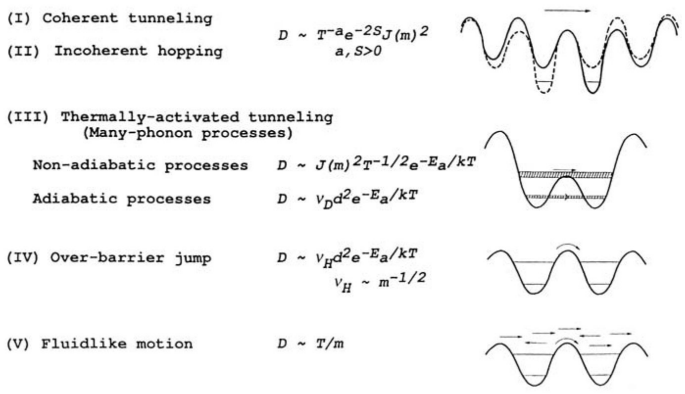


Figure 1.12: Schematic depiction of diffusion processes of H at different temperatures with diffusion coefficients [11].

Al lowest temperatures, the hydrogen wavefunction must be delocalized and must be in a form of a band state, unless trapped by a lattice defect. Such wavefunction propagates through the lattice, but is limited by thermal phonons and crystal defects. At higher temperature, the wavefunction becomes localized in interstitial sites and its movements through the lattice become thermally activated. At even higher temperatures, classical thermally activated jumps occur, in two kinds; the thermally activated jumps to the same energy level, as the current one; and the thermally activated jumps to higher energy levels. This is the moment, when H can be considered as a particle. At the highest temperatures, the H atom diffuses through the lattice like a fluid, since its energy is higher, than the energy of barriers [11]. Of course, processes mentioned above hold true for one hydrogen atom only. Not much investigation has been done in case of coherent diffusion of several H atoms [3].

A basic phenomenological approach is to describe the H diffusion in a metallic lattice by Fick's law. Two diffusion coefficients can be introduced for metal–hydrogen system. They are the chemical coefficient $D$ and the self (or tracer) diffusion coefficient $D_{self}$. The chemical flux of H is given by:

$$\vec{j}(\vec{r},t) = -D\nabla x(\vec{r},t) \tag{1.39}$$

where $x(r,t)$ is the hydrogen concentration. The continuity equations holds too:

$$x = -\nabla \cdot \vec{j}(\vec{r},t) \tag{1.40}$$

Where $j$ is the H flow. We get a classical diffusion equation:

$$x(\vec{r},t) = D\nabla^2 x(\vec{r},t) \tag{1.41}$$

There is a second diffusion equation for a 'hydrogen interstitial' as well. It is characterised by the diffusion coefficient $D_{self}$ and the variable is $p(\vec{r},t)$; the probability of finding certain occupied interstitial at volume $dV$:

$$p(\vec{r},t) = D_{self} \cdot \nabla^2 p(\vec{r},t) \tag{1.42}$$

These two diffusion coefficients are bound together by relation:

$$D_{self} = D\frac{\partial ln\ c}{\partial ln\ a} \tag{1.43}$$

$a$ is the activity and $c$ is the concentration [25]. If the hydrogen concentration is small, both diffusion coefficients are the same and there is no need to distinguish between them. When the hydrogen concentration is large, the system is strongly correlated and both equations has to be accounted [23].

The exact definition of self diffusion coefficient is following: It is a spontaneous mixing of 'molecules' taking place in the absence of the concentration, or chemical potential gradient. This type of diffusion can be followed using isotopic tracers, hence the name [25]. It does not lead to entropy increase and it take place under equilibrium.

Opposite to that, chemical diffusion occurs in a presence of concentration (or chemical potential) gradient and it results in transport of mass. The chemical diffusion is always a non-equilibrium process, increasing the systems entropy, and bringing the system closer to equilibrium [25].

When one possesses a diffusion equation, the next step is to find an appropriate fluctuation–dissipation theorem. For Brownian motion, after considering equipartition theorem, one gets:

$$\langle \xi(t)\xi(t') = 2(k_B T\Gamma m)\delta(t-t')\rangle \tag{1.44}$$

$\xi(t)$ is a fluctuating part of the force at given time $t$, $\gamma$ is a friction coefficient and $m$ is the mass of the Brownian particle. The diffusion coefficient turns out:

$$D = k_B T/\Gamma m \tag{1.45}$$

This model holds true for the metal–hydrogen system only at very high temperature, when the hydrogen acts like fluid (figure 1.12 (V)).

For the system studied here, thermally activated jumps are the leading process. Considering the Boltzmann type dependence: $\sim e^{-\frac{E}{k_B T}}$ makes perfect sense, since the H atom has to overcome the potential barrier, while the probability of occurrence at the top of it is given by the Maxwell–Boltzmann distribution. From figure 1.12 we can see, that real forms of diffusion coefficients contains the Boltzmann factor, though some pre-factors are present, depending on $m$ and $T$. The derivation of these diffusion coefficients can be found in [11].

# 2. Experimental Techniques

## 2.1 X-ray Diffraction (XRD)

The XRD is one of the most common technique in condensate matter research and will not therefore be described here in much detail. The XRD is either performed on monocrystals, or on polycrystals, which should ideally be in a form of a powder, for maximal accuracy. However, there is not always need for a sample to be ground into a powder, especially when we have a one, or two phases sample. The polycrystalline sample is therefore put in the diffractometer as it is. The sample's surface should be as clean as possible, since the X-rays do not have a large penetrability, and oxidized, or in other way contaminated surface would influence the measurement. However, the surface has to be brushed and cleaned carefully, since one can bring additional strain into the sample, which usually results in the broadening of diffraction lines.

We have measured our samples in ordinary Bragg–Brentano geometry, where the X-ray lamp and the detector point at the sample in joint angle $\theta$. The Bragg equation is:

$$2d_{hkl}\ sin\theta = \lambda \tag{2.1}$$

Where $\lambda$ is the wavelength of roentgen radiation used and the term $d_{hkl}$ stands for inner plane distances in given crystalline lattice. The resulting diffractogram is a spectrum over the angle $2\theta$. When the Bragg equation 2.1 is satisfied for a certain angle, a peak occurs in the spectrum. Its shape is best described as the convolution of Lorenz curve and Gaussian. The Lorentz curve arises from first principle statistical physics, and the Gaussian is a usual spectral function of a detector. This convolution is called the Voigt function; though for practical fitting it is usually replaced by a pseudo-Voigt function, which is a weighted linear combination of Lorenzian and Gaussian.

If a peak broadening occurs in a diffractogram, it can indicate two things. Either, the grains in the sample are small, or large amount of defects causing micro distortions of crystal lattice (dislocations) is present in the sample. Model, presented here: [26] is used to determine both properties. As so-called diffraction vector is defined as:

$$K_{hkl} = \frac{2\ sin\theta_{hkl}}{\lambda} \tag{2.2}$$

where $\theta_{hkl}$ is the diffraction angle belonging to certain plain system and $\lambda$ is the wavelength. We define the broadening of certain diffraction peak, usually as the full width at half maximum (FWHM) of the peak on certain $\theta_{hkl}$. This $\Delta\theta_{hkl}$ leads to $\Delta K_{hkl} = 2\Delta\theta_{hkl}\ cos\theta_{hkl}/\lambda$ for which following equation holds true [26]:

$$\Delta K_{hkl} = \frac{0.9}{D} + \xi b \sqrt{\rho} K_{hkl} \tag{2.3}$$

$D$ is the mean grain radius, $b$ is the Burgers vector, $\rho$ is the dislocation density and $\xi$ is a constant, depending on parameters of the model. If the dependence of $\Delta K_{hkl}$ on $K_{hkl}$ is plotted, a line should be the result. Inverse of the intersection with y axes is proportional to the mean grain size; square of the slope is proportional to the dislocation density.

The approximation 2.3 gives reasonable results. However, the curve should not, generally, be a line, since different dislocation systems (occupying different systems of atomic planes), has different $b$ and $\xi$. The general dependence is a broken line. Different models had to be employed if one is interested in exact numerical results. See [27] for exact models for hcp metals.

## 2.2 Vickers Hardness Test (HV)

This method uses a square based pyramid, made out of diamond, and constant force over certain time, to make a square-like indentation on the surface of the sample. The pyramid, also called indenter, has the include angle $136^0$. The Vickers microhardness HV is calculated bz the equation:

$$HV = \frac{F}{A} = \frac{2Fsin(360^0/2)}{d^2} \tag{2.4}$$

The $F$ stands for force, $A$ for the area of the indentation, and $d$ is length of its diagonals.

Similarly to the XRD measurement, the surface of our sample must be as smooth as possible and one must consider, that the surface can have different composition, then the bulk. Thin layers of oxidized substrate material are a common thing. Such layers must be removed, otherwise the hardness measurement would be influenced. At the same time, one must not introduce any additional strain, into the material, by brushing the surface too intensively.

## 2.3 Differential Scanning Calorimetry (DSC)

DSC is a primal techniques in thermal analysis. It has incredibly wide usage and can be used for examination of almost every material, from metal to polymers and generally amorphous materials, to food, or nanomaterials.

The technique measures, how the heat capacity of material changes by temperature. A sample of known mass is placed inside a device and is heated and/or cooled down. The heat capacity is tracked as changes in the heat flow. Phase

transitions of first and second kind are easily detected by DSC. However one must bear in mind, that possible non-equlibrium processes, such as overheating and supercooling, may occur within the first kind phase transition. The speed of heating and cooling must therefore be chosen wisely.

### 2.3.1 Difference Between Heat Flow & Heat Flux DSC

Historically, temperature transitions in materials were first seriously studied in the ceramic industry in the 1800s using DTA [28]. During this early work a thermometer was placed into a sample and it was heated in an oven; process similar to the way a meat thermometer is inserted in a meat while cooking. This arrangement lead to some serious problems, as the placement of the thermometer was rarely reproducible. This was solved by S. L. Boersma's development of a fixed thermocouple differential thermal analyzer [28]. One thermometer is placed in an inert material such as $Al_2O_3$, while the other is placed in a sample of the material under study. Analyzers of this design are still common today and are known under the name Differential Thermal Analysis (DTA).

In the 1960s a first double-furnace, or power controlled DSC was created in order to measure heat flow in and out of a sample, directly [28]. Such instrument must posses a feedback loop to maintain the sample at a defined temperature while the power needed to do this is measured against the reference furnace. This arrangement allows very precise control of temperature and accurate measurement of enthalpy (heat) and heat capacity. Because of its direct measurement of the heat flow, this instrument is called heat flow DSC.

DTA can also be used to calculate heat flow with the right calibrations. Such instrument is then called heat flux DSC. Because of its single furnace design, heat flux DSC is less sensitive to small transitions, heats and cools at slower rate than heat flow DSC, and give less accurate values for the heat capacity and enthalpy [28].

| | Heat Flow | Heat Flux |
|---|---|---|
| Fast Heating ($250^0C$/min plus) | Yes | No |
| Modulated Techniques | Yes | Yes |
| Accuracy of Cp Values | High | Moderate |
| Accuracy of enthalpy | High | Moderate |
| Easy for cleaning | Very | Moderate |
| Isotherm perforamnce | Excellent | Affected by sample |

Table 2.1: Differences between Heat flow & Heat flux DSC, according to [28].

## 2.4 Positron Annihilation Life-time Spectroscopy (PALS)

Positron Annihilation Life-time Spectroscopy is an extremely useful non-destructive technique, convenient for the inquiry of materials containing empty volumes. These empty volumes can be defects like vacancies, dislocations, VAC clusters, voids etc. These are just the most common objects detected by positrons. The idea of this technique is quite simple. We have a radioactive source of positrons. In our case it is a bit of $NaCl$ with radioactive sodium $^{22}Na$. It undergoes the $\beta+$ decay and creates positrons in reasonable rate. This positron creation is accompanied by a 1274 keV photon, which we detect and call it a START photon. A positron enters our sample and looses its kinetic energy until it reaches the thermalized state with the kinetic energy $E_k \sim \frac{3}{2}k_BT$. This process is called thermalization and the probability of annihilation during this time period is very small. After thermalization, the positron remains in the sample for some time. Its life and movements are in fact a stochastic process with certain expected value, called the positron life-time. It tells us, how long does it take for a positron to annihilate with an electron, that is present in the sample.

### 2.4.1 Positrons in Solids

Positrons, created by the common $NaCl$ positron source have continuous energy spectrum with the mean value around 270 keV [29]. The energy spectrum is continuous, since a neutrino, produced together with the positron, takes some energy too. The thermalized positron has the energy of 0.039 eV at room temperature. That is a great amount of energy that has to be lost. There are three main processes of energy loosing. In the high energy region ($> 100$ eV), positron undergoes an elastic scattering process on atomic nuclei and inelastic collisions with electrons. It excites electrons from lower levels into higher energy levels. This process takes around 1 ps. In the energy region $0.1 - 100$ eV the positron excites the valence electrons (conduction electrons in metals) by inelastic scattering. This process takes a few ps. Positrons with kinetic energies lower than 0.01 eV undergoes an elastic scattering on phonons. This is the longest phase and takes up to $\sim 10$ ps. The root mean square velocity of thermalized positron is:

$$v = \sqrt{\langle v \rangle} = \sqrt{\frac{3k_BT}{m_{ef}}} \tag{2.5}$$

The effective positron mass $m_{ef}$ is influenced by phonons, band electron structure and positron – electron interaction. In solids, the effective mass is $m_{ef} \sim 1.5\, m_{rest}$, the $m_{rest}$ being the rest mass of positron (electron) [29]. We therefore get for the root means square velocity in solids:

$$v[nm/ps] = 5.5\sqrt{T} \tag{2.6}$$

Thermalized positron diffuses throw the sample with the diffusion coefficient:

$$D \sim \frac{1}{\sqrt{T}} \tag{2.7}$$

The mean diffusion length is:

$$L \sim \sqrt{D\tau} \tag{2.8}$$

The $\tau$ is a de-localized positron's effective life-time. The de Broglie wavelength of a thermalized positron is:

$$\lambda[nm] = \frac{2\pi\hbar}{m_{ef}v} \sim 5.2\sqrt{\frac{293}{T}} \tag{2.9}$$

The region which is covered by a positron is therefore as large as $10^7$ atoms [29].

The positron life is ended by its annihilation with an electron. We introduce the positron annihilation rate $\lambda$ as the overlap of positron and electron densities, weighted by the so called enhancement factor $\gamma$:

$$\lambda = \int n_+(\vec{r})n_-(\vec{r})\gamma(n_-)\ d\vec{r} \tag{2.10}$$

The electron density is the sum of squared electron wave-functions, presented in the material:

$$n_-(\vec{r}) = \sum_{e_i<E_F} |\psi_i(\vec{r})|^2 \tag{2.11}$$

Where the summing runs over all occupied electrons states, i.e. up to the Fermi energy $E_F$. The positron density is the squared positron wave-function:

$$n_+(\vec{r}) = |\psi_+(\vec{r})|^2 \tag{2.12}$$

The correlation between positron and electron densities is positive, due to their Coulomb interaction, though an exact formula for the enhancement factor is unknown, similarly to the correlation factor in density functional theorem (DFT) calculations. The positron life-time is defined as the inverse positron annihilation rate:

$$\tau = \frac{1}{\lambda} \tag{2.13}$$

The positron wave-function in a perfect crystal lattice can be described as an ordinary plane wave. However, if defects, or open volumes in general, are present in the sample, they create a deep potential well for the positron, so the positron becomes trapped. The connection between the positron states in a

sample and detected positron life-times is described by so-called simple trapping model (STM) [29]. The time dependent probability of positron existence in a perfect lattice is given by exponential law:

$$n(t) = e^{-\lambda_B t} \tag{2.14}$$

The initial condition $n(0) = 1$ implicates, that only thermalized positrons can annihilate. If the sample contains single type of defects, trapping positrons, the kinetic equations for the trapping process are:

$$\frac{dn_B(t)}{dt} = -(\lambda_B + K_D)n_B(t) \tag{2.15}$$

$$\frac{dn_D(t)}{dt} = -\lambda_D n_D(t) + K_D n_B(t) \tag{2.16}$$

$n_B$ is the probability of positron being spread around the bulk, $n_D$ is the probability of positron being trapped by the defect. The symbol $K_D$ is the positron trapping rate from de-localized to localized state. The initial conditions are:

$$n_B(t = 0) = 1 \tag{2.17}$$

$$n_D(t = 0) = 0 \tag{2.18}$$

We assume the trapping here, to be permanent, so if once trapped, the positron annihilates in the defect. The general solution, to our kinetic equation is in the form:

$$n(t) = \left[1 - \frac{K_D}{\lambda_f - \lambda_D}\right] e^{-\lambda_f t} + \frac{K_D}{\lambda_f - \lambda_D} a^{-\lambda_D t} \tag{2.19}$$

Where $\lambda_f = \lambda_B + K_D$ is the disappearance rate of free positrons.

As mentioned before, the positron life-time is the measured quantity in PALS. The resulted positron life-time spectrum is a histogram of annihilation events, telling us, how many positrons had their life-time in certain time interval.

$$S(t) = -\frac{dn(t)}{dt} \tag{2.20}$$

The real positron spectrum is however influenced by the resolution function of the spectrometer. It also contains random background contribution and contribution from positrons annihilating in the source itself and the thin (usually Mylar) foil, separating the source, from the sample. Using STM one obtains by putting 2.19 into 2.20, positron life-time spectrum in the form:

$$S(t) = \lambda_f I_0 e^{-\lambda_f t} + \lambda_D I_1 e^{-\lambda_D t} \tag{2.21}$$

The relative intensity of the component representing the de-localized positrons contribution is:

$$I_0 = 1 - \frac{K_D}{\lambda_f - \lambda_D} \tag{2.22}$$

The relative intensity representing the contribution of positrons trapped in defects is:

$$I_0 = \frac{K_D}{\lambda_f - \lambda_D} \tag{2.23}$$

In case of a crystal containing N different types of trapping centres, the following positron life–time spectrum is predicted by the STM:

$$S(t) = \lambda_f I_0 e^{-\lambda_f t} + \sum_{j=1}^{N} \lambda_j I_j e^{-\lambda_j t} \tag{2.24}$$

The $I_0 = 1 - \sum_{j=1}^{N} I_j$ is the intensity of the contribution of de-localized positrons. The intensities of components representing contributions of positrons trapped by various defects are:

$$I_j = \frac{K_j}{\lambda_B - \lambda_j + \epsilon}, \quad j = 1, 2, ...N \tag{2.25}$$

$$\epsilon = \sum_{j=1}^{N} K_j \tag{2.26}$$

The trapping rate $K_j$ to j-th type of defect, is directly connected to the concentration of corresponding defects:

$$K_j = \nu_j c_j \tag{2.27}$$

The symbol $\nu_j$ denotes the specific positron trapping rate for certain type of defects, which describes how easily is the positron trapped by the defects. It is influenced by the local electron density and structure of the defect [29].

### 2.4.2 PAS Instrumentation & Data Analyses

The positron life-time measurements spectrometer consists primarily of two detectors, that are opposite to each other, with the sample and the radioactive source between them, and as close to each other as possible. The reason is to detect both, the start $\gamma$ and the annihilation $\gamma$ ray, each in one detector. Detectors consist of a scintillator optically coupled to photomultiplier. In our case, the scintillator is a high quality $BaF_2$ crystal, that transforms the $\gamma$ photon into UV light. The light is detected by the photomultiplier and a photo–electrons are created. Photo–electrons are accelerated by a strong electric field and multiplied by a system of dynodes. An electric pulse, with amplitude proportional to the

energy of the original $\gamma$ photon, is collected. The signal then has to be multiplied and checked if it pass into an energy window, set around values $1274keV$ and $511keV$ for the START and annihilation photons, respectively. The differences between START and STOP pulses are recorded and transformed to digital data.

The positron life-time is usually between 100 and 200 ps in bulk state of metals. Exact values for our sample will be given later. In a real spectrum, there are two other important components, that are always present. It is a component with the life-time of 368 ps and intensity around 8% representing a contribution of positrons annihilated in the $NaCl$ source spot and a component with the life-time of 1.5 ns, and intensity approximately 1% which comes from annihilations in a Mylar foil, covering the source. The ideal spectrum $S_{id}$ is convoluted with the resolution function of the spectrometer $R(t)$ and a constant background $B$ from random coincidences is always present.

$$S(t) = S_{id}(t) * R(t) + B \tag{2.28}$$

The resolution of the spectrometer used in the present work function can be described as a sum of two Gaussians.

There are many free parameters in the model function of a positron life-time spectrum, for every type of trapping center, there are two parameters: the positron life-time and the intensity. We therefore have to get some estimated values of these parameters. Those estimated values can either be calculated by DFT based calculations, or they can be measured on specially prepared samples. One can typically calculate the positron life-time for an ideal material, and a life-time for a vacancy and vacancies clusters. Calculation of life-time of positrons trapped at dislocations is more difficult and thus it is usually determined experimentally using a sample, that contains so many dislocation, that nearly all positrons annihilate trapped in dislocations.

Fitting of the experimental positron life-time spectrum is performed by non-linear least square method in a specialized program called plrf18 developed at the positron annihilation group at the Department of low-temperature physic. $\chi^2$ functional calculated as weighted squares of differences between the measured spectrum and model function 2.28 is minimized with respect to all parameters. A robust gradient based variable metric algorithm procedure MINUIT, developed in CERN, is used.

# 3. Ab-initio Calculations & Used Computational Packages

## 3.1 Two-Component Density Functional Theory

The problem of a positron trapping at defect is not just a particle occurrence in a potential well. It involves screening and charge transfer in a non-uniform system. It can be formulated in terms of a so-called two-component density functional theory [30].

The total energy of a system of interacting electrons and positrons moving in an external potential $V_{ext}$ can be expressed using a separation [30]:

$$\begin{gathered} E[n_+, n_-] = T_0[n_+] + T_0[n_-] + \\ \int V_{ext}(\vec{r})(n_-(\vec{r}) - n_+(\vec{r}))d\vec{r} - \int\int \frac{n_+(\vec{r})n_-(\vec{r'})}{|\vec{r}-\vec{r'}|} d\vec{r}d\vec{r'} + \\ \frac{1}{2}\int\int \frac{n_+(\vec{r})n_+(\vec{r'})}{|\vec{r}-\vec{r'}|} d\vec{r}d\vec{r'} + \frac{1}{2}\int\int \frac{n_-(\vec{r})n_-(\vec{r'})}{|\vec{r}-\vec{r'}|} d\vec{r}d\vec{r'} + \\ E_c^{e-p}[n_+, n_-] + E_{XC}[n_+] + E_{XC}[n_-] \end{gathered} \tag{3.1}$$

$n_+ \& n_-$ are the positron and electron densities, $T_0$ is the kinetic energy for non-interacting electron and positron gas, $E_c^{e-p}$ is the functional of positron–electron correlation energy and $E_{XC}$ is the exchange–correlation energy for positrons & electrons. By applying the general DFT procedure, we obtain following equation for electron and positron densities:

$$\frac{\delta E[n_+, n_-]}{\delta n_-} = \frac{\delta T_0[n_+, n_-]}{\delta n_-} + V(\vec{r}) = \mu_- \tag{3.2}$$

$$\frac{\delta E[n_+, n_-]}{\delta n_+} = \frac{\delta T_0[n_+, n_-]}{\delta n_+} - V(\vec{r}) = \mu_+ \tag{3.3}$$

$V(\vec{r})$ is the outside potential (from atomic cores). Details about the Two-Component DFT can be found in literature: [31] as the original work of Kohn & Sham; [32] dealing with large systems Hamiltonian diagonalization and [33, 34, 30], as works dealing with positron–electron systems directly.

## 3.2 Vienna ab-initio Simulation Package (VASP)

VASP is a large computational package for performance of ab-initio quantum molecular dynamics (MD). It uses ultra-soft pseudopotentials (PP) and projector-augmented waves (PAW) method with plane wave basis. The approach implemented in VASP is based on the finite-temperature local-density approximation (LDA) with the free energy as variational quantity. Exact evaluation of the instantaneous electronic ground state is performed at each MD time step. The ultra-soft PP and PAW allow considerable reduction of the number of plane-waves per atom, especially for transition metals and first row elements. Forces and the full stress tensor can be calculated with VASP and is used to relax atoms into their instantaneous ground-state [35].

Here are some characteristics of VASP that make it a powerful computational tool [35]:
• VASP uses the PAW method or ultra-soft PP. The size of basis-set can be therefore kept very small even for transition metals and first row elements like C and O. Generally not more than 100 plane waves (PW) per atom are required to describe bulk materials, in most cases even 50 PW per atom will be sufficient for a reliable description.
• VASP includes a full featured symmetry code which determines the symmetry of arbitrary configurations automatically.
• Computation time scale like $N^3$, where N is the number of valence electrons in the system. This is characteristic for all plane wave programs. In VASP, the pre-factors for the cubic parts are almost negligible, which lead to an efficient scaling with respect to system size. This is possible by evaluating the non local contributions to the potentials in real space and by keeping the number of orthogonalisation processes small. For systems with roughly 2000 electronic bands, the $N^3$ part becomes comparable to other parts of the code. Hence we expect VASP to be useful for systems with up to 4000 valence electrons.
• VASP uses traditional self-consistency cycle for the ground state search. Together with very efficient numeric methods of diagonalization (RMM-DISS, and blocked Davidson) it moves VASP among the fastest schemes currently available.

The most important files used by VASP are following [35]:
• INCAR: It is the central input file of VASP. It determines 'what to do and how to do it', and contains a relatively large number of parameters. Most of these parameters have convenient defaults, and a user unaware of their meaning should not change any of the default values.
• STOPCAR: Allows one to stop VASP during its execution.
• stdout, and OSZICAR: Information about convergence speed and about the current step is written to stdout and to the file OSZICAR. stdout file contains some additional technical parameters.
• POTCAR: It contains PP for every atomic specie used in the calculation.

• KPOINTS: It is an essential file for k-grid production. It contains the mesh size, or k-points coordinates and weights.
• IBZKPT: File compatible to KPOINTS file.
• POSCAR: File containing lattice geometry and positions of present ions.
• CONTCAR: It is a file produced at the end of every MD step. Sometimes it is possible to carry on from the CONTCAR file, if the VASP implementation was interrupted.
• CHGCAR: It contains the lattice vectors, atomic coordinates and the total charge density multiplied by volume.
• WAVECAR: A binary file that predicts wavefunctions computed in the next step.
• TMPCAR: Binary file for MD purposes.
• EIGENVALUE: It contains the Kohn-Sham-eigenvalues for all k-points, at the end of the simulation.
• DOSCAR: This file contains the density of states (DOS) and integrated DOS. The units are "number of states/unit cell"
• *PROCAR, PCDAT, XDATCAR, LOCPOT, ELFCAR, PROOUT, PRJCAR*: Usefull in some VASP versions only, or not important files.

The VASP manual [35] is very well written and contains all conceivable information. Also, given the extensiveness of this computational tool, it takes time and practice before one becomes able to use this tool by himself.

## 3.3 Program Pos330

This program allows one to compute positron life-times by solving the Schrödinger equation on a 3D mesh in the real space using the conjugate gradient method [33] and Kimball-Shortley iteration technique [36]. A preceding program *pos-new* was first introduced by Puska & Seitsonen [37] in 1995. Since that, some changes were implemented, though the basic structure remains. The implementation is being further developed by Jan Kuriplach at Charles University. The program has following structure:
• Reading the INPUT file in order to receive types and positions of atoms together with instructions for computation.
• Reading the atomic electron densities calculated by Desclaux's selfconsistent relativistic code [38, 39] from the file ATOM.
• Calculation of the Coulomb potential.
• Calculation of the correlation potential.
• Solving the Schrödinger equation for the positron to get the positron wave function and the energy eigenvalue.
• Calculation of annihilation characteristics.
• Production of OUTPUT file, including the computed values of life-time, energy, etc.
• (optional) Production of files *de&dp* containing electron and positron densities.

An example of INPUT file is presented bellow. A short explanation is given for each INPUT entry.
• ATSUP3.25: Version of the program.
• HEADER: Brief description of the calculation.
• SWITCHES: Modes of calculation. First switch is an ordinary ATSUP, Second switch switches on the high momentum component calculations (HMC), with momentum distributions.
• POSITRON: Specifics of the positron wave function.
• ENHANCE: Enhancement factor or correlation potential information, i.e. enhancement switch and dielectric constant.
• 3DMESH: Density of the mesh for calculation.
• MESHLIMIT: Parameters for 3D mesh reduction and potential boundary condition.
• BOUNDARY: Boundary conditions for all directions (symmetric, antisymmetric, vanishing).
• ATOM: Atomic numbers and shifts of the atomic positron potential for all atoms.
• LATTICE: Lattice constant, cutoff for potential generation, cutoff for the shift of the positron potential Units aa mean Angströms.
• VECTORS: lattice translation vectors. The program requires atoms coordinates in Cartesian frame.
• POSITIONS: Types and positions of all atoms.
• ITERATION: Parameters for conjugate gradient method. These are the number of iterations, resulting precision of energy in eV, preconditioning parameter, Kimball-Shortley check on, inverted potential switch, pseudo-random initialization - noise addition.
• OUTPUT: Options for 3D and HMC arrays output. ma is Matlab readable file, de, dp are 3D arrays of electron and positron densities.
• HMC: Parameters for the HMC calculations, e.g. maximum momentum in mrad units, number of points in p-mesh, 'wfminr' parameter, the cutoff for the wave function expansion and its units. au stand for atomic units.
• SAVERAGE: Direction of positron wave function expansion and number of points for spherical averaging of the wave around atoms.
• ORBITAL: Ranges of orbitals.
• WPARAM: Range of momentum for the W-parameter calculation in mrad units.
• RFUNCTION: Parameters of the energy resolution function of the detection system, here FWMH for one Gaussian.

```
ATSUP_3.25

HEADER    short description of data
          Ti, test version 3.25

SWITCHES  modes_of_calculation
           ATSUP
!          ATSUP   HMC2
!         SCALE
!         VASP

POSITRON  #levels energies    mass
          1       1.0         1.0

ENHANCE   enh_switch dieps_or_alpha
          BN  1.d20
!         SL  1.d20
!         SK  1.d20
!          GC  0.22

3DMESH    nr1 nr2 nr3
          100  100 100 0
!         10  10  10
!         24  24  24

MESHLIMIT mesh_reduction_(+-x,+-y,+-z), averaging_(x,y,z), energy
          0 0  0 0  0 0   0 0 0    0.0

BOUNDARY  BC_type_in_all_directions, init., average
           1  1  1   0 1
!         -1 -1 -1   1 1
!          0  0  0   1 1

ATOM      atomic_numbers_of_all_species
            22 1 0.00 0.00

LATTICE   lattice_constant cutoff sapcut units potnew? #min #max
!         6.23689 12.0    au
          2.9508  6.0  2.9508 aa 0 11 11

VECTORS   lattice_translation_vectors (in three lines)
           8.0  0.0     0.0
           0.0  6.9282  0.0
           0.0  0.0     6.351498

POSITION  types_and_coordinates_of_all_atoms
             1   0.000000000000000   0.866029977798462   0.000000000000000
             1   1.000000000000000   0.866029977798462   0.000000000000000
             1   0.500000000000000   0.000000000000000   0.000000000000000
             1   1.500000000000000   0.000000000000000   0.000000000000000
```

Figure 3.1: Structure of INPUT file of the Pos330 program, 1. part.

```
             2   4.500000000000000   3.464100000000000   2.778780438000000
             2   4.500000000000000   2.886749982833862   3.572717688000000
ITERATION #iterations precision preconditioning KSnew? init_s init_f
          500  1.d-12   0.01                    1        IP   0.1

OUTPUT    output_switches
          ma de dp

HMC       HMC_basic_parameters:  prmax npr wfminr cutoff2 units
          100.0  200    1.e-10   5.0  au

SAVERAGE  HMC_averaging_parameters: pdir(3)  nth nph
          0. 0. 0.   10 20

ORBITAL   orbital_info_for_hmc:
          1 9 1 7 1 1 1 1

WPARAM    range_for_W-parameter_calculation: p1 p2
          15. 25.

RFUNCTION resolution_function_parameters: FWHM
          4.0
```

Figure 3.2: Structure of INPUT file of the Pos330 program, 2. part.

# 4. Ultra-fine Grained Materials (UFG)

The size of grains effects affects strongly the properties of metallic materials. On one hand we have the mono-crystalline materials, which have immense usage in semi-conductor-base technologies, optical elements etc. On the other hand, there are techniques, like equal-channel angular pressing (ECAP) and high pressure torsion (HPT) under intense inquiry, whose purpose is to produce materials with as small grain size as possible.

The UFG materials exhibit the mean grained size typical bellow $1\mu m$. They experience very high strength and ductility. Due to their large fraction of grain boundaries compared to the whole volume, they bring completely new phenomena into physics, like the high diffusion activity and the low temperature super-plasticity. One has to distinguish between the UFG materials prepared by processes like HPT, or ECAP and condensate nano-materials, which exhibit the similar grain size, but possesses completely different properties. UFG materials prepared by aforesaid methods (also commonly called severe plastic deformation (SPL)) has no residual porosity and gas contamination, apart from the nano-materials prepared by powder metallurgy.

### High Pressure Torsion

The technique requires disc shaped samples. The sample is held between anvils, while the lower anvil rotates. Thus it is strained in torsion. One either applies defined pressure (of several GPa) for some time, or one allows the lower anvil to revolution couple times, till the process is terminated. The technique does not destroy samples [40]. The shear strain introduced to the sample by HPT after $N$ revolutions is estimated as:

$$\gamma = 2\pi N r/h \tag{4.1}$$

$r$ is sample radius and $h$ sample thickness. This implies, that the strain in a disc sample increases from the center to the perimeter. It was however proven, that with sufficient number of revolution, the strain becomes homogeneous [10, 9]. These experimental results agree well with the strain gradient plasticity model of HPT [41].

The techniques of HPT and ECAP are depicted in Figure 4.1.

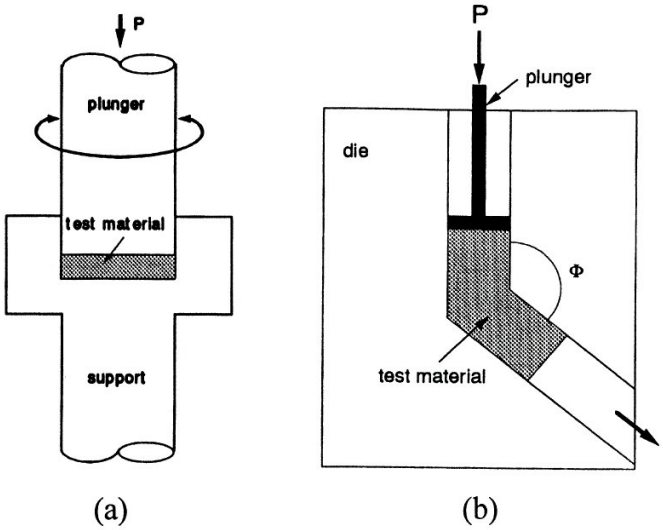


Figure 4.1: Schematic illustration of HPT (a) & ECAP (b) [10].

**Equal-channel Angular Pressing**

The ECAP is performed on samples having the shape of billets. The sample is passed through a special die several times. The angle between two channels is usually $90^0$ [40].

To compare the HPT and ECAP, there are two main differences. First we have mentioned, that HPT introduces strain inhomogeneously, while ECAP does it homogeneously. The other difference is, as has been proven, that HPT produces smaller size grains and higher fraction of high angle grain boundaries in a sample. The main advantage of ECAP is its ability to produce bigger samples, thus it is more suitable for industrial applications.

# 5. Hydrogen Loading

Generally, two different techniques are used in order to fill a metallic sample with H. The first technique consists of inserting the metallic sample in the $H_2$ atmosphere. As has been shown in the thermodynamic section, the H atmosphere works as a bath of certain thermodynamic variables. The temperature is left constant during the whole process. Pressure varies over time, but its variation only influence the speed of the loading. The last variable, that can be taken as constant throughout the process is chemical potential 1.4 of hydrogen, since it only depends on temperature and pressure.

The second loading technique is based on inserting the sample as a cathode into a specific solution, where $H^+$ carry the charge, when electric current is applied. $H^+$ ions are neutralized on the samples surface and then diffuse into the sample in the same way, as they do from the gas atmosphere.

### 5.0.1 Hydrogen Atmosphere Loading

Or H loading from the gas phase, in another formulation. The Figure 5.1 shows how the $H_2$ atmosphere loading is commonly done. The sample is surrounded by an atmosphere of certain pressure and temperature. Pressure decays over time, as the sample absorbs H. If the pressure reaches some minimal value, it is further adjusted to its initial value. Such steps are carried out, till the sample quits absorbing hydrogen, or till the process is turned off, of course.

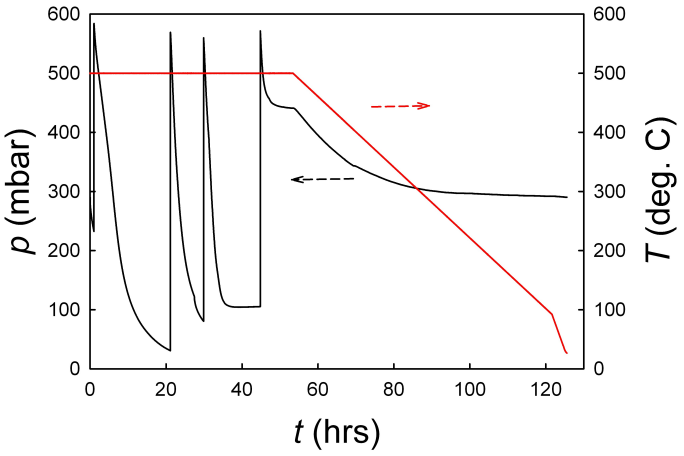


Figure 5.1: Typical progress of H loading from the gas phase.

### 5.0.2 Electrochemical Loading

If a metallic sample is inserted as a cathode into a solution with $H^+$ ions as charge carriers, those ions bombard the samples surface and they are neutralized and eventually absorbed by the metal. However, if the current is to high, there is also an concurrent process, of $H_2$ molecule forming. Those molecules then form a bubbles and leak from the solution. If the current is sufficiently low, only few atoms become adsorbed on the surface and the process of $H_2$ molecule forming is negligible. In that case, the Faraday's law can be applied, for calculation of adsorbed hydrogen.

$$m = AIt \tag{5.1}$$

where $m$ is the mass of hydrogen, $I$ is electric current, $t$ time and $A$ is a so-called chemical equivalent, which can be expressed from the second Faraday's law:

$$A = \frac{M_m}{Fz} \tag{5.2}$$

$M_m$ is molar mass, $z$ is the valency number (1 for $H^+$ ions) and F is a Faraday's constant, equal to a product of elemental charge and Avogadro number.

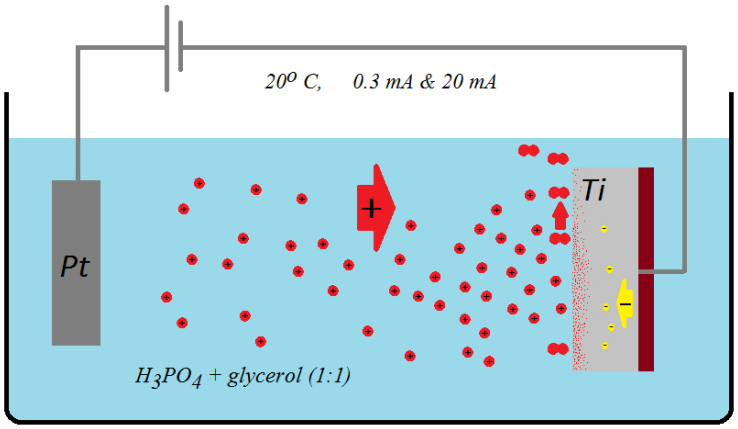


Figure 5.2: Electrochemical loading apparatus used in present work.

# 6. Samples Preparation & Characterization

## 6.1 Introduction

From this point, this thesis presents our own results, both theoretical and experimental. First, a description of Ti samples preparation and primal characterization shall be given in this very chapter. Then, in the following chapter, our theoretical calculations regarding the Ti-VAC-H system, shall be performed. In the last chapter, thermal stability of the Ti-H system shall be investigated.

Several specific Ti samples were prepared in our investigation. A simple coarse–grain (CG) Ti sample with minimum amount of defects was produced. UFG samples prepared by ECAP and HPT were produced later. These samples will be called virgin Ti samples. H loading was later performed on virgin Ti samples (both CG & UFG) in three modifications. All such treated samples were measured using mentioned experimental techniques in order to obtain their constitution and content of defects. This is the content of this chapter.

Positron lifetime spectroscopy (PALS) was employed for investigation of H-induced defects. PALS measurements were performed on a digital spectrometer [42] with time resolution of 145 ps (FWHM of the resolution function). At least $10^7$ positron annihilation events were collected in each PALS spectrum, which was subsequently decomposed into exponential components using a maximum likelihood method (see section 2.4.2). The contribution of positrons annihilated in the source has been always subtracted from measured PALS spectra.

Phase composition and lattice parameters of samples studied were determined by XRD measurements in the Bragg-Brentano symmetric geometry using Co $K_\alpha$ ($\lambda \doteq 1.79$ Å) radiation on D8 Advance (Bruker) diffractometer and Cu $K_\alpha$ ($\lambda \doteq 1.54$ Å) radiation on Xpert MRD (Panalytical) diffractometer.

The microhardness was measured by STRUERS Duramin-2 micro-tester. We measured the so called HV 0.5 & HV 1, which means that the load of 500 g (resp. 1000g) was applied on the indenter and it was applied for 10 s. Always 10 values were measured. The arithmetic mean was taken as the hardness of the material. The error of this measurement was taken to be the standard error of the mean.

Thermal stability of Ti samples and desorption of H were studied by simultaneous DTA and TG measurements carried out in a Setaram Labsys Evo apparatus. In this apparatus the DTA sensing trod is placed on a sensitive

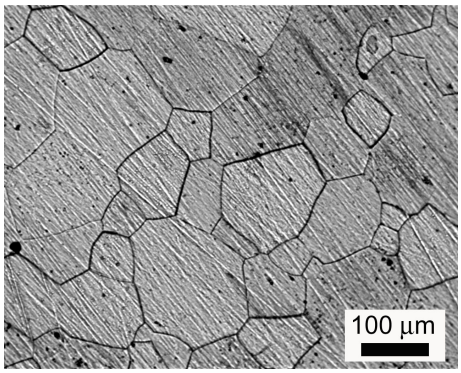


Figure 6.1: Initial Ti sample. Optical microscope photography.

balance. This enables simultaneous measurement of DTA and thermogravimetry (TG), i.e. to follow changes of the sample mass during the thermal treatment. Moreover the DTA apparatus is equipped with a quadruple mass spectrometer which enables analysis of gases evolved from the samples studied. The measurements were performed in a protective Ar atmosphere (20 ml/min).

## 6.2 Virgin Samples

### 6.2.1 Initial Samples & Annealing

Our starting Ti samples had commercial purity, which means they possessed about 99.7 % of Ti. They were naturally coarse–grained, with the mean grain size $\approx 150$ $\mu$m. Figure 6.1 shows a micro–photography of the initial Ti sample.

The starting Ti samples possessed some amount of dislocation, probably introduced to them during their preparation and slicing. This was revealed by PALS measurement, as the spectrum had two components. The first one was the component from positrons annihilating in defect–free lattice. It had a life–time matching the calculated positron life–time in bulk state $\tau_{bulk} = 146.8$ ps (see the section dealing with performed calculations). The second component had a positron life-time matching the value $\tau_{disl} \approx 172 \pm 3$ ps. $\tau_{disl}$ was obtained by measuring a Ti sample, previously subjected to cold rolling. Such sample was rolled to 30% of its initial thickness. Thus big amount of dislocations were introduced into the sample and it possessed one component positron spectrum, characterized by this positron life-time [9].

Dislocations in starting samples had to be removed, before other treatments would be employed. We have used HV measurement (HV 1) and isochronal annealing to determine an ideal temperature and time, when the samples posses

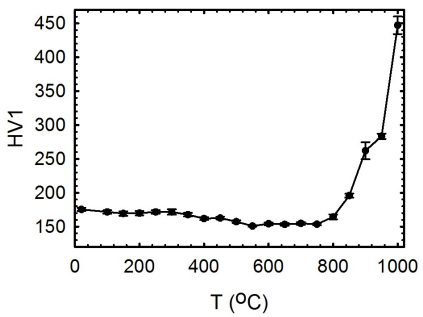


Figure 6.2: Isochronal annealing of initial Ti sample with hardness measurements.

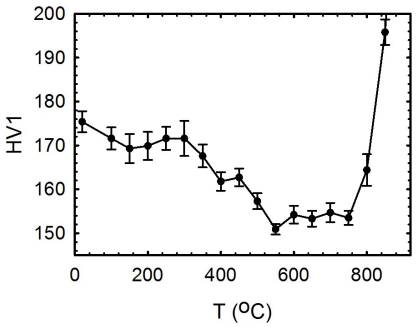


Figure 6.3: The same Figure zoomed.

minimal hardness and therefore minimal amount of defects. We used steps of $50^0$C and annealing for 50 minutes on each temperature. Temperature of minimal hardness was settled to be $550^0$C. One can see in figure 6.2 that the hardness is lowered with increasing temperature till this temperature. After that, short plateau occurs and from the temperature of $750^0$C, the hardness rises rapidly. It is caused by oxygen penetration of the sample. The issue of titanium's affinity to atmospheric gases shall be treated later in this chapter. It was a permanent difficulty, influencing our measurements. The time sufficient for the complete disappearance of defects by annealing was settled on two hours. After that the sample suffered from oxygen penetration.

Annealing in Earth's atmosphere at $1000^0$C causes large oxygen penetration, and change of structure, however annealing in vacuum ($10^{-3}$ mbar) leads to pure, defect free Ti sample. PALS measurement performed on this sample had one component spectrum with the mean life–time $144.6 \pm 0.6$ ps. PALS measurement performed on the sample, which was annealed in Earth's atmosphere at the temperature $550^0$C for two hours, did not revealed any defects either and had the mean life–time $145.0 \pm 0.8$ ps.

Another isochronal annealing with simultaneous HV measurements (HV 0.5) was performed on two Ti samples. We decided for HV 0.5, since its results were less subjected to fluctuations. The first sample was previously annealed in vacuum on temperature $800^0$C for two hours. The other one was the starting Ti sample, witch possessed some amount of defects from its production and slicing. The results can be seen in Figure 6.4. We have again proven, that the temperature when defects can be annealed in Earth's atmosphere is $550^0$C.

The XRD was measured on the annealed sample ($500^0$C, 2 hours). It detected the hcp structure of $\alpha$-Ti. The diffractogram is in figure 6.5. Peaks are very narrow, indicating very low concentration of dislocations and large grains.

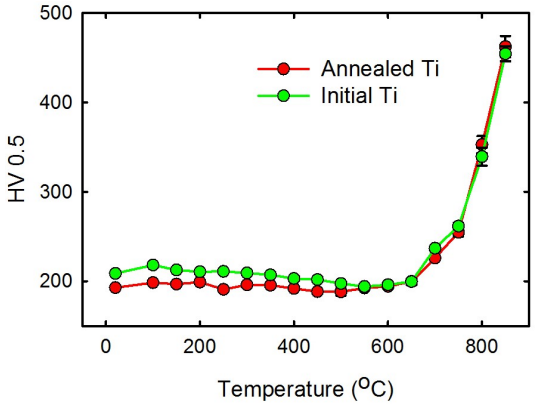


Figure 6.4: Isochronal annealing with HV 0.5 measurement of a starting Ti sample and sample previously annealed.

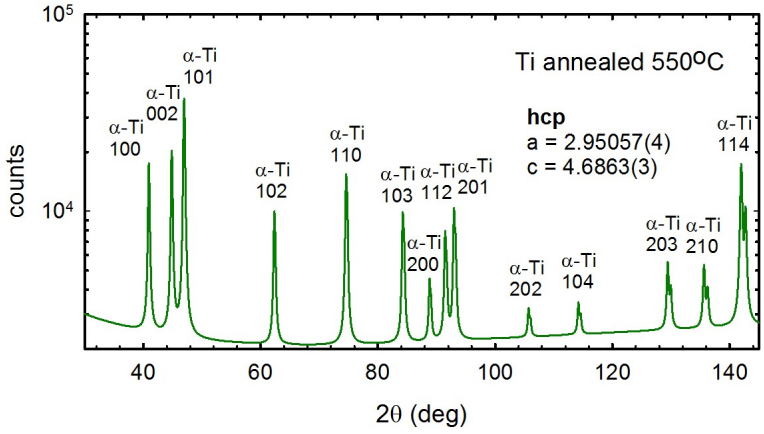


Figure 6.5: Fitted diffractogram of annealed Ti. Detected structure with lattice parameters in Å.

### 6.2.2 Titanium and Atmospheric gases

As was mentioned in the introduction, Ti is valued for its chemical stability at low temperatures. However at higher temperature, Ti reacts rather willingly with atmospheric gasses [15]. Both oxygen and nitrogen are $\alpha$-phase stabilizers, that means the $\alpha$-Ti can exist at much higher temperatures, than 882°C, with a small addition of oxygen, or nitrogen. See phase diagrams 6.6 & 6.7.

The diffusion coefficient of oxygen in titanium is 2 orders of magnitude higher

than nitrogen, and 4 orders of magnitude higher than titanium self-diffusion coefficient [14]. The current technical literature establishes the temperature of $600^0$C as the temperature, when oxygen penetrates Ti and can cause embrittlement. It is therefore not meant to be used, without any protection at higher temperatures [2]. Bellow this temperature, oxygen passivates the surface of Ti and protects it in a way [14].

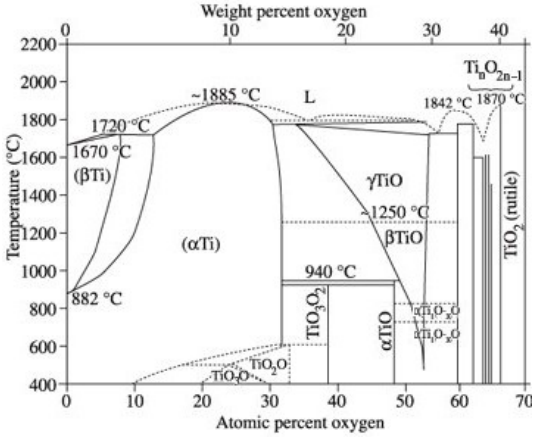


Figure 6.6: Phase diagram of Ti-O system [15].

Titanium and its alloys have a great affinity for nitrogen. The equilibrium nitrogen pressure for the Ti-N system is lower than $10^{-25}$ Pa [14]. Surface experimental techniques and theoretical calculations have shown, that N atoms take place under the first layer of Ti atom [14]. The Ti sample then receives a typical golden – like color of TiN. We have experienced that, when annealing our Ti samples in Earth's atmosphere at temperatures roughly $(400 - 600)^0$C. At higher temperature, a blue color took place. At temperature higher than roughly $850^o$C, the color changed to gray, which clearly belongs to Ti oxides. Sometimes also thin, extremely brittle white layers, occurs on the surface of Ti. They were reported many times [14] and are made out of Ti oxides. The true composition of the blue color surface remains unknown to us.

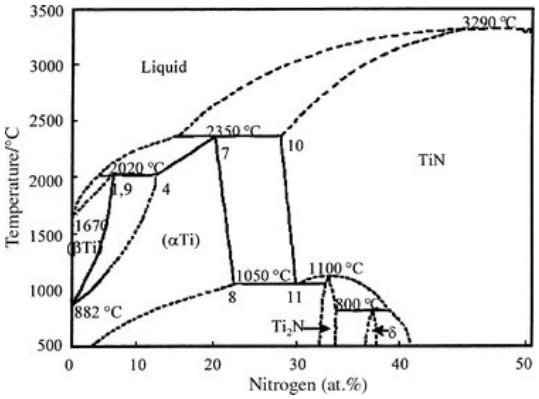


Figure 6.7: Phase diagram of Ti-N system [14].

### 6.2.3 UFG Materials Characterization

Ti samples subjected to ECAP and HPT were studied in this work. ECAP samples were prepared by 1 to 10 passes through a die at temperature $300^0$C. Figure 6.8 shows the surface of ECAP Ti, prepared by 6 passes. Back-scattered electrons in electron microscope determined the mean grained size to be $\approx 500$ nm.

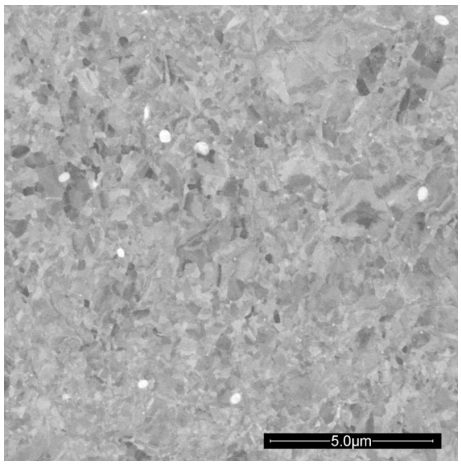


Figure 6.8: ECAP Ti (N=6). Electron microscope image.

The fine–grained structure leads to very high hardness of the material. The hardness HV 0.5 was measured on two ECAP samples during isochronal annealing. The annealing time was 50 minutes and the temperature step $50^0$C, the same as in the case of the starting Ti sample, discussed in the previous section.

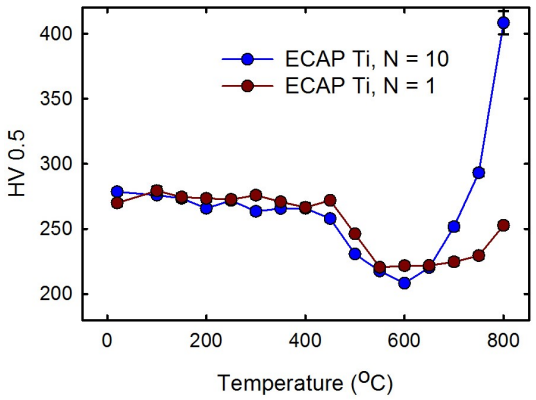


Figure 6.9: Isochronal annealing of ECAP Ti, produced by passing a Ti sample 1 and 10 times through a die.

From figure 6.9 one can see, that the number of passes does not influence the hardness much. Both curves in Figure 6.9 have similar development up to temperature of $650^0$C. After that, one rises more rapidly than the other. It is caused by different way of packing the sample in an ironic protection foil, which was used during the annealing in Earth's atmosphere. If packed carefully, the foil is able to slow down the oxygen penetration of annealing Ti sample.

The most important result of the isochronal annealing in figure 6.9 is the temperature, when the fine-grained structure starts to restore. The hardness decreases evidently after the temperature $450^0$C. Considering the finite time of annealing (50 minutes), the temperature $400^0$C was settled to be a safe temperature for thermal processing of ECAP Ti. This temperature was later used during H loading of ECAP Ti.

The PAS measurement were performed on ECAP and HPT samples. Figure 6.10 shows the dependency of defects positron life–time on number of passes (N), figure 6.11 shows intensities of detected components. Similarly to the HV measurement; life–times and their intensities do not vary much with the number of passes.

A HPT Ti sample was prepared by applying the pressure 6 GPa and making 5 revolutions. It exhibits grain size around 150 nm. It was measured by PALS too, with results in figures 6.12 and 6.13. In case of HPT samples, the structure varies from the axis of the revolution to the perimeter. The PALS measurement was made with moving the positron source (which can be very small) around the sample. Thus the development from the axis to the perimeter was measured.

The HV measurement is in figure 6.14. It was performed in a similar way as PALS. From the revolution axis to the perimeter, the hardness was measured.

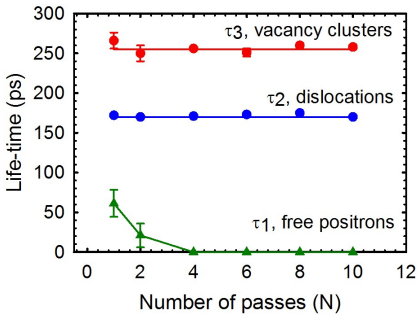


Figure 6.10: Positron life–times in ECAP Ti samples. One to ten passing through the die.

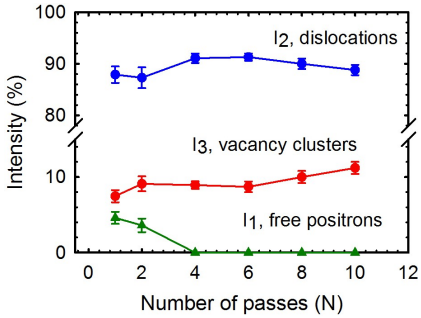


Figure 6.11: Intensities of detected positron components.

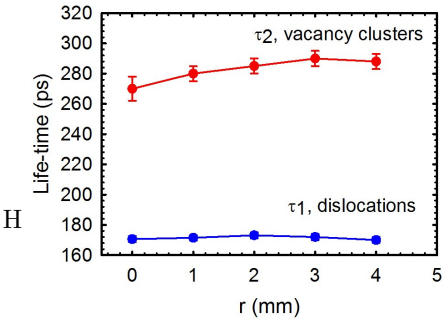


H

Figure 6.12: Positron life–times in HPT Ti sample. Development from the revolution axis to the perimeter.

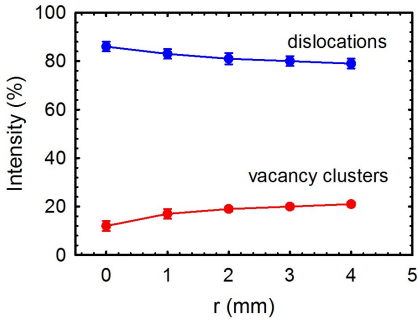


Figure 6.13: Intensities of detected positron components.

Figure 6.14 gives mean values of hardness. Another measurement in real space was performed. Figure 6.15 shows a quarter of cylindrical sample introduced to HPT. The hardness was measured throughout the whole slice. This measurement gives a great insight onto the homogeneity of samples prepared by HPT.

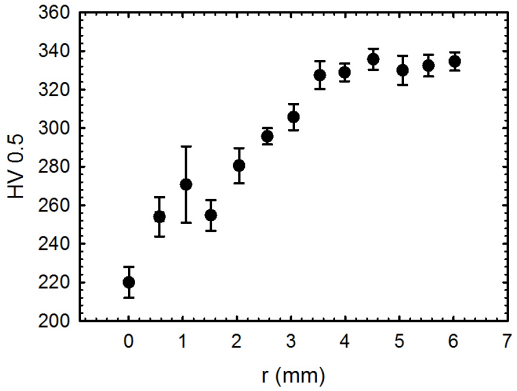


Figure 6.14: Hardness measurement of HPT sample from the revolution axis to the perimeter.

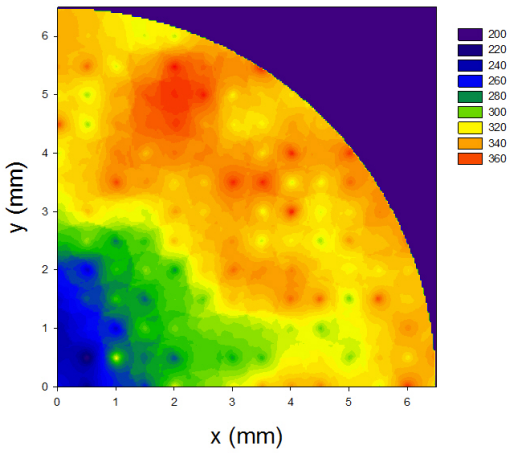


Figure 6.15: Hardness measured on HPT sample in a real slice.

Diffracrograms of ECAP and HPT Ti can be seen in figures 6.16 and 6.17. Peaks are noticeably wider, indicating the fine–grained structure and/or large amount of dislocations.

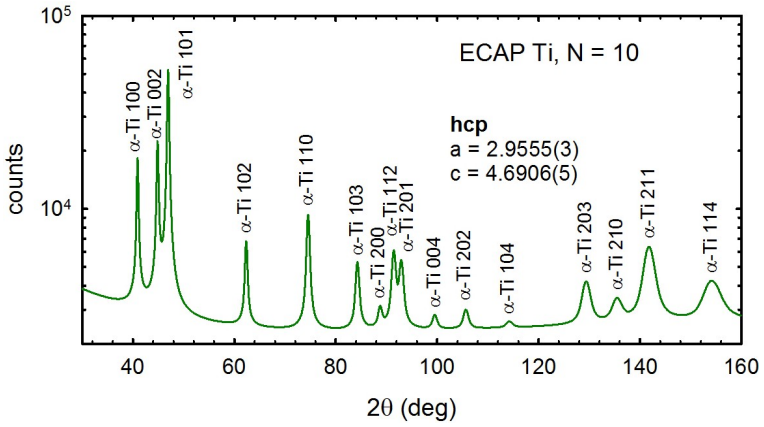


Figure 6.16: Fitted diffractogram of Ti subjected to ECAP. Detected structure with lattice parameters in Å.

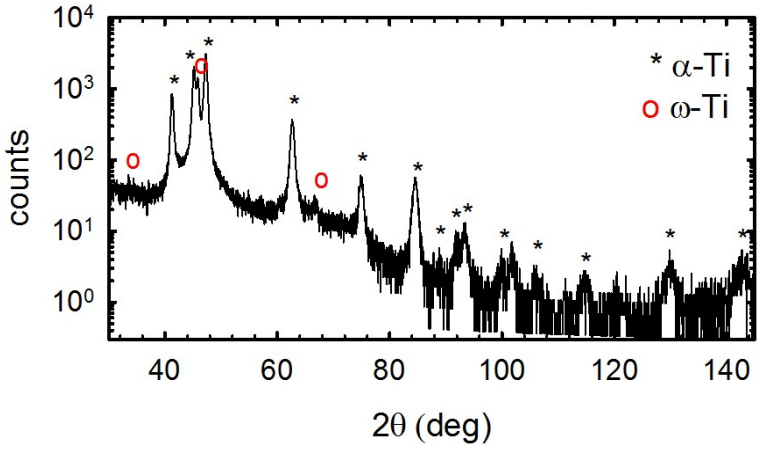


Figure 6.17: Diffractogram of Ti subjected to HPT.

Figure 6.17 shows, that HPT applyed on $\alpha$-Ti can lead to martensitic transformation $\alpha \rightarrow \omega$, discussed in the section 1.2.3. This proves, that HPT is capable of introducing even larger internal strain, than ECAP [8].

## 6.3 Hydrogen Loading of Virgin Samples

### 6.3.1 Electrochemical Loading

Following articles: [43, 44, 45] deal with electrochemical loading of $\alpha$-Ti. We performed the loading procedure at room temperature. $H_3PO_4$ and glycerin in

ration 1:1 were used as electrolyte. We used annealed, defect free Ti sample and Ti sample subjected to ECAP, as the cathode. The anode was pure platinum made (99.99% purity). We used electric current of 20 mA. An area of $1cm^2$ of the cathode was in contact with the solution, it was always one side of the samples. The other side was isolated and a wire was brought through the isolation. The apparatus was presented in previous chapter in Figure 5.2.

It is fair to mention, that the adsorption of H for different elements is different in the same solution. It is therefore sometimes useful, to deposit thin layer of specific material on the surface of the sample, one wants to load with H. Material with large H enhancement probability is definitely palladium. It catalyzes strongly the $H_2$ molecule dissociation and can therefore limit the bubbles creation and support the hydrogen atoms diffusion into the cathode [11]. We made an attempt to cover our titanium samples with palladium and thus improve the loading process. However this was not in any use, since the palladium quickly transformed into its hydride. This hydride has larger volume, than the pure palladium. A large strain was introduced into the layer and it became blistered and eventually fell of. We therefore did not use this technique any more and used only cleaned and brushed titanium samples.

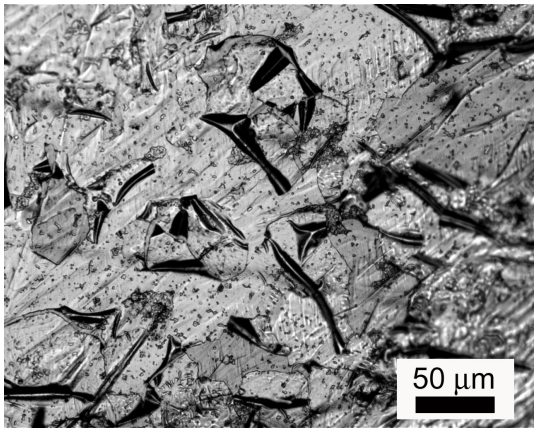


Figure 6.18: Surface of Ti with deposited Pd layer after electrochemical doping. Light microscope micro-photography.

An annealed, defect free Ti sample was loaded electrochemically for 239 hours. The composition was measured by XRD on the loaded site and on the opposite site. Resulting diffractogram is in Figure 6.19. The loaded site was completely transformed to $\delta$-hydride, while the opposite site remains almost pure $\alpha$-Ti. It implies, that the H diffusivity in the $\alpha$-Ti is very low at room temperature. Also the layer of $\delta$-hydride on the loaded site is quite homogeneous and peaks width indicate low amount of dislocations. There is a photography of the thin layer of $\delta$-hydride in figure 6.20. We can see, that it is several $\mu$m thick.

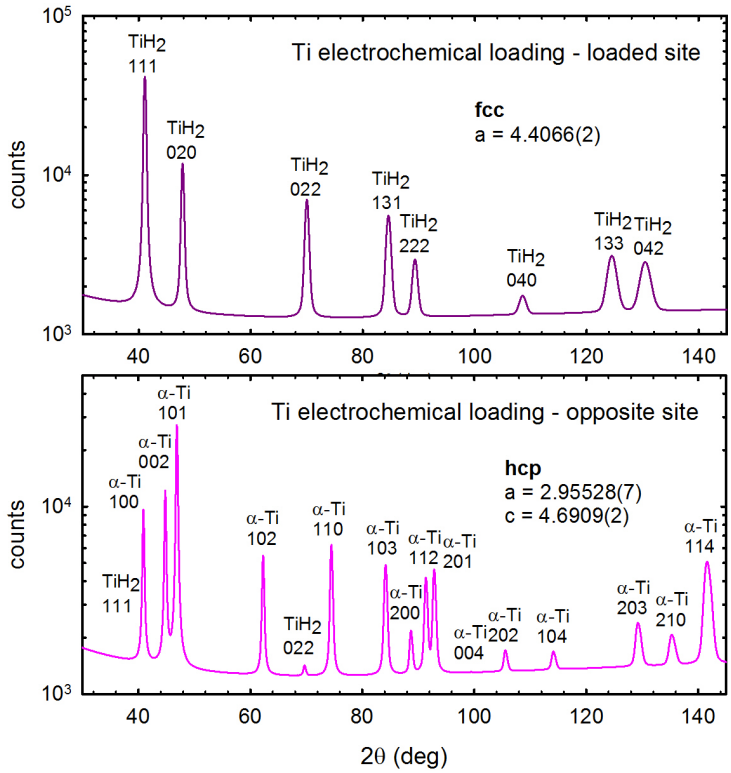


Figure 6.19: Fitted diffractogram of electrochemically loaded CG Ti, both sides. Structures detected, with lattice parameters in Å

PALS measurement was performed on the same, electrochemically loaded CG Ti sample. See figure 6.21. Large amount of dislocations were introduced into the sample during first 68 hours of loading. Some others added up during the next 171 hours. Some amount of VAC clusters occurred during the process too. Their size increased with time. PALS is a bulk technique and therefore the results hold for the sample as whole, not sample sides separately.

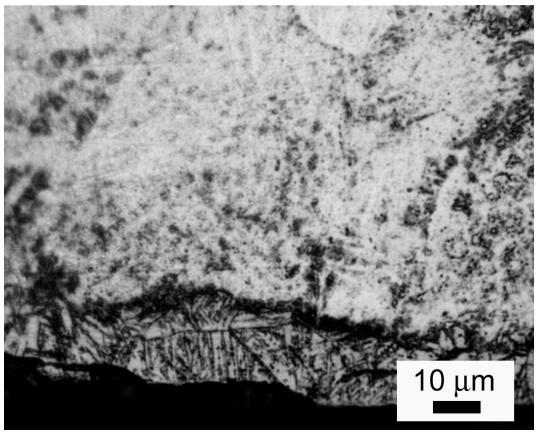


Figure 6.20: The layer of $\delta$-hydride arising on the surface of electrochemically loaded CG Ti sample.

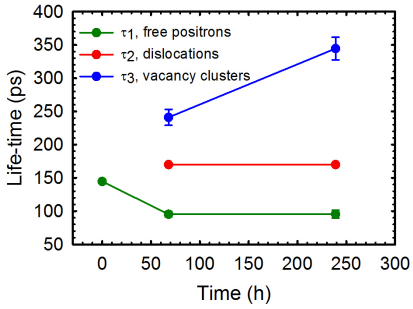


Figure 6.21: PALS measurements over time of electrochemically loaded CG Ti sample.

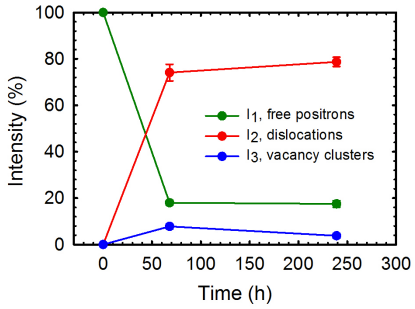


Figure 6.22: Intensities of detected components.

Similarly to PALS development over time, HV was measured. See figure 6.23. The hardness raised even at the opposite site. At the loaded site, the hardness rises continually with time.

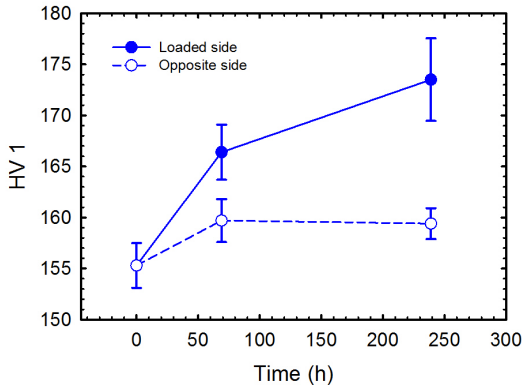


Figure 6.23: HV measurement of electrochemically loaded sample.

## 6.4 Loading from Gas Phase

It has been proven, that by applying high temperature, complete transformation from $\alpha$-Ti to $\delta$-hydride is possible in reasonable amount of time (hours) [46, 47]. Indeed, figure 6.24 shows a diffractogram of CG Ti sample, loaded at $500^0$C for 50 hours. The sample was completely transformed to $\delta$-hydride.

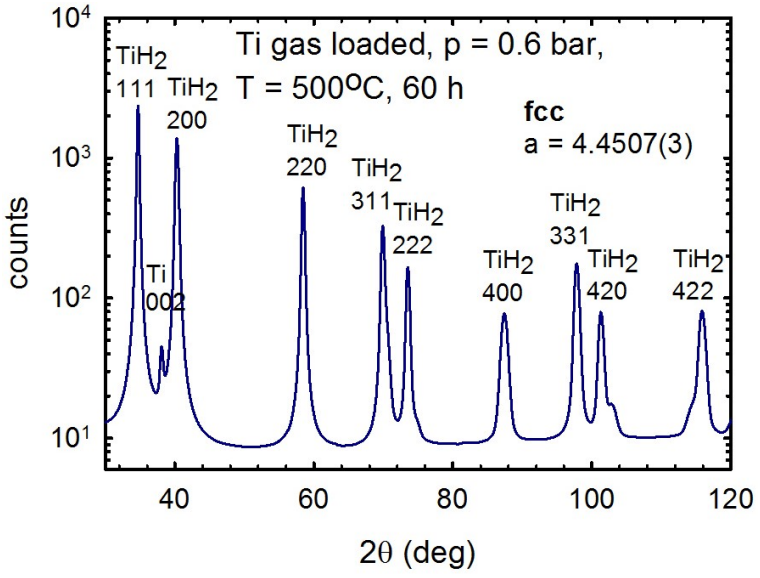


Figure 6.24: Diffractogram of CG Ti sample, loaded from gas phase. Structure detected, with lattice parameter in Å.

The reason for the complete transformation of a CG Ti sample is that temperature around $500^0C$ makes the diffusion of H atoms large enough to allow the H to spread throughout the whole sample. At this temperature, the solubility of H in $\alpha - Ti$ reaches its maximal value $\approx 8$ at.%.

The $\alpha$-Ti interstitial alloy is the first step of $H_2$ atmosphere loading at high temperature. When the maximal solubility is reached, grains of $\beta$-Ti occur. Later, when the concentration of approximately 50 at. % is reached, grains of $\delta$-hydride occur. Regardless of how much hydrogen will eventually be absorbed, the slow cooling to room temperature causes all parts of the sample to transform to either $\alpha$-Ti or $\delta$-hydride. These two phases are then detected by XRD.

The CG Ti sample obtained by $H_2$ atmosphere loading contain cracks. It can be seen in figure 6.25 and 6.26. The more H the sample absorbs, the more cracks are produced.

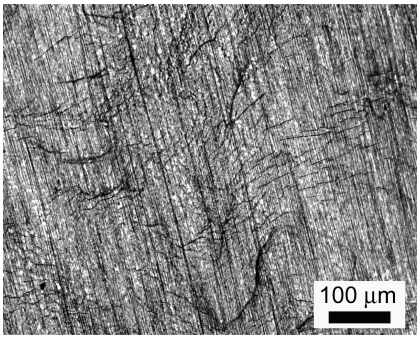


Figure 6.25: Micro-photography of the Ti surface after loading in $H_2$ atmosphere ($500^0C$, 0.6 bar) for 1 hour. Cracks present.

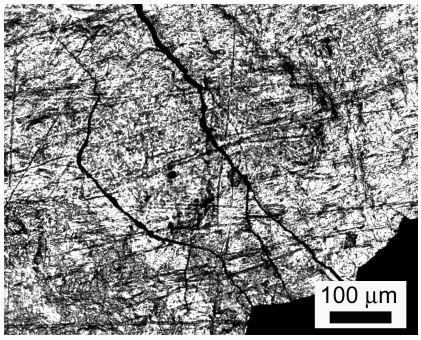


Figure 6.26: Micro-photography of the Ti surface under the same condition for 50 hours. Amount of cracks increased.

When the behaviour of CG Ti samples during gas phase H loading was known, samples subjected to SPD were investigated. As was proven, in the section 6.2.3, at temperatures only up to $400^0$C, is the UFG structure stable. Therefore, the temperature $500^0$C, used for the CG Ti loading could not have been used for UFG samples.

The investigation was made, how the loading time influences the constitution of the resulting sample. CG & UFG Ti samples were loaded in $H_2$ atmosphere of pressure 1 bar, at $400^0$C for 5, 10 and 15 hours. They were measured by XRD. Diffractograms after loading for 5 hours are presented (figures 6.27 & 6.28). The evolution of $\alpha$-Ti/$\delta$ constitution is in figure 6.29. The weight concentration of the $\delta$-hydride plotted against time. As one can see, the transformation in ECAP

sample was much faster, due to the diffusivity of H around grain boundaries.

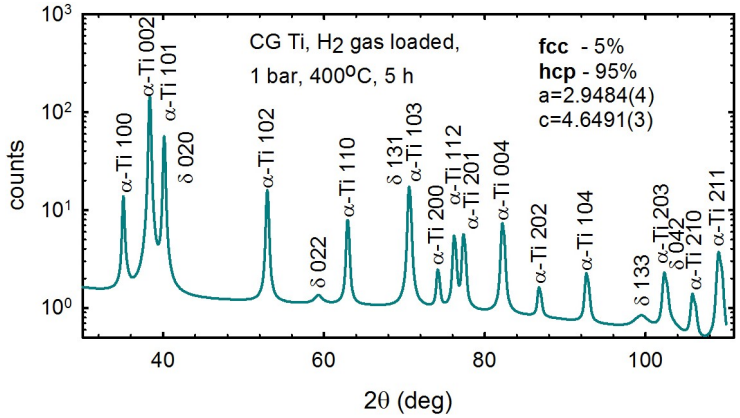


Figure 6.27: Diffractogram of CG Ti, loaded at $400^0$C for 5 hours.

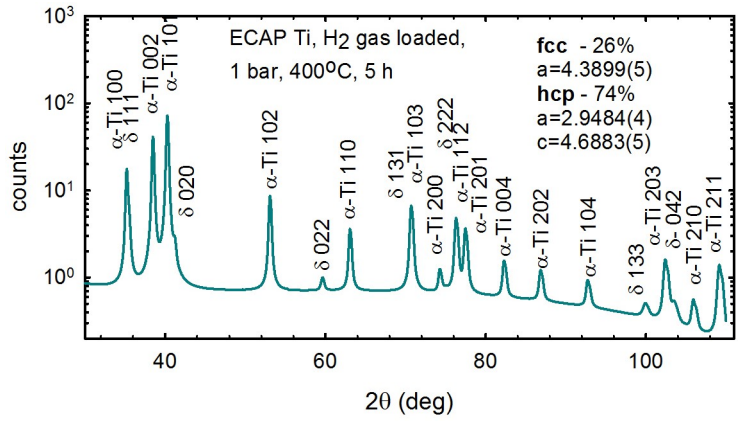


Figure 6.28: Diffractogram of CG Ti, loaded at $400^0$C for 5 hours.

The H loading from gas phase at temperatures like $400^0$C leads to very different results, compared to the electrochemical loading. It is however possible to imitate the electrochemical loading by loading from the gas phase of high pressure and low temperature. The pressure equivalent in a solution, fugacity, is really high during the electrochemical loading of $I = 20$ mA current applied.

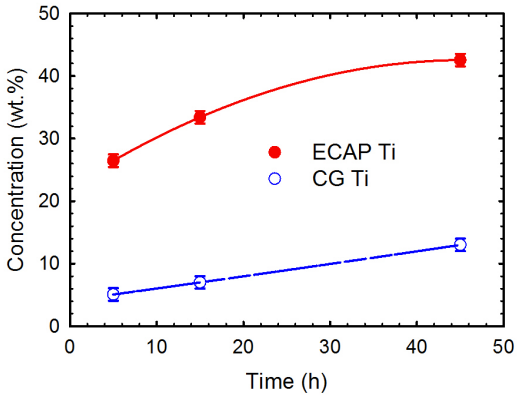


Figure 6.29: Weight concentration of $\delta$-hydride over time. CG & UFG Ti samples loaded at $400^0$C in 1 bar $H_2$ atmosphere.

We have performed loading from $H_2$ gas phase on both CG & UFG sample. Diffractograms of resulting samples are in figure 6.30 & 6.31. As one can see, the HPT sample is able to absorb much more H during the same time of loading, than the CG Ti. This against proves the assumption, that the diffusivity in UFG Ti is be much higher than in CG samples.

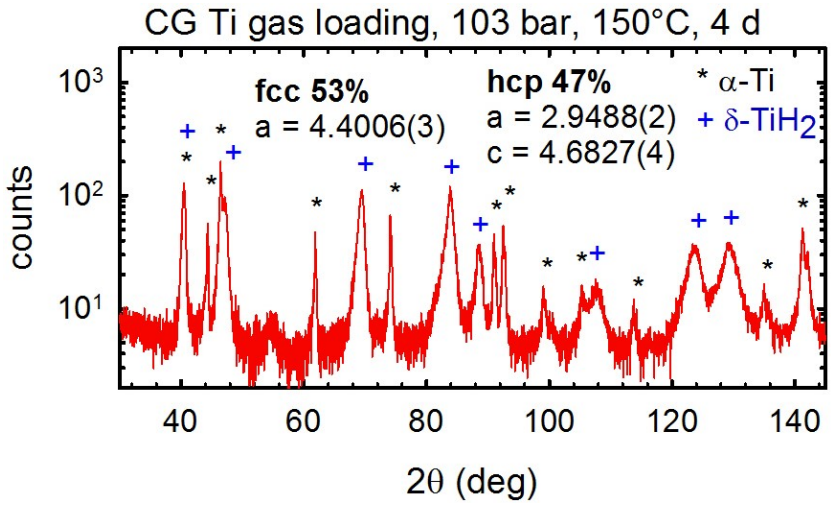


Figure 6.30: Diffractogram of CG Ti sample, loaded in $H_2$ atmosphere.

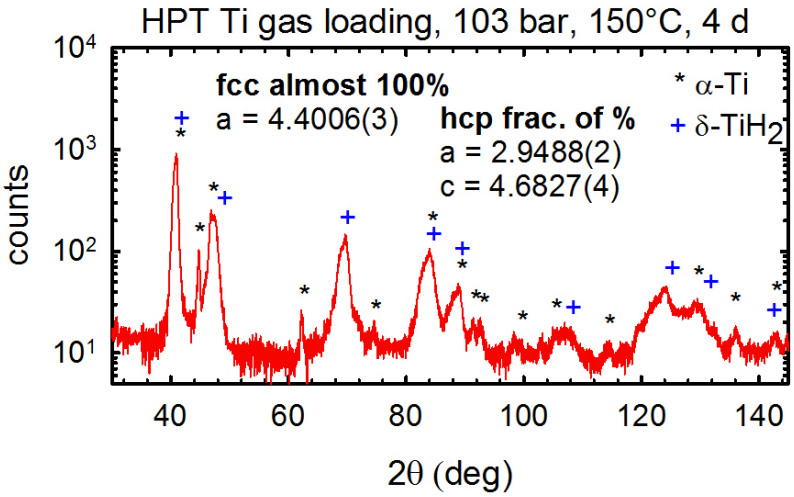


Figure 6.31: Diffractogram of HPT Ti sample, loaded in $H_2$ atmosphere.

The figure 6.32 shows the surface of CG Ti sample loaded at low temperature and high pressure. One can see a non-homogeneous layer of $\delta$-hydride, that has arisen on $\alpha$-Ti substrate. Figure 6.33 shows the layer on a cut. The result is very similar to electrochemically loaded sample in figure 6.20.

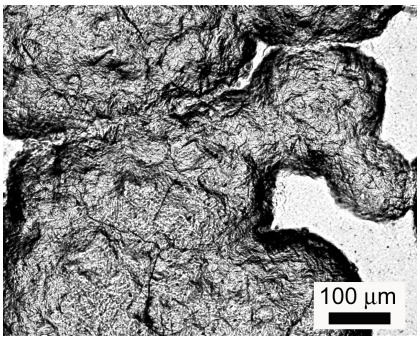


Figure 6.32: Micro-photography of the Ti surface after loading in H atmosphere ($150^0C$, 103 bar) for 4 days.

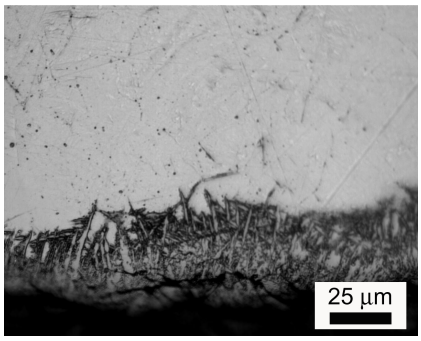


Figure 6.33: The same sample photography on a cut.

## 6.5 Summary

This chapter has shown, how initial Ti samples can change after specific types of treatment. We can summarized that as:

• It is possible to remove most of structural defects from Ti sample by annealing it in Earth's atmosphere at 550$^o$C, or in vacuum at arbitrary higher temperature.
• Ti subjected to ECAP experience great hardening. Typical grain size after ECAP is $\approx$ 500 nm. The final sample contains large amount of dislocations and some amount of VAC clusters.
• Ti subjected to HPT also experience great hardening. Typical grain size is $\approx$ 150 nm. The final sample has similar content of defects like ECAP Ti. Sometimes, a high pressure phase $\omega$, occurs in the sample.
• UFG samples are more easily loaded with H, since H can diffuse around grain boundaries.
• The loading temperature for UFG samples should not exceed 400$^0$C. Higher temperature causes the UFG structure to restore.
• It is possible to transform whole CG Ti sample to $\delta$-hydride, if it is loaded from gas phase at 500$^o$C and pressure even below 1 bar. Some amount of cracks is introduced into the sample, though it is not heavily damaged.
• Electrochemical and low temperature gas phase loading cause a thin layer of CG Ti sample to transform to $\delta$-hydride, while the rest of the bulk remain $\alpha$-Ti.
• It is possible to transform whole UFG Ti sample to $\delta$-hydride, by loading it electrochemically, or from gas phase at low temperature.
• Loading UFG Ti sample at 400$^0$C in 1 bar $H_2$ atmosphere cause quick transformation to $\delta$-hydride, while loading CG Ti at at the same conditions, cause very slow transformation to $\delta$-hydride. The diffusivity in CG Ti is at 400$^0$C noticeably smaller than at 500$^0$C.

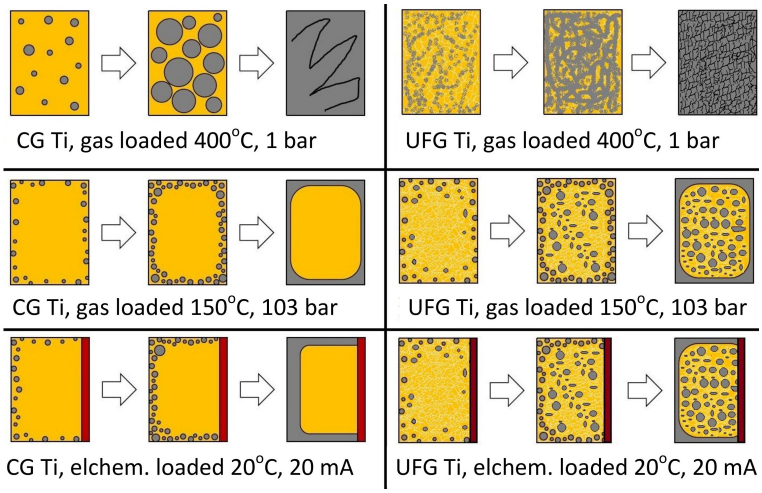


Figure 6.34: Differences between CG and UFG loaded samples.

• Figure 6.34 qualitatively shows the time evolution of loaded CG and UFG Ti samples. Left side belongs to CG samples and the right side to UFG samples. The arrows represent time development, however another time scale is considered

in individual situations. The UFG structure cause quick diffusion of H into the whole sample at all loading conditions used. Transformation then take place in the whole bulk simultaneously.

• Arisen $\delta$-hydride has different lattice parameter after loading in different conditions. The results are presented in figures 6.35 and 6.36. The second figure shows the lattice parameter evolution with time, when loading at $400^0$C in 1 bar.

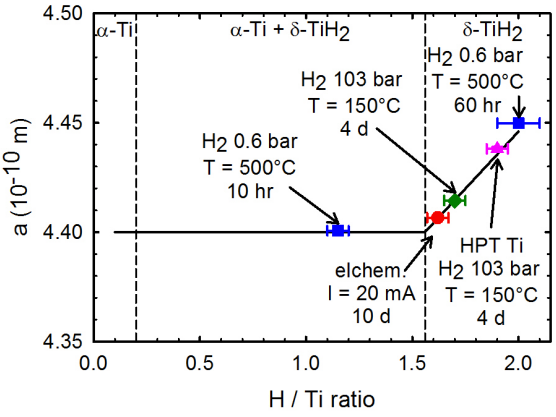


Figure 6.35: Obtained values of $\delta$-hydride lattice parameter from loaded Ti samples.

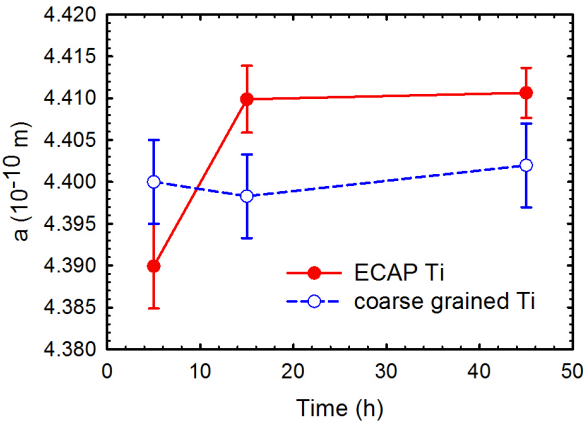


Figure 6.36: $\delta$-hydride lattice parameter evolution in CG & ECAP Ti samples loaded at $400^0$C.

# 7. Theoretical Simulation of the Ti–VAC–H System

It was very beneficial for this work, to calculate energies and positron life-time of specific crystal arrangements, containing Ti and H atoms and VAC. Some calculations were even fundamental, since the results served as input values for PALS spectra processing. Calculated energies were compared to each other and thus formation energies and binding energies of space arrangements could have been obtained. A small grid of 216 (N) atoms was used and following energies were calculated by VASP.

The energy of 'pure Ti lattice consisting of 216 atoms' was calculated to be $E_{blk} = E(N_{Ti} = 216, N_V = 0, N_H = 0) = -1671,27eV$ (Slightly odd syntax shall be clarified in a moment). It is the energy difference between 216 Ti atoms standing alone and forming a hcp lattice with lattice constant, real Ti possesses. The number 216 atoms is sufficient for infinite lattice modelling and simultaneously such calculations last a reasonable amount of time (few days in our case). The energy value $E_{blk}$ was used as a reference to every other space arrangement of the Ti-VAC-H system.

Energy of lattice containing a VAC was further calculated. The energy is denoted: $E_{VAC}(N_{Ti}, 1, 0)$. That means that the vacancy formation energy is given by:

$$E_F(N_{Ti}, 1, 0) = E(N_{Ti} - 1, 1, 0) - \frac{N_{Ti} - 1}{N_{Ti}} E(N_{Ti}, 0, 0) \tag{7.1}$$

Similar thoughts lead to expressions for a mono-vacancy, surrounded by H atoms. Formation energy of such cluster is given by:

$$\begin{aligned} E_F(N_{Ti}, 1, N_H) &= E(N_{Ti} - 1, 1, N_H) - \\ &\left[\frac{N_{Ti} - 1}{N_{Ti}} E(N_{Ti}, 0, 0) + N_H \cdot \frac{1}{2} E(H_2)\right] \end{aligned} \tag{7.2}$$

$E(H_2)$ is energy difference between two H atoms, forming the $H_2$ molecule and two H atoms taken within energetic reference of our 216 atomic grid. It was calculated by VASP to be: $E(H_2) = -6.77$ eV. Note, that it is a bigger energy difference, than the $H_2$ molecule binding energy (table 1.1). Energies of grids containing H atoms were calculated with the vibration energies of absorbed H atoms taken into account. This vibration energy was calculated to be: $E_{vib} = 0.23$ eV.

Introduced formation energies were calculated for mono-vacancies with 1..8 surrounding H atoms, while (T) interstitial sites were considered to be their

initial positions. As I have already mentioned, different sources present different set of interstitial site to be occupied by H. Fukai [11] introduces (T) interstitial sites in Ti to be occupied. He proves that experimentally by various experimental methods. However some articles present (O) sites to be those occupied by H [48, 49]. Those results are based on DFT calculations and consider the system at 0K temperature only. Very neat characterization, between the theory & experiment discrepancy, concerning the (T) & (O) occupancy, is given here [19]. We have performed our own calculation by VASP and came to similar results. We calculated formation energies of Hydrogen in (T) & (O) sites in a non-defect Ti lattice: $E_F(216,0,1)(H\ in\ (T) = -0,49$ eV & $E_{216,0,1;F}(H\ in\ (O) = -0,57$ eV. Calculated energies are very similar, though the energy in (O) site is smaller. A decision was made to followed (T) sites for our system. We have therefore received different results, than the articles calculating with (O) set of sites.

Apart from formation energies of various Ti-VAC-H clusters, binding energies $E_B(N_{Ti}, N_V, N_H)$ were calculated. Binding energy represents the energy difference between the situation, when the last H atom is in the VAC neighborhood and when it is away, in an ordinary interstitial site. In other words, it is expressible as:

$$\begin{aligned} E_{N_{Ti},1,N_H;B} = -((E(N,1,H) + E(N_{Ti},0,0) - \\ (E(N_{Ti},1,N_H-1) + E(Hin(T);N_Ti,0,1))) \end{aligned} \tag{7.3}$$

We used the minus sign, in order to obtain a positive biding energy for systems with positive VAC-H affinity. For the sake of clarity, a figure of the binding energy construction is presented:

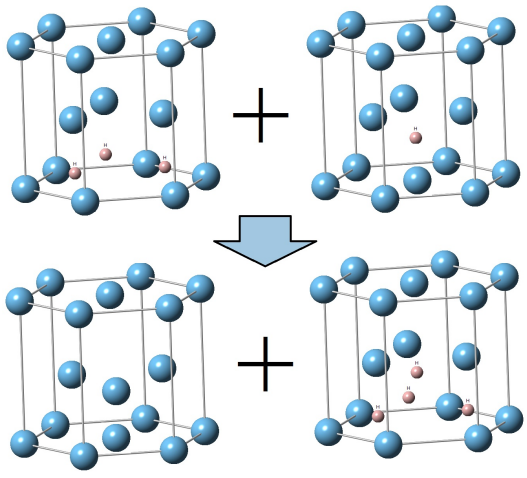

Figure 7.1: Binding energy calculation. Final situation is VAC decorated by $N_H$ H atoms and pure Ti bulk, initial situation is VAC decorated by $N_H - 1$ H atoms and one H atom in an ordinary interstitial site.

Three types of calculation were performed in VASP, a non-relaxed calculation, relaxed calculation, denoted $E^n(..)\&E^r(..)$ respectively and finally relaxed calculation, with the energy $E_{vib}$ included. The non-relaxed variation considers all present atoms in fixed positions. It performs a common DFT calculation and minimizes the total energy by variation of electron density and lattice parameters. The relaxed calculation allows individual atoms of the system to move. It therefore performs a complex molecular dynamics (MD) calculation, with a DFT calculation at each (MD) step. We have experienced, that the relaxed variant of our calculations leads to much better results in case of Ti. Covering of the vibrational energy leads to even more realistic results.

Convenient calculated values are presented in table 7.1 and figures 7.3,7.2. Labeling of Table 7.1 is following. System energy by VASP: $E^{n/r}$(Number of Ti atoms,Number of VAC,Number of H atoms) was skipped. Formation energy according to equation 7.2: $E_F(..)^{n/r}$ is presented for relaxed variants only and for $E_{vib}$ included.

Binding energy according to equation 7.3: $E_B(..)^r$ were calculated for relaxed version only. Including $E_{vib}$ is redundant, since the same number of H atoms occur at both minuend & subtrahend in 7.3. Positron life-times by Pos330 were calculated for relaxed & non-relaxed arrangement: $LT^{n/r}$.

One must keep in mind, that if for example four H atoms decorate a VAC, there are multiple ways of arranging them. Every way has different energy. See rows 7 and 8 in Table 7.1. Variant (a) stands for energetically not-favourable arrangement, while (b) stands for energetically favourable arrangement. See Figures 7.9 & 7.10 showing the arrangements.

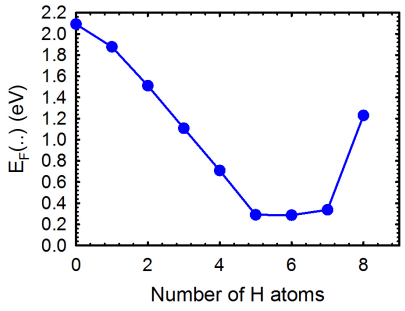


Figure 7.2: Formation energies of a mono-vacancy, surrounded by hydrogen atoms.

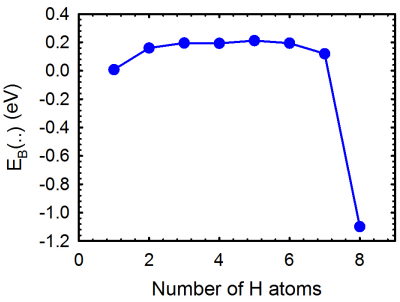


Figure 7.3: Binding energies of hydrogen atoms to a mono-vacancy.

| System $(N_{Ti}, N_V, N_H)$ | $E_F(..)^r$ eV | $E_B(..)^r$ eV | $LT^n$ ps | $LT^r$ ps |
|---|---|---|---|---|
| (216,0,0) | - | - | 146.8 | 146.8 |
| (216,0,1) in (O) | -0.57 | - | 146.8 | 146.8 |
| (216,0,1) in (T) | -0.48 | - | 146.8 | 146.8 |
| (215,1,0) | 0.09 | - | 236.5 | 234.9 |
| (215,1,1) | 1.88 | 0.01 | 228.3 | 220.0 |
| (215,1,2) | 1.51 | 0.16 | 219.0 | 196.7 |
| (215,1,3) | 1.11 | 0.19 | 212.0 | 188.1 |
| (215,1,4)[a] | 1.57 | -0,67 | $n$ | 198.3 |
| (215,1,4)[b] | 0.71 | 0,19 | 204.6 | 183.6 |
| (215,1,5) | 0.29 | 0.21 | 196.1 | 179.1 |
| (215,1,6) | 0.66 | -0.58 | 190.6 | 182.2 |
| (215,1,7) | 0.34 | 0.12 | 184.8 | 185.1 |
| (215,1,8) | 1.23 | -1.10 | 178.4 | 184.9 |

Table 7.1: Calculated energies of various Ti-VAC-H arrangements. $n$ stands for not calculated value, - stands for non-sense value.

Calculated positron life-times are in figure 7.4. Not-relaxed calculations differ greatly from their relaxation-allowed counterparts. Also occupancy of (T) sites lower the life-time more, than occupancy of (O) sites.

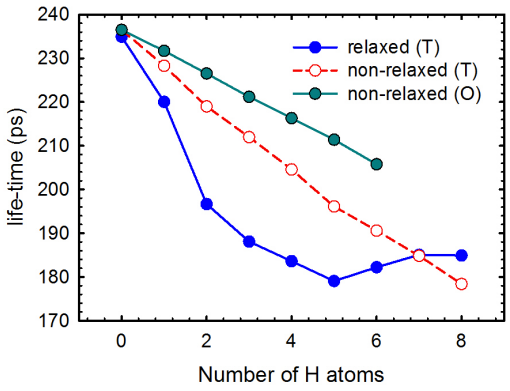


Figure 7.4: Calculated positron life-times for systems of mono-vacancy, surrounded by hydrogen atoms, occupying (T) sites, relaxed and not-relaxed variants. Not relaxed life–time for (O) occupancy.

Figures 7.5 to 7.14 shows calculated relaxations of Ti and H atoms. As one can see, the system's space arrangement changes radically with number of H atoms, surrounding the VAC.

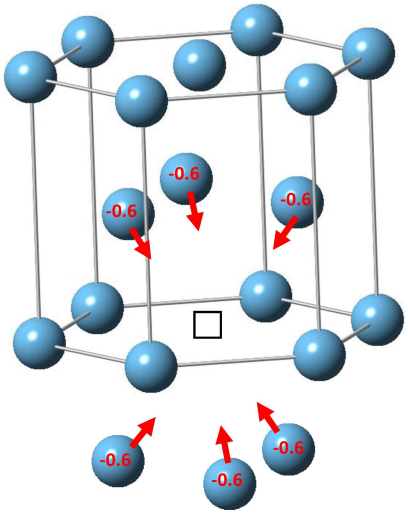


Figure 7.5: Lattice relaxation around a pure VAC.

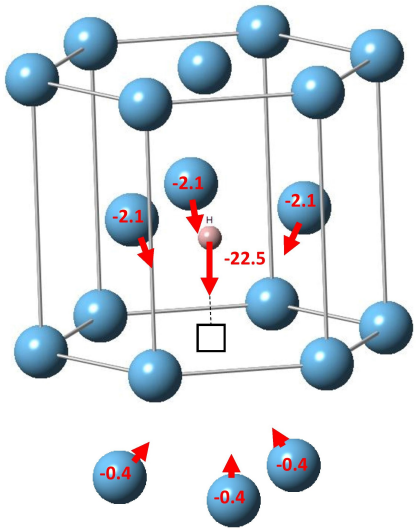


Figure 7.6: Lattice relaxation around a VAC, surrounded by 1 H atom.

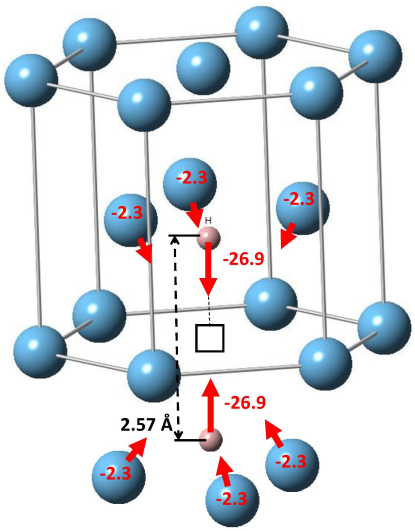


Figure 7.7: Lattice relaxation around a VAC, surrounded by 2 H atoms.

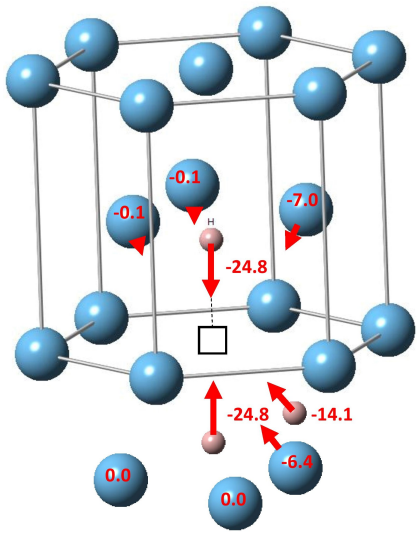


Figure 7.8: Lattice relaxation around a VAC, surrounded by 3 H atom.

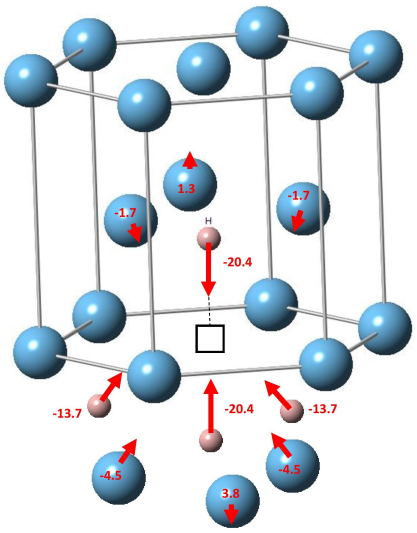


Figure 7.9: Lattice relaxation around a VAC, surrounded by 4 H atoms. Energetically not-favourable variant.

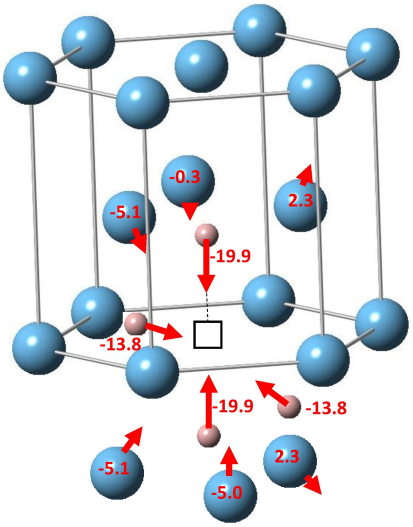


Figure 7.10: Lattice relaxation around a VAC, surrounded by 4 H atom. Energetically favourable variant.

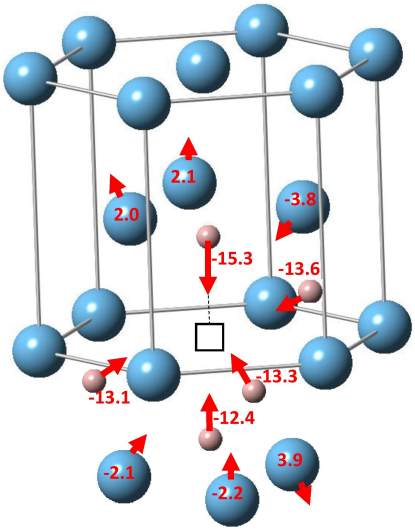


Figure 7.11: Lattice relaxation around a VAC, surrounded by 5 H atoms.

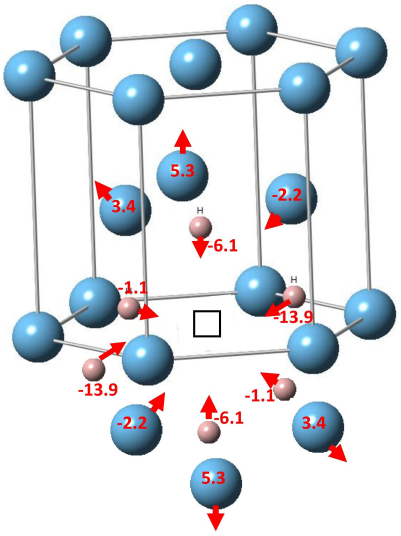


Figure 7.12: Lattice relaxation around a VAC, surrounded by 6 H atom.

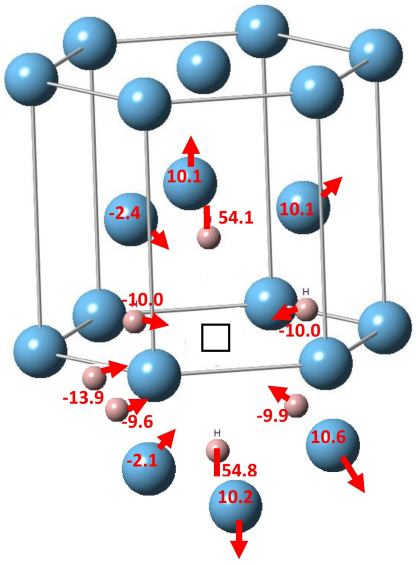


Figure 7.13: Lattice relaxation around a VAC, surrounded by 7 H atoms.

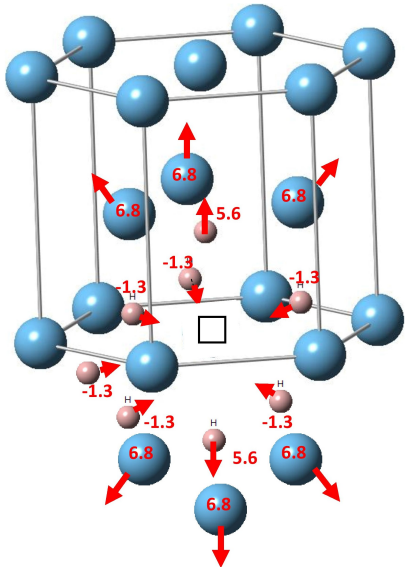


Figure 7.14: Lattice relaxation around a VAC, surrounded by 8 H atom.

From obtained energy values, the equilibrium vacancies concentration could have been be calculated, according to equation 1.20 (section 1.3.1). As was however mentioned already in that section, the problem is to express the pure lattice solubility $x$. The equation 1.14 is not suitable for the whole temperature range of $\alpha$-Ti existence. A decision was therefore made, to follow the experimental data for terminal solubility from [17]. This can be done under the assumption, that the amount of H absorbed in the defect-free lattice is much larger, than the amount attached to VAC. Otherwise, the calculated results would be higher than reality. The calculated VAC concentration is in figure 7.15. The H assisted VAC concentration is plotted against the pure VAC concentration given by Maxwell – Boltzmann distribution, with the energy $E_F(N_{Ti}, 1, 0)$ (the 4th line in table 7.1). As one can see, the H assisted concentration is of several order higher, than the pure VAC concentration. It has a maximum slightly bellow $600^0$C. Such behaviour is caused by the H solubility $x$ in the VAC free $\alpha$-Ti, which has its peak at $\sim 550^0$C (see phase diagram 1.2).

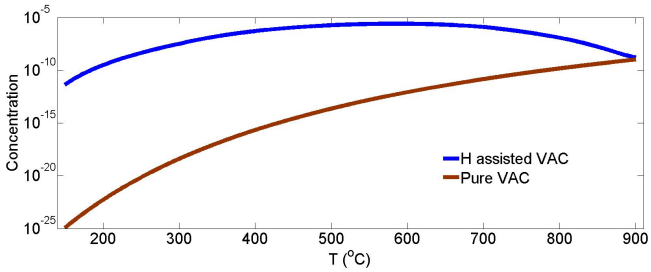


Figure 7.15: Calculated VAC concentration in $\alpha$-Ti.

The equation 1.20 was also used for individual clusters occupancy calculation. Five temperatures were selected. When the temperature is lowest, the solubility is in general low. But also, the cluster with the lowest formation energy (5 H atoms decorating the VAC) is occupied the most. As the temperature gets higher, the occupancy differences erase. Figure 7.16 significantly shows, that the cluster with 5 H atoms, decorating the VAC is the most favourable one. The reason for that is not only its lowest formation energy, but also the binomial factor in equation 1.20, which describes the configurational entropy. There is one more issue of this model. The equation 1.20 does not consider the different energies between different space arrangement of the same number of H atoms. (As we have seen in the case of 4 H atoms cluster). The model treats them as equal. Once again we have experienced, that Ti is a complicated material for theoretical descriptions.

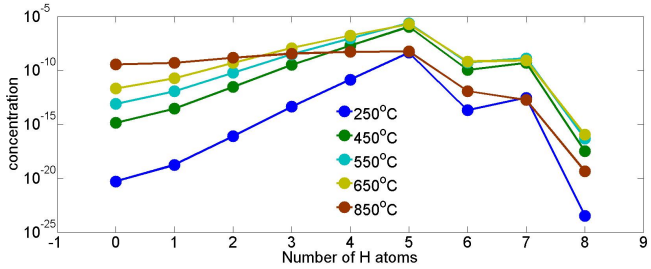


Figure 7.16: Calculated occupancy of given VAC-H clusters at given temperatures.

Figure 7.17 shows, how the life-time would change if H atoms was shifted from VAC to the position of (T) and (O) interstitial site and also little further. The Ti lattice was considered rigid, this calculation has therefore only qualitative character. It shows however, that the H atom influences noticeably the local electron density and therefore the life-time. In other words, the H atoms does not only distort the Ti lattice, which would later cause the life-time change. The presence of H atoms influences the electron density. It seem natural, since Ti

possesses 4 valence electrons and hydrogen one. The H electron is taken by the conduction band, as was mentioned in section 1.2.1 (source: [12]).

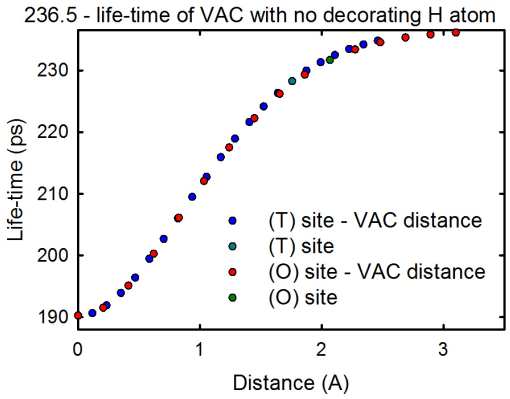


Figure 7.17: Calculated positron life–times for systems of a VAC, with one hydrogen atoms placed on a line between the VAC and given interstitial site. Not-relaxed calculation.

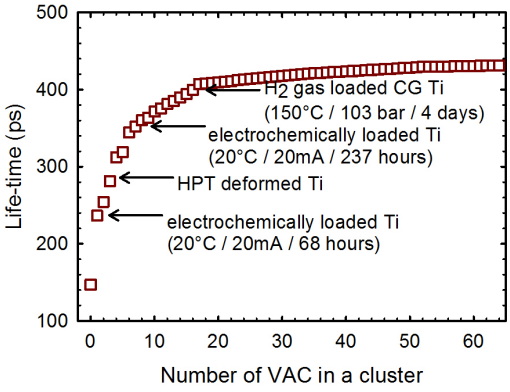


Figure 7.18: Calculated positron life-times for clusters of vacancies with no H atoms around. Experimentally detected values.

The last important calculation, performed for the Ti system was the calculation of positron life-times for clusters of VAC. They were actually detected by positrons in Ti samples prepared by SPD (ECAP & HPT) and samples loaded electrochemically and from the $H_2$ atmosphere of low temperature. Calculated life-times are in figure 7.18. Life-times measured in the Ti-H systems, that clearly correspond to VAC clusters, were added into the plot. One cannot however

compare the theoretical and experimental data absolutely, since VAC clusters in the Ti-H system are probably decorated by H atoms. This theoretical simulation was not performed yet and it is a subject to further investigation.

## 7.1 Summary

Performed theoretical calculations lead to very interesting results, regarding the Ti-H & Ti-VAC-H systems:

• The calculated formation energy of H inside an interstitial site corresponds to the experimental value, presented in section 1.3.1: $\Delta h = -0.55$ eV/atom. Calculated values are: $E_F(Hin(T)) = -0.48$ ev/atom and $E_F(Hin(O)) = -0.57$ ev/atom. The energy is lower for (O) interstitial site. This result is common to all DFT based theoretical calculations [19, 48, 49]. Article [48] also presents calculated energies of H in (O) & (T): -0.85 eV/atom & -0.70 eV/atom. These values are however lower than ours and more distant from the experimental value. Article [49] presents the same calculation with zero-point vibrational energy included, which we have included too. Their results are very similar to ours: -0.56 eV/atom in (T) & -0.62 eV/atom in (O), but still more distant from the experimental value.

• The formation energy of VAC-H clusters is lowered till 5 H atoms decorate the VAC. As present work might be on of the first investigation of (T) sites occupied by H, this value cannot be compared. It is a however higher number, than in the case of (O) sites occupancy. Up to 4 H atoms lower the formation energy of VAC [48].

• Figures 7.5 to 7.14 show, that the Ti lattice experience relatively large distortion, when a VAC-H cluster is formed. The strong H–H interaction, that are present in $\alpha$-Ti, are thus theoretically supported.

• Positron life-time is influenced, by the presence of H atom in a VAC. Not only due to the Ti lattice distortion, but due to the H atoms contribution to local electronic structure (figure 7.17).

• In this chapter, many interesting quantities were calculated and the calculations themselves gave us a great insight into the system of Ti, VAC & H. However, there is a lot more work, that could be done, that would be valuable. For example, the VAC-H clusters investigation could be widen to clusters of VAC, decorated by H atoms. Calculated life-times of such systems could then be immediately compared to their measured counterparts, since VAC clusters are found in the Ti-H system (figure 7.18).

• Another very interesting theoretical issue to be studied is the Ti & H atoms influence on the life-time.

# 8. Temperature Stability of the Ti-H system

In-situ XRD, PAS and DSC measurement were performed in order to look inside the Ti-H system during a thermal processing.

## 8.1 In–situ XRD Diffraction Measurements

Modern XRD apparatuses allows one to perform measurements at very specific and interesting conditions. In our case, we used the diffractometer under the Czech Academy for Sciences and performed diffraction measurements during annealing of our samples. The sample was heated in high vacuum ($5 \cdot 10^{-9}$ bar residual pressure) to given temperature, that was then held constant in order to measure the spectra. By doing this in-situ measurements we were able to detect phases that we would never detect in ordinary measurement at room temperature and Earth's atmosphere.

It has already been mentioned, that at room temperature only two phases can be detected by XRD ($\alpha$-Ti & $\delta$). Our first intention was to detect $\beta$-Ti in-situ. First we did not use Ti loaded with H, since a pure Ti sample transforms to $\beta - Ti$ at $882^0$C. If detected, such transition would serve as a good calibration of the used thermometer inside the XRD chamber.

We performed this experiment, however the bcc $\beta$-Ti was not detected up to temperature of $1000^0C$. See figure 8.1, showing a slice of obtained diffractograms. Peaks are obviously moving with temperature, which is given by the temperature dilatation of the Ti lattice. Measured lattice parameters at each temperature were collected and a plot of their evolution created. See figure **??**, showing the $\alpha$-Ti lattice parameters evolution. This growth can be compared to the thermal expansion coefficient of $\alpha$-Ti, which is: $\lambda \approx 8.6/\mathrm{K}$ and thus a temperature calibration can be done.

The Ti sample was held by bracket made out of Pt. During the measurement, the sample moved, by mistake, and the X-rays reached the Pt bracket. Pt has an fcc structure, and its diffraction peaks fortunately do not coincide with XRD peaks of $\alpha$-Ti. A regular measurement was actually collected, and it could have been used for the thermometer calibration as well. The Pt lattice parameter evolution is in figure 8.3. From the evolution of lattice parameters of Ti & Pt, it was found out, that the thermometer works fine and the $\alpha \rightarrow \beta$ transformation should be detected.

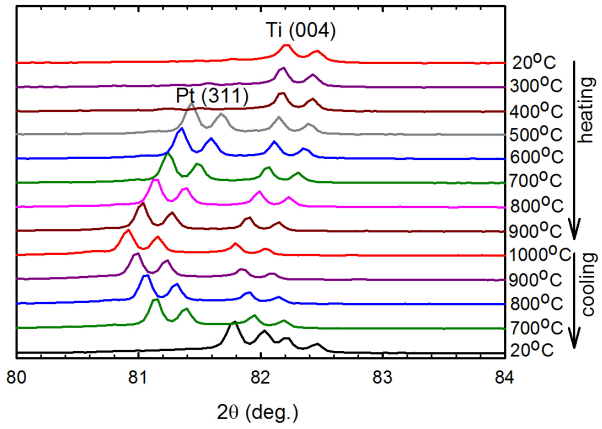


Figure 8.1: In–Situ XRD of previously annealed Ti sample. Slice of all diffractograms.

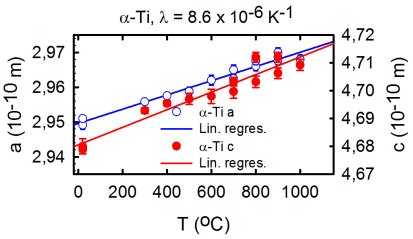


Figure 8.2: Evolution of a & c $\alpha$-Ti lattice parameters during heating of previously well annealed sample.

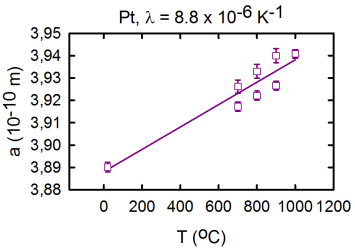


Figure 8.3: Evolution of lattice parameter of fcc-Pt bracket, that held the Ti sample.

The $\alpha \rightarrow \beta$ transformation at $882^0$C was detected by DTA, as will be seen in the next section. How come it was not observed by XRD? We came to the conclusion, that the transition is not visible, because a thin layer of measured Ti sample remains $\alpha$-Ti due to its penetration by oxygen and/or nitrogen. As was showed in the section 6.2.2, both oxygen and nitrogen are $\alpha$-phase stabilizers. Even small atomic concentration, like units of at. % cause that the $\alpha \rightarrow \beta$ transition is moved hundreds of degrees to higher temperatures. Even though the experiment was performed in vacuum, the remaining amount of atmospheric gasses caused this trouble.

However, the main reason of in-situ XRD was not to detect a pure $\beta$-Ti. A loaded sample was chosen and the thermal stability of the phase structure was investigated. We have chosen the eletrochemically loaded sample, which is from previous experiments, known to have a homogeneous layer of $\delta$-hydride on its

surface. The series of diffractograms (again just a slice) is visible in figure 8.4.

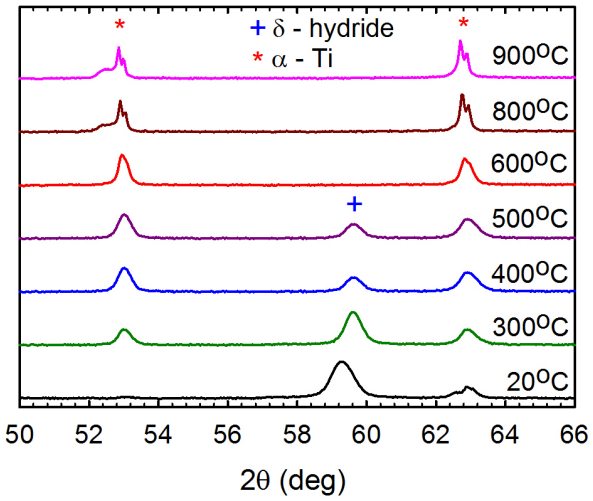


Figure 8.4: In-Situ XRD of Electrochemically loaded Ti sample. No $\alpha \rightarrow \beta$ is visible.

The measurement detected only $\alpha$-Ti and $\delta$-hydride. At romm temperature, there was vast majority of $\delta$-hydride. By annealing, the $\delta$-hydride slowly disappeared and the sample became a pure $\alpha$-Ti. The ratio between the two phases concentration was obtained from the diffractograms (8.4) and its temperature evolution is in figure 8.5.

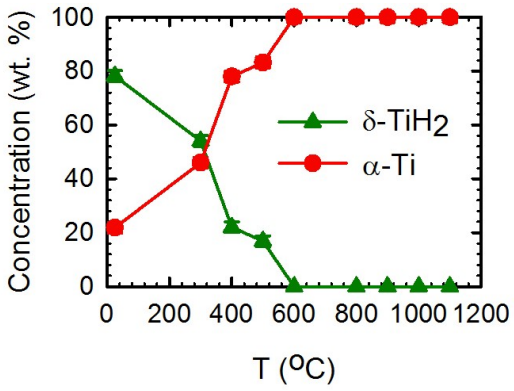


Figure 8.5: The decomposition of $\delta$-hydride during annealing.

Since the sample was according to its phase composition very close the pure

hydride, and the decomposition did not go through the $\beta$-Ti region (See the Ti-H phase diagram 1.2); the $\beta$-phase must have been forbidden again by the oxygen and/or nitrogen. This time, we cannot suppose, that the $\beta$-Ti would only occur deep in the bulk, since there in no H absorbed in the bulk, only at the this surface layer. We have observed the decomposition of this layer, in this experiment. This is even the reason, why the electrochemically loaded sample, was chosen at the first place.

If the $\beta$-Ti was indeed forbidden, we can imagine that the eutectic transition at $298^0$C was shifted to higher temperature. It was also assumed, that the solvus curves of $\alpha$ & $\delta$ phases remains uninfluenced by the missing $\beta$-phase. It is then possible to use the lever rule to calculate, where on the Ti-H phase diagram, we are present at each temperature, the XRD was measured. The $\delta/\alpha$ composition ratio is known (figure 8.5). The lever rule states, that if two phases of solubilities $x_1$ & $x_2$ are present in molar (atomic) concentration $n_1$ & $n_2$ the overall concentration $x$ can be calculated as:

$$x = \frac{x_2 n_2 + x_1 n_1}{n_1 + n_2} \tag{8.1}$$

Approximate values of solubilities $x_1$ & $x_2$ were taken from [17] and measured atomic concentrations were taken from figure 8.5. The difference between weight and molar concentration was omitted, since both hcp $\alpha$-Ti & fcc $\delta$-hydride are closed-packed structures with 12 atoms per cell. In $\delta$-hydride, up to 4 H atoms are present in the (T) sites. The molar weight of Ti is 47, while of H it is 1. Thus the difference between weight and molar concentration of $\delta$-hydride differs by the factor of 142/141. Following places on the Ti-H phase diagram were calculated:

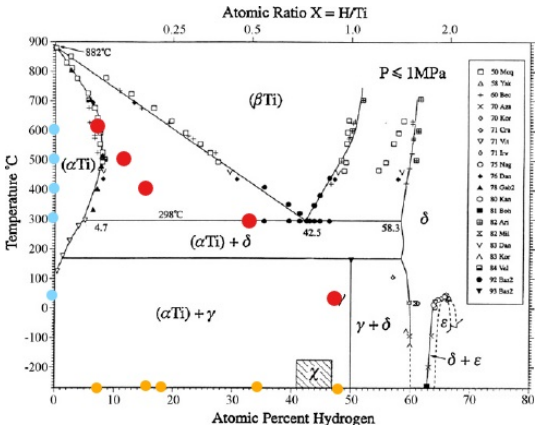


Figure 8.6: Positions on the phase diagram during the experiment. Calculation by the lever rule.

An interesting temperature development was observed on $\delta$-hydride lattice

parameter. It can be seen in figure 8.7. First, the structure contracted itself after reaching the temperature $300^0$C, then it expanded rapidly, at $500^0$C. The increase is probably caused by the fact, that $\delta$-hydride has larger volume per primitive cell, than $\alpha$-Ti. When $\delta$-hydride decomposes to $\alpha$-Ti, a dilatation strain is introduced to the sample. That strain enlarges the $\delta$-Ti lattice parameter and leaves the $\alpha$-Ti as it is.

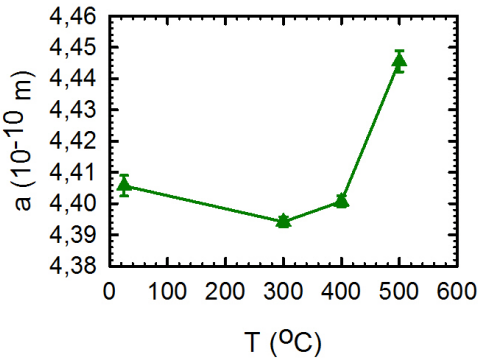


Figure 8.7: Evolution of lattice parameter of fcc-$\delta$-hydride.

## 8.2 PAS Measurements during Thermal Processing

Two Ti samples underwent the same isochronal annealing process as already introduced (50 minutes annealing, $50^0$C temperature step). The first sample was first annealed and then loaded with H at $400^0$C for 5 hours. The second sample were subjected to ECAP (N=8 passes) and later loaded in the same way. During the isochronal annealing, PALS was measured. That means, both samples were annealed for 50 minutes, quenched and then measured. Thus specific phase composition present at certain temperature could have been preserved.

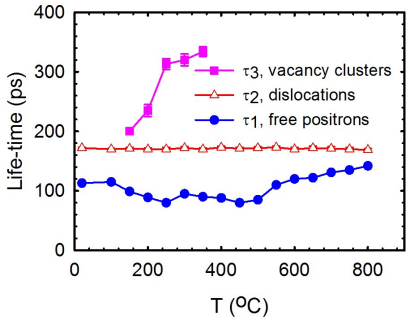


Figure 8.8: Positron life-times development of loaded CG Ti during annealing.

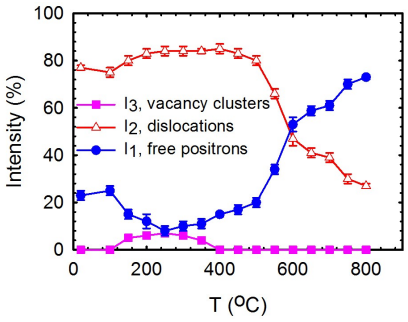


Figure 8.9: Intensities of detected components.

In case of the CG Ti, two component spectrum, was present at the beginning of the annealing process. The component form dislocations had intensity of 80% and the rest were free positrons. However at $150^0$C, VAC clusters occurred. Their life–time was increasing with temperature, that means their size increased. Comparing measured life–time with calculated life–times in figure 7.18, the clusters changed from bi-VAC (probably decorated by some H atoms) to clusters, containing 6 VAC. The VAC clusters disappeared at temperature of $400^0$C. From the temperature of $500^0$C, vacancies present in the sample began to vanish. The VAC clusters probably occurred due to the smaller size of $\alpha$-Ti, compared to $\delta$-hydride. The decomposing $\delta$ introduced a free volume in the form of VAC clusters into the bulk.

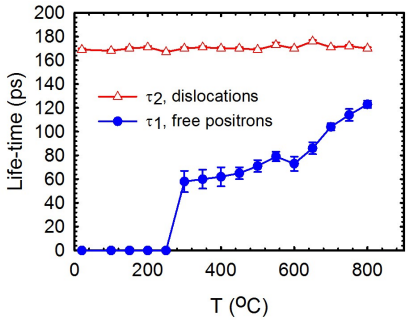


Figure 8.10: Positron life-times development of loaded ECAP Ti during annealing.

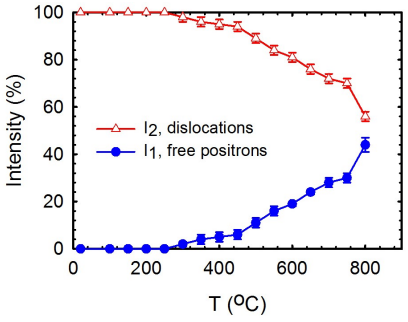


Figure 8.11: Intensities of detected components.

The same measurement for ECAP Ti is in figures 8.10 & 8.11. During thus thermal processing, no VAC clusters occurred. It is probably because the UFG structure is much more flexible, and the volume reduction is able to compensate.

Another difference compared to the CG Ti measurement is that dislocations began to vanish a little bit sooner. It is cause by the non-equilibrium state of the UFG structure, which has a strong intention to return to equilibrium state, with CG structure.

## 8.3 Differential Thermal Analysis Measurements & Results

DTA measurements were the last one performed on our Ti samples in order to see phase transitions and also the release of H in-situ. The TG and released $H_2$ pressure (from the mass spectrometer) were measured simultaneously with DTA on loaded Ti samples.

First, a plain DTA curve of pure, defect free Ti was obtained, see figure 8.12. The curve shows ordinary behaviour and the $\alpha \rightarrow \beta$ transition is well apparent, unlike in the case of the in-situ XRD measurement. This proves, that the Ti sample as a bulk indeed undergoes the phase transition. However as the XRD is sensible to the sample surface only, it does not detect the $\alpha \rightarrow \beta$ transition. The heating and cooling speed was set on 10K/min. The speed 15K/min was tried, but led to overheating, and the $\alpha \rightarrow \beta$ peak was not well observable. The speed 5K/min led to extreme broadening of the $\alpha \rightarrow \beta$ peak and was therefore not suitable as well.

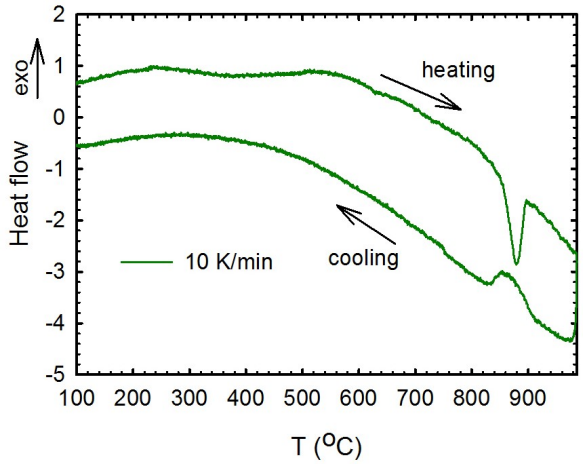


Figure 8.12: DSC curve of pure, CG Ti.

After that, five H loaded Ti samples were measured and results from all DTA, TG and $H_2$ pressure where collected. A difference between measuring this set of

samples and measuring the pure Ti is the heating speed. I was determined to be 5 K/min, for the best result in case of loaded samples. The H release clearly has a different kinetics, than ordinary structural transformations, like $\alpha \rightarrow \beta$.

Measured samples can be divided into three groups. First there are DTA curves of sample that were completely transformed to $\delta$-hydride. It is the CG Ti, loaded at $500^0$C (figure 8.13) and the HPT sample loaded at low temperature and high pressure (figure 8.14).

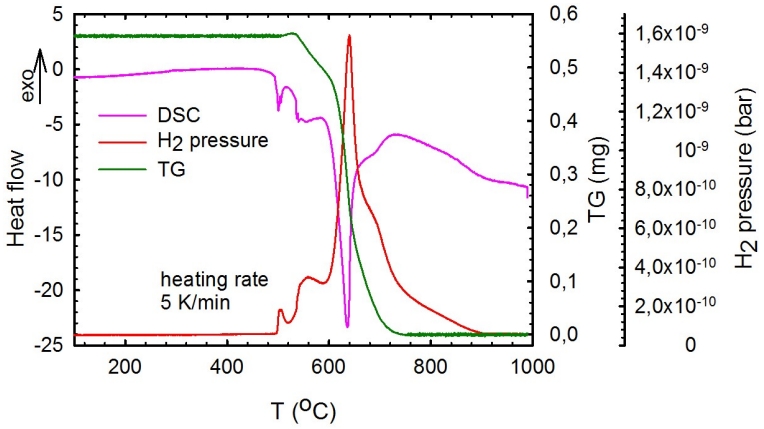


Figure 8.13: DTA curve of CG Ti, loaded from gas phase, on $500^o$C, 0.77 bar, for 50 hours.

The CG sample, that was completely transformed to $\delta$-hydride (see for example diffractogram 6.24) contains large amount of dislocations. Its DTA curve in shows multiple peaks, which all seem to be endothermic and connected with a release of H, detected by TG and pressure measurement. The peak at $640^0$C comes from the $\delta$-hydride decomposition since it is connected with the largest energy change and the $\delta$-hydride structure has has a very low energy (see section 1.3.3) compared to $\alpha$-Ti and $\beta$-Ti. It is at approximately $720^0$C followed by a poorly visible exothermic peak, which could indicate the $\beta \rightarrow \alpha$-Ti change. At roughly $900^0$C there is a very shallow depression, on the DTA curve, which is the $\alpha \rightarrow \beta$-Ti change in already H free sample. The last peaks to be identified are the two peaks at $500^0$C & $600^0$C. They come probably from H release from various defects systems in the material. The H lowers the formation energy of defects and its release is therefore an endothermic process. The following annealing of H free defects should be accompanied by an exothermic peak. It is however a process, that last longer, because defects have much lower mobility, than H atoms [3]. The exothermic contribution is therefore hidden and only the endothermic peak from the H release is visible.

Finally we have to admit, that it is not known, what defect systems release the

H at what temperature. That is why we performed those numerical calculations at least for the VAC-H system. There is however a need for further investigation in this field still.

The DTA measurement of HPT sample, loaded at low temperature and high pressure (figure 8.14), shows similar progress, while heated, as the CG Ti. It is because it was also completely transformed to $\delta$-hydride. The number of peaks connected with the H release from defects is however larger. The HPT sample thus contains more developed system of trapping centres for H.

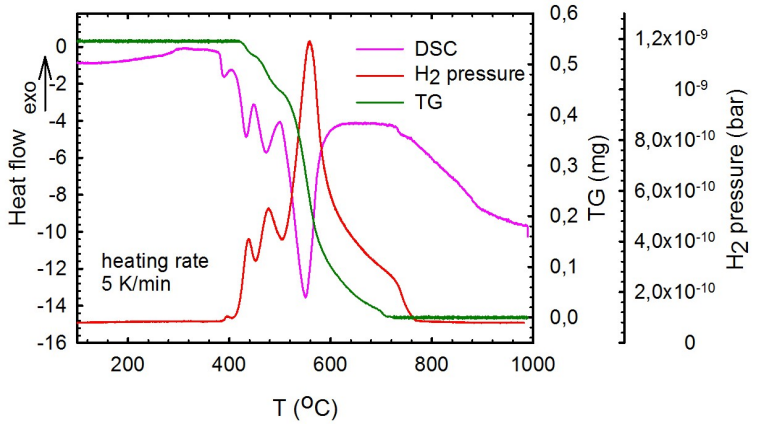


Figure 8.14: DTA curve of HPT Ti, loaded from gas phase, on 150$^o$C, 100 bar, for 100 hours.

The second group of DTA measured samples are samples, which were not fully transformed to $\delta$-hydride. They exhibit a two phase structure with grains of $\alpha$-Ti and $\delta$- hydride. They are the ECAP sample, loaded at high temperature and low pressure for 5 hours only and the CG Ti loaded at low temperature and high pressure, which is known to be transformed to $\delta$-hydride only in a thin surface layer.

DTA curves of these samples shows a sharp peak at temperature a little more than 298$^0$C, the eutectic transition point. It must be connected with the $\alpha \rightarrow \beta$ transition, since the $\beta$-Ti has a structure with higher energy. The samples enters the $(\beta + \delta)$ area on the Ti-H phase diagram (see figure 8.18 showing the evolution of all DTA measured samples on the phase diagram). These two samples further release H at temperature of 600$^0$C. The release is again connected with an endothermic peak, which is less visible though.

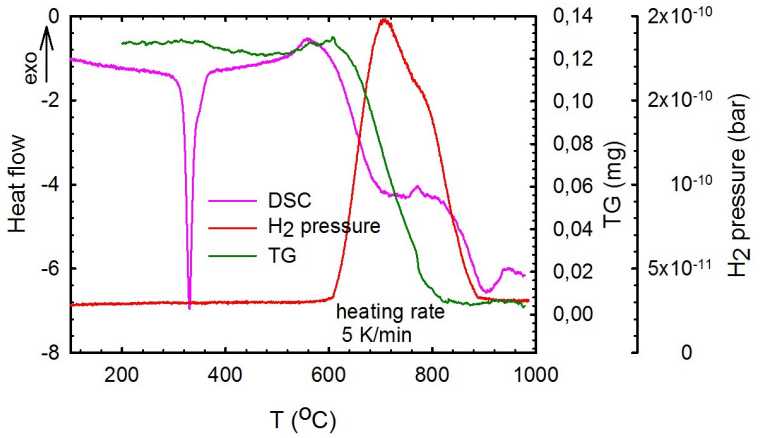


Figure 8.15: DTA curve of ECAP Ti, loaded from gas phase, on 400$^o$C, 1 bar, 5 hours.

Both CG and UFG samples shows the $\alpha \rightarrow \beta$ transition at 882$^0$C. That proves that all H is released till this temperature. One can even see a small exothermic peak, slightly bellow 800$^0$C which would then accompany the $\beta \rightarrow \alpha$ Ti transformation.

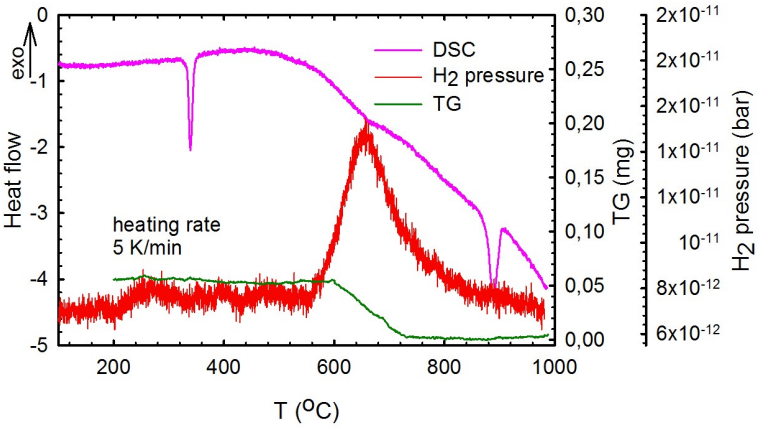


Figure 8.16: DTA curve of CG Ti, loaded from gas phase, on 150$^o$C, 100 bar, for 100 hours.

The last presented DTA measurement is the measurement of the CG Ti sample loaded at 400$^0$C for 5 hours. It is shown in the figure 8.17. This sample absorbed very little H, compared to its ECAP counterpart (figure 8.15). The TG and $H-2$ pressure measurement is therefore not very precise, though it still shows some of sample's evolution. There is a very well apparent $\alpha \rightarrow \beta$

transformation at $882^0$C. The H release occur at temperature higher than $650^0$C.

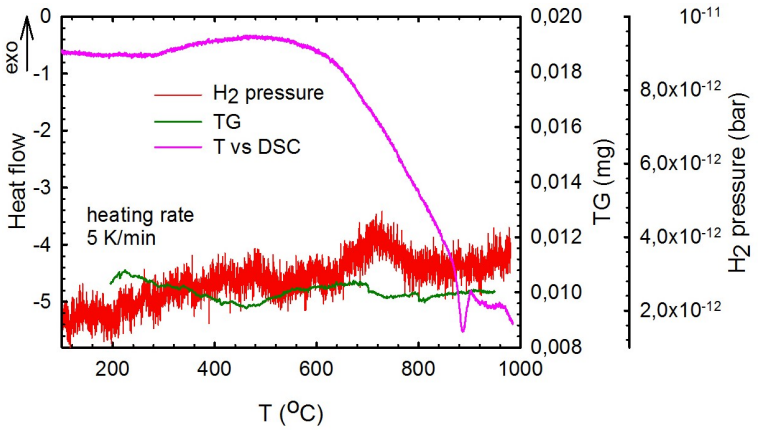


Figure 8.17: DTA curve of CG Ti, loaded from gas phase, on $400^o$C, 1 bar, for 5 hours.

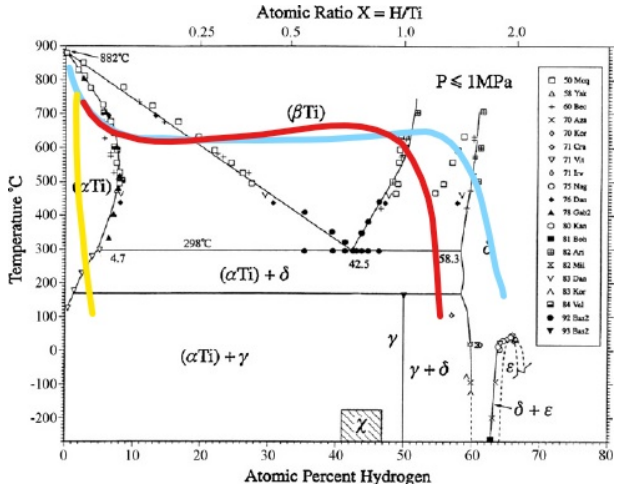


Figure 8.18: Guessed samples position on the Ti-H phase diagram during the DTA measurement. Blue are the completely transformed samples, red are double phases samples and yellow is the last sample, which absorbed only minimum amount of H.

## 8.4 Summary

• The temperature stability of loaded Ti samples was studied by in-situ XRD, PALS and DTA. The XRD and PALS measurement can be directly compared, due to the similar time of annealing at certain temperature. The DTA was much faster measurement and therefore the same processes might have occurred at different temperature.
• It would be highly valuable to perform the DTA in a similar time scale, like PALS and XRD.
• According to XRD results, the $\delta$-hydride is completely decomposed at $600^0$C.
• According to PALS, its decomposition is accompanied by VAC cluster, which later disappear, in case of the CG Ti sample.
• The UFG sample does not need such process since its structure is very flexible.
• From DTA, TG & $H_2$ pressure measurement we know, that during the thermal treatment, H is first released from defects. Then, the $\delta$-hydride decomposes at $600^0$C approximately. Among these changes, $\alpha \rightarrow \beta$ and reverse transformation are well visible at DTA curves.

# 9. Conclusions & Overall Summary

In this thesis, basic theoretical knowledge about the metal–hydrogen systems was presented. Couple bibliographic sources were suggested for a reader, that would be interested. The theoretical introduction also set up a proper frame to our performed experiments. It also gave us models, which we used for the Ti-VAC-H system theoretical simulation. A relatively complex theoretical calculations based on DFT were performed in this work. The interaction between VAC and H was studied numerically. Additionally, positron life-times for VAC, decorated by H atoms were calculated. calculated positron life-times are the basis for successful PALS spectra processing.

In the experimental part, we have focused on the interaction between H, absorbed in the lattice of Ti and constitutional defects, like vacancies, dislocations and grain boundaries. We have therefore prepared two sets of samples, one defect-free and the other subjected to severe plastic deformation (SPD). SPD introduced large amount of grain boundaries, dislocations and sometimes VAC clusters into Ti samples. H loading techniques were used to load prepared samples by H. Changes in the phase constitution and concentration of defects were followed.

A short summary was given at the end of every chapter presenting results. The most important results of this work can be summarized as follows:
• The UFG structure is stable up to temperature of $400^0$C in Ti.
• H loading performed on UFG Ti samples leads to quicker transformation to $\delta$-hydride for all three loading methods used. The reason is the diffusion of H around the grain boundaries.
• H loading introduces a high density of dislocations into all samples studied.
• In addition to that, low temperature H loading introduces also VAC clusters. VAC are mobile at high temperatures, they quickly diffuse to empty spaces, present in the sample. They are therefore not observed in case of samples loaded at high temperature and slowly cooled down.
• H stabilizes defects in Ti samples. First, their formation energy is lowered by H. Thus a large amount of them is introduced into the sample while loading.
• H is relatively temperature stable in Ti. It has a positive affinity to both structural defects and Ti atoms.
• Part of experimental results obtained in this work were used to write an article: Characterization of defects in titanium created by hydrogen charging, which has been accepted for publication in International Journal of Hydrogen Energy. Those results have also been presented in the 5th International Symposium on Metal-Hydrogen Systems, in Switzerland, 2016. Results of performed theoretical calculations should also be published soon.

# 10. List of Abbreviations

| | |
|---|---|
| Ti | titanium |
| H | hydrogen (protonium in section 1.2.1) |
| VAC | a vacancy, vacancies |
| HAC | hydrogen–assisted cracking |
| UFG | ultra–fine grained material, materials |
| DSC | differential scanning calorimetry |
| PALS | positron annihilation life-time spectroscopy |
| XRD | X-ray diffraction |
| HV | Vickers micro-hardness |
| D | deuterium |
| T | tritium |
| hcp | hexagonal close-packed structure |
| fcc | face-centred cubic structure |
| bcc | body-centred cubic structure |
| fct | face-centred tetragonal structure |
| fco | face-centred orthorhombic structure |
| (O) | octahedral interstitial site/sites |
| (T) | tetrahedral interstitial site/sites |
| UFG | ultra-fine grained |
| ECAP | equal channel angular pressing |
| HPT | high pressure torsion |
| SPD | severe plastic deformation |
| STM | simple trapping model |
| MD | molecular dynamics |
| UV | ultra-violet |
| ADC | analog-to-digital converter |
| ATSUP | atomic superposition |
| LDA | local density approximation |
| HMC | high momentum calculation (Pos330 program) |
| au | atomic units |
| PAW | projector-augmented wave |
| PP | pseudo-potentials |
| PW | plane-wave |
| DOS | density of states |
| Pt | plattinum |

# Bibliography


[1] Jr. Matthew J. Donachie. *Titanium a Technical Guide*. ASM International, 2000.

[2] Williams James C. Lütjering, Gerd. *Titanium*. Springer Berlin Heidelberg, 2007.

[3] Petar Maroevic. *Equilibrium and Diffusion Studies of Metal - Hydrogen Systems*. PhD thesis, Rice University, 1998.

[4] et. al D. Chartouni. Metal hydride fuel cell with intrinsic capacity. *International Journal of Hydrogen Energy*, 27(9):945–952, sep 2002.

[5] R. A. Oriani. Whitney award lecture—1987:hydrogen—the versatile embrittler. *CORROSION*, 43(7):390–397, jul 1987.

[6] Ervin Tal-Gutelmacher and Dan Eliezer. The hydrogen embrittlement of titanium-based alloys. *JOM*, 57(9):46–49, sep 2005.

[7] E. Tal-Gutelmacher, D. Eliezer, and Th. Boellinghaus. Investigation of hydrogen-deformation interactions in -21s titanium alloy using thermal desorption spectroscopy. *Journal of Alloys and Compounds*, 440(1-2):204–209, aug 2007.

[8] Ruslan Z. Valiev, Alexander P. Zhilyaev, and Terence G. Langdon. *Bulk Nanostructured Materials*. John Wiley & Sons, Inc, oct 2013.

[9] F Lukáč, J Čížek, J Knapp, I Procházka, P Zháňal, and R K Islamgaliev. Ultra fine grained ti prepared by severe plastic deformation. *Journal of Physics: Conference Series*, 674:012007, jan 2016.

[10] J. Cizek, M. Janecek, O. Srba, R. Kuzel, Z. Barnovska, I. Prochazka, and S. Dobatkin. Evolution of defects in copper deformed by high-pressure torsion. *Acta Materialia*, 59(6):2322–2329, apr 2011.

[11] Yuh Fukai. *The Metal-Hydrogen System*. Springer Berlin Heidelberg, 1993.

[12] R. D. Shannon and C. T. Prewitt. Effective ionic radii in oxides and fluorides. *Acta Crystallographica Section B Structural Crystallography and Crystal Chemistry*, 25(5):925–946, may 1969.

[13] Geoffrey Davies. *Basic Inorganic chemistry, second edition (Cotton Albert F. Wilkinson, Geoffrey)*, volume 65. American Chemical Society (ACS), sep 1988.

[14] Lizhi Liu. *Surface Hardening of Titanium Alloys by Gas Phase Nitridation Under Kinetic Control*. PhD thesis, 2005.

[15] Henry Wu. *Oxygen Diffusion Through Titanium and Other hcp Metals*. PhD thesis, 2013.

[16] The Editors of Encyclopædia Britannica. Thomas graham, 2006.

[17] F. D. Manchester. *Phase Diagrams of Binary Hydrogen Alloys*. ASM International, 2000.

[18] Richard G. Hennig, Dallas R. Trinkle, Johann Bouchet, Srivilliputhur G. Srinivasan, Robert C. Albers, and John W. Wilkins. Impurities block the to martensitic transformation in titanium. *Nature Materials*, 4(2):129–133, jan 2005.

[19] Damien Connétable, Julitte Huez, Éric Andrieu, and Claude Mijoule. First-principles study of diffusion and interactions of vacancies and hydrogen in hcp-titanium. *Journal of Physics: Condensed Matter*, 23(40):405401, sep 2011.

[20] H. Kozima. Cold fusion phenomenon in open, nonequilibrium, multi-component systems – self-organization of optimum structure. In *Reports of cold fusion research laboratory*, 2012.

[21] K. Linga Murty. Effect of c/a-ratio on crystallographic texture and mechanical anisotropy of hexagonal close packed metals. *Materials Science Forum*, 426-432:3575–3580, 2003.

[22] Adolf Sieverts. The absorption of gases by metals. 1929.

[23] H. Wipf. Solubility and diffusion of hydrogen in pure metals and alloys. *Physica Scripta*, T94(1):43–51, 2001.

[24] Nan Z Carr and Rex B McLellan. The thermodynamic and kinetic behavior of metal–vacancy–hydrogen systems. *Acta Materialia*, 52(11):3273–3293, jun 2004.

[25] Prof. Ling Zang. Diffusion coefficient (diffusivity), 2015.

[26] G.K Williamson and W.H Hall. X-ray line broadening from filed aluminium and wolfram. *Acta Metallurgica*, 1(1):22–31, jan 1953.

[27] M. Griffiths, D. Sage, R. A. Holt, and C. N. Tome. Determination of dislocation densities in HCP metals from x-ray diffraction line-broadening analysis. *Metallurgical and Materials Transactions A*, 33(3):859–865, mar 2002.

[28] Inc. Perkin Elmer. Differential scanning calorimetry (dsc). online, 2014.

[29] A. Dupasquier. *Positrons in Solids*. Springer, 2011.

[30] R. M. Nieminen, E. Boronski, and L. J. Lantto. Two-component density-functional theory: Application to positron states. *Physical Review B*, 32(2):1377–1379, jul 1985.

[31] W. Kohn and L. J. Sham. Self-consistent equations including exchange and correlation effects. *Physical Review*, 140(4A):A1133–A1138, nov 1965.

[32] Michael P. Teter, Michael C. Payne, and Douglas C. Allan. Solution of schrödinger's equation for large systems. *Physical Review B*, 40(18):12255–12263, dec 1989.

[33] M. J. Puska and R. M. Nieminen. Theory of positrons in solids and on solid surfaces. *Reviews of Modern Physics*, 66(3):841–897, jul 1994.

[34] K O Jenson and A B Walker. Non-local positron-electron density functional theory and the positron surface state. *Journal of Physics F: Metal Physics*, 18(12):L277–L285, dec 1988.

[35] Martijn Marsman Georg Kresse and Jurgen Furthmuller. Vasp the guide. online, 2016.

[36] G. E. Kimball and G. H. Shortley. The numerical solution of schrödingers equation. *Physical Review*, 45(11):815–820, jun 1934.

[37] Ari P. Seitsonen, M. J. Puska, and R. M. Nieminen. Real-space electronic-structure calculations: Combination of the finite-difference and conjugate-gradient methods. *Physical Review B*, 51(20):14057–14061, may 1995.

[38] J.P. Desclaux. Hartree fock slater self consistent field calculations. *Computer Physics Communications*, 1(3):216–222, jan 1970.

[39] J.P. Desclaux. A multiconfiguration relativistic DIRAC-FOCK program. *Computer Physics Communications*, 9(1):31–45, jan 1975.

[40] I.V Alexandrov R.Z Valiev, R.K Islamgaliev. Bulk nanostructured materials from severe plastic deformation. *Progress in Materials Science*, 45(2):103–189, mar 1999.

[41] X.H. An, Q.Y. Lin, S.D. Wu, Z.F. Zhang, R.B. Figueiredo, N. Gao, and T.G. Langdon. Significance of stacking fault energy on microstructural evolution in cu and cu–al alloys processed by high-pressure torsion. *Philosophical Magazine*, 91(25):3307–3326, sep 2011.

[42] F. Bečvář, J. Čížek, I. Procházka, and J. Janotová. The asset of ultra-fast digitizers for positron-lifetime spectroscopy. *Nuclear Instruments and Methods in Physics Research Section A: Accelerators, Spectrometers, Detectors and Associated Equipment*, 539(1-2):372–385, feb 2005.

[43] Pauline Millenbach and Meir Givon. The electrochemical formation of titanium hydride. *Journal of the Less Common Metals*, 87(2):179–184, oct 1982.

[44] Akito Takasaki, Yoshio Furuya, Kozo Ojima, and Youji Taneda. Hydride dissociation and hydrogen evolution behavior of electrochemically charged pure titanium. *Journal of Alloys and Compounds*, 224(2):269–273, jul 1995.

[45] L. Yan, S. Ramamurthy, J.J. Noël, and D.W. Shoesmith. Hydrogen absorption into alpha titanium in acidic solutions. *Electrochimica Acta*, 52(3):1169–1181, nov 2006.

[46] D. Eliezer, E. Tal-Gutelmacher, C.E. Cross, and Th. Boellinghaus. Hydrogen trapping in -21s titanium alloy. *Materials Science and Engineering: A*, 421(1-2):200–207, apr 2006.

[47] E. Tal-Gutelmacher, D. Eliezer, and E. Abramov. Thermal desorption spectroscopy (TDS)—application in quantitative study of hydrogen evolution and trapping in crystalline and non-crystalline materials. *Materials Science and Engineering: A*, 445-446:625–631, feb 2007.

[48] Andrey I. Kartamyshev, Dat Duy Vo, and Alexey G. Lipnitskii. The interaction between light impurities and vacancies in titanium and aluminum metals: A DFT study. *St. Petersburg Polytechnical University Journal: Physics and Mathematics*, 2(2):96–102, jun 2016.

[49] D.O. Poletaev, D.A. Aksyonov, Dat Duy Vo, and A.G. Lipnitskii. Hydrogen solubility in hcp titanium with the account of vacancy complexes and hydrides: A DFT study. *Computational Materials Science*, 114:199–208, mar 2016.

# List of Figures

# List of Tables